EUROPEAN ORGANIZATION FOR NUCLEAR RESEARCH

CERN/EP 80-67
13 May 1980

RESULTS FROM A SLOW PROTON TRIGGER EXPERIMENT AT 12 GeV/c

C. Evangelista, B. Ghidini, A. Palano, V. Picciarelli and G. Zito
Istituto di Fisica dell'Università and Sezione INFN, Bari, Italy

J. Bröring, K. Müller, E. Paul, W. Renneberg and W. Rühmer
Physikalisches Institut der Universität Bonn, West Germany

J. Eades, B.R. French, J. Moebes and F. Navach(*)
CERN, European Organization for Nuclear Research, Geneva, Switzerland

M. Edwards(**), I.L. Smith and G. Petzmezas
Daresbury High Energy Physics Laboratory, Daresbury, U.K.

R.A. Donald, D.N. Edwards, J.R. Fry and M.A. Houlden
Oliver Lodge Laboratory, University of Liverpool, Liverpool, U.K.

A. Cantore, M. Di Corato, L. Mandelli and L. Perini
Istituto di Fisica dell'Università and Sezione INFN Milan, Italy

ABSTRACT

A study of the reaction $\pi^- p \to X^- p$, where $X^- \to \pi^-\pi^o$, $\pi^+\pi^-\pi^-$, $\pi^+\pi^-\pi^-\pi^o$, $\pi^+\pi^+\pi^-\pi^-\pi^-$ and $\pi^+\pi^+\pi^-\pi^-\pi^-\pi^o$, based on 1.17×10^6 events, corresponding to a mean sensitivity of 200 events/μb is presented. Properties of the various X^- systems are analysed in detail.

Submitted to Nuclear Physics B

(*) Now at Bari University, Bari, Italy.

(**) Now at the Rutherford Laboratory, Rutherford, U.K.

0002P/BRF/mk

1. INTRODUCTION

We report on the results of an experiment run on the Omega Spectrometer at CERN. $\pi^- p$ interactions at 12 GeV/c were studied by triggering on a slow recoil proton with four-momentum transfer squared (t) in the range -0.15 to -0.4 GeV^2. The beam flux sensitivity of the experiment was 16.9 events/nb. The acceptance depends on both M (the recoil mass to the proton) and t. At typical values of M and t (1.7 GeV and -0.3 GeV^2) the acceptance is 5%. For peripheral production of meson resonances with a t dependence of $e^{-6|t|}$, this corresponds to an experimental sensitivity of 200 events/μb. Results on meson production in the following channels are presented and discussed.

(a) A study of X^o, X^-, X^{--} missing mass spectra in

$\pi^- p \to X^- p$ 1 272 303 events (elastic excluded) (1)

$\to X^o \pi^- p$, $X^o \pi^- \pi^- \pi^+ p$ 1 272 303 and 373 769 events respectively (2)

$\to X^{--} \pi^+ p$ 696 178 events (3)

(b) A study of exclusive channels in

$\pi^- p \to \pi^- \pi^o p$ 42 705 events (4)

$\to \pi^+ \pi^- \pi^- p$ 128 404 events (5)

$\to \pi^o \pi^+ \pi^- \pi^- p$ 84 149 events (6)

$\to 2\pi^+ 3\pi^- p$ 8 244 events (7)

$\to \pi^o 2\pi^+ 3\pi^- p$ 14 258 events (8)

The subjects we discuss are the following:

(a) $\pi^- p \to X^- p$: we present the missing mass spectrum $M(X^-)$ and show that we see no evidence for narrow width bosons [1,2]: these data represent about seven times the data of ref. [1] and about two times the data of ref. [2].

(b) $\pi^- p \to X^o \pi^- p$: with ten times the statistics of ref. [3] we confirm the presence of an enhancement in the neutral missing mass spectrum $M(X^o)$ [3] with a mass and width consistent with those of the D^o meson provided the π^- is selected to be the fastest negative

particle. We show further that the enhancement is associated with the decay $D^o \to \delta^{\pm}\pi^{\mp}$ in the reaction

$$\pi^- p \to \pi^-_f D^o p \quad \begin{matrix} \to \delta^{\pm}\pi^{\mp} \\ \to \eta^0\pi^{\pm} \end{matrix} \quad , \tag{9}$$

where the subscript f labels the fastest particle of that charge. The $M(X^o)$ spectrum also shows a strong η^o signal ($\sim$ 3600 ev.) in the 2-prong channel

$$\pi^- p \to \eta^o \pi^- p \quad . \tag{10}$$

No evidence is seen for $\eta^o\pi^-$ resonances other than the A_2^-.

(c) $\pi^- p \to X^{--}\pi^+ p$: the effective mass spectrum $\pi^+ p$ shows a strong $\Delta^{++}(1232)$ signal. No evidence for an exotic X^{--} meson is present either in the total spectrum or in the X^{--} opposite to $\Delta^{++}(1232)$.

(d) $\pi^- p \to \pi^-\pi^o p$: the ρ^- and g^- are seen and the statistical tensors of the $\pi^-\pi^o$ decay are presented and discussed.

(e) $\pi^- p \to \pi^+\pi^-\pi^- p$: general features of the mass spectra for different sectors in longitudinal phase space are shown and a partial wave analysis of the $(3\pi)^-$ system is presented.

(f) $\pi^- p \to \pi^o\pi^+\pi^-\pi^- p$: in the $(4\pi)^-$ mass spectrum the $A_2^- \to \eta\pi^-$, $B^- \to \omega\pi^-$ and $g^- \to (4\pi)^-$ are observed and studied.

(g) $\pi^- p \to 2\pi^+ 3\pi^- p$: the mass spectra are shown and an enhancement is seen in the $2\pi^+ 2\pi^-$ mass spectrum at 1.27 GeV.

(h) $\pi^- p \to \pi^o 2\pi^+ 3\pi^- p$: the η' and D^o are observed in the $\eta^o\pi^+\pi^-$ decay mode.

2. EXPERIMENTAL SET UP

The layout of the Omega Spectrometer as used in this experiment is shown in fig. 1. The trigger has been described in a previous paper [4]. Essentially it consisted of measuring with a large scintillation counter the time-of-flight of a slow proton originating from an interaction in the hydrogen target. By choosing the time-of-flight interval, a region of missing mass (X^-) to the proton was selected. The experiment was run so that masses between 1.0 and 2.2 GeV had their acceptance limited only by the geometry of the slow proton counter. The variation of the acceptance with the missing mass and with the four-momentum transfer (t) to the proton for three values of the missing mass X^- are shown in figs 2(a) and 2(b) respectively. The charged particles arising from the reaction were detected in a system of optical spark chambers arranged around the hydrogen target. The sparks were viewed by stereoscopic pairs of Plumbicon cameras which digitised their positions and recorded them on magnetic tape for subsequent analysis. The entire system of hydrogen target and spark chambers was situated in the 18 kG magnetic field of the Omega magnet and thus enabled the momentum of charged particles to be measured. A more detailed description of the apparatus can be found in ref. [5]

An example of a 4-prong event, as displayed on-line during the run, is shown in fig. 3.

3. DATA REDUCTION

A total of 3.3×10^6 triggers was recorded in two runs, one with a 30 cm and the other with a 60 cm long liquid hydrogen target. The data were processed through a modified version of the automatic pattern recognition and geometry reconstruction program ROMEO [6]. The slow proton was identified by tracing positive tracks to the proton counter and demanding agreement to within $\pm$ 5 ns between the time-of-flight (TOF) as calculated from the track momentum and that recorded electronically. This procedure yielded 1.272×10^6 events which were then processed through the kinematic fitting program KOMEGA [6]. Our ability to provide

an absolute normalization was tested by calculating the differential cross section for elastic scattering and comparing with other experiments in this energy region. Good agreement was obtained [4].

4. RESULTS ON MISSING MASS SPECTRA

4.1 $\pi^- p \to X^- p$

The missing mass spectrum to the recoil proton in $\pi^- p$ interactions was studied in a series of experiments by the CERN Boson Spectrometer (CBS) group [1] and aroused considerable interest due to the evidence from their analysis that several narrow boson states were present in the 1.7 GeV region of mass. However, a subsequent experiment by the North Eastern Stony Brook (NESB) Collaboration [2] with higher statistics did not confirm the original result. Figs 4(a) and 4(b) show the missing mass squared (MM^2) and missing mass (MM) respectively to the slow recoil proton of reaction (1) for the present experiment. The numbers of events and the resolution in MM^2 (which is independent of MM^2) of our experiment, averaged over the t range, is compared with the NESB experiment in table 1. The resolution evaluation has been checked by computing the mean error on the MM^2 to the proton for elastic events and comparing it with the width of the pion peak. As can be seen from fig. 4(a), apart from the broad enhancements in the 1.3 and 1.7 GeV mass regions, no evidence is seen for either narrow structures or other broad enhancements below 2.2 GeV. The A_1 resonance which we might have expected to observe, has been suppressed because the acceptance falls to zero for $|t|$ values below 0.1 GeV^2 (fig. 2).

The missing mass squared for the 2 and 4-prong charge conserving samples are shown in figs 4(c) and 4(d). Signals are evident in the ρ and A_2 mass regions in the 2-prong sample but no evidence of a $\delta^-(980)$ meson is seen [7].

4.2 $\pi^- p \to X^0 \pi^- p$ and $X^0 \pi^{\pm} \pi^- \pi^- p$

Fig. 5 shows the X^0 mass spectrum opposite the $p\pi^-$ for all topologies where, in addition to the shoulder at the η^0 and the peak at

the ρ^o/ω^o, a signal is seen at a mass of $\sim$ 1.28 GeV. In this region contributions may be expected from many resonances (e.g. A_2^o, f^o, B^o, D^o). In order to see if part of this signal can be associated with the known decay of the D^o meson to $\eta^o\pi^+\pi^-$ we looked for evidence of an η^o signal in the MM to the 4-prong charge conserving events, assumed to be events of the type $\pi^- p \to \pi^+\pi^-_f\pi^-_s pX^o$, where f, s refers to the faster, slower π^- in the laboratory system. Fig. 6(a) shows the mass spectrum of X^o from 373, 769 events, where an η^o signal containing $\sim$ 4000 η^o is seen. Selecting X^o in the η^o region ($0.50 < M(X^o) < 0.58$ GeV) and plotting in figs 6(b) and 6(c) the mass $\eta^o\pi^+\pi^-_s$ and $\eta^o\pi^+\pi^-_f$ respectively reveals a peak only in the $\eta^o\pi^+\pi^-_s$ combinations (fig. 6(b)) at a mass corresponding to the D^o meson. A fit to a Breit-Wigner and a polynomial background gives a mass and width, after unfolding the resolution of σ = 21.5 MeV,

$$M = (1.278 \pm .004)\text{GeV}$$
$$\Gamma = (26 \pm 12)\text{MeV},$$

which are compatible with the world averaged values for the D^o meson. The fact that the D^o signal is associated mainly with the slow $\pi^-(\pi^-_s)$ agrees with the observation of Grässler et al. [8]. Fig. 6(d) displays the $\eta^o\pi^+\pi^-$ mass spectrum where the events with a missing mass X^o lying in the η^o band have had their mass X^o fixed at the η^o mass. An η' signal is seen which, like the D^o, is also preferentially produced with a fast bachelor π^-. Figs 7(a), 7(b), 8(a) and 8(b) show respectively the $\eta^o\pi^+\pi^-\pi^-$, $\eta'\pi^-_f$, $D^o\pi^-_f$ and $D^o p$ mass distributions where the D^o is defined by the mass cut (1.24 - 1.32)GeV. No evidence for resonance structures is seen.

From these observations a picture emerges of central η' and D^o production, a feature which would not be inconsistent with the speculations in the literature that the η' consists of 72% gluons [9,10] and that the D^o is a glueball [11]. The relatively narrow width of the D^o also points in this direction.

The $\eta^o\pi^{\mp}$ mass spectrum (fig. 9) from events having an $\eta^o\pi^+\pi^-_s$ mass combination lying in the D^o region reveals an enhancement in the $\delta^{\pm}$ region which corresponds to $\sim$ 500 events. This observation is consistent with the $\eta^o\pi^+\pi^-_s$ decay of the D^o arising almost completely from the intermediate state $\delta^{\pm}\pi^{\mp}$. A fit to this $\eta^o\pi^{\pm}$ mass spectrum with an S wave Breit-Wigner, a polynomial background and folding in the experimental resolution results in a mass and width for the δ of

$$M = (0.986 \pm .003)\text{GeV}$$
$$\Gamma = (62 \pm 15)\text{MeV}.$$

In the missing mass distribution $M(X^o)$ for the 2-prong charge conserving events shown in fig. 10 an η^o signal of some 3600 events can be seen. The $\eta^o\pi^-$ mass spectrum displayed in fig. 11 shows no evidence for any resonance other than the A_2^-.

4.3 $\pi^- p \to X^{--}\pi^+ p$

The effective mass spectrum of $p\pi^+$ for 696 178 events (fig. 12(a)) shows evidence for $\Delta^{++}(1232)$ production. The "exotic" MM^2 spectrum X^{--} for events with a $p\pi^+$ mass between 1.15 and 1.27 GeV (fig. 12(b)) shows no evidence of narrow structures which could be attributed to resonance production. Relaxing the criteria on the $p\pi^+$ mass and plotting the mass X^{--} opposite the $p\pi^+_s$ combination (fig. 12(c)) also shows no structure.

5. THE CHANNEL $\pi^- p \to \pi^-\pi^0 p$ (42 705 EVENTS)

5.1 Event selection

The 2-prong charge conserving events were fitted to the reactions

$$\pi^- p \to \pi^-\pi^o p \tag{11}$$

$$\to K^- K^o p \tag{12}$$

$$\to \bar{p}n\, p. \tag{13}$$

The ambiguity between reaction (11) and reactions (12) or (13) has been resolved by accepting hypothesis (11) if the probability for the other hypotheses is less than 20%. If the probability is > 20% for hypothesis (12) or (13) the event remained ambiguous and was not used in the analysis. The contamination by multi-neutrals has been reduced by applying cuts for reaction (11) at 20% probability and $|MM^2| < 0.2$ GeV^2. Fig. 13 shows the MM^2 distribution after this selection. The asymmetry shows that there still remains some contamination of the $\pi^-\pi^o p$ fits by events with multi-neutrals (estimated to be 13%).

Reaction (13) has been separately studied [12].

5.2 Mass spectra

The $\pi^-\pi^o$ mass spectra unweighted and weighted for the acceptance (fig. 14(a)) show evidence for the ρ^- and g^- mesons. Baryon resonances in the $p\pi^-$ and $p\pi^o$ systems (fig. 14(b) and 14(c)) give rise to an accumulation of events at high masses in the $\pi^-\pi^o$ spectrum. Excluding the events with a $p\pi^o$ mass < 1.8 GeV gives the distribution shown in fig. 14(d) where the g^- is more clearly seen. Fitting the weighted $\pi^-\pi^o$ mass spectrum up to a mass of 2 GeV with a third order polynomial background and two relativistic Breit-Wigner resonance shapes with appropriate angular momentum barrier factors gives for values of the mass and width of the ρ^- and g^-

$$
\begin{aligned}
M(\rho^-) &= (0.763 \pm .002)\text{GeV} \\
\Gamma(\rho^-) &= (134 \pm 7)\text{MeV} \\
M(g^-) &= (1.677 \pm 0.014)\text{GeV} \\
\Gamma(g^-) &= (246 \pm 37)\text{MeV} .
\end{aligned}
$$

5.3 Analysis of the $\pi^-\pi^0$ angular distribution

The angular distributions of the $\pi^-\pi^o$ system are distorted by the presence of low mass resonances in the $p\pi^o$ channels. The exclusion of these (selecting $M(p\pi^o > 1.8$ GeV) leads to "holes", i.e. regions with zero events, in the ($\cos\theta$, ϕ) Jackson decay distribution of the $\pi^-\pi^o$

system. Examples can be seen in figs 15(a) and 15(b), where events having a $\pi^-\pi^o$ mass in the ρ^- and g^- regions respectively, have been subjected to these cuts. We note that this procedure for excluding isobar resonances also allows us to overcome the problem of correcting for slow pion losses: in fact, slow pions contribute only to small $p\pi$ masses and it has been checked (both with Monte-Carlo simulated events and real events) that no charged pions with momenta less than 1 GeV/c are present in the sample remaining after the $p\pi$ cuts. On the other hand the pion loss in Omega is < 2% above 1 GeV/c as we found in recuperating events of reaction (5) via a one-constraint fit which recovered the lost pions (sect. 6.1).

The situation of the decay angular distribution is then similar to that occurring in many spectrometer experiments, where holes are produced by the acceptance of the apparatus. Introducing an "acceptance", which is defined to be zero in the holes and 1.0 outside, the standard method of linear algebra [13] can be used to compute the statistical tensors t_ℓ^m of the expansion

$$W(\cos\theta,\ \phi) = \sum_{\ell,m} t_\ell^m \ \mathrm{Re}\ Y_\ell^m\ (\cos\theta,\ \phi)\ .$$

The $\pi^-\pi^o$ mass spectrum was divided into bins 100 MeV wide from 0.5 to 2.0 GeV and for each bin the linear algebra method was applied introducing moments up to $\ell = 10$ and $m = 4$. As a second iteration, the fits were redone setting to zero the statistical tensors which were consistent with zero in the first fits except t_6^2, t_7^o and t_8^o. The results are displayed in fig. 16.

In the ρ^- region a strong negative signal is present in t_2^2 and a smaller signal, also negative, in t_2^o. It is possible to express the tensors (assuming that L is the maximum wave present) in the form [14]

$$t_{2L}^o = C_1\ |L_o|^2 - C_2(|L_-|^2 + |L_+|^2$$

$$t_{2L}^1 = C_3\ \ \mathrm{Re}(L_o L_-^*)$$

$$t_{2L}^2 = C_4(|L_-|^2 - |L_+|^2)\ ,$$

(where C_1 to C_4 are known positive coefficients, L_o is the spin L

helicity zero amplitude produced by unnatural parity exchange in the t channel and L_+ are the spin L helicity one amplitudes produced by natural and unnatural parity exchange respectively). From the observed behaviour of t_2^o and t_2^2 one can deduce the dominance of natural parity exchange (e.g. ω^o, A_2^o) in the ρ^- production $|t| > 0.2$ GeV^2.

In the 1.7 GeV region a positive signal is observed in t_6^o while t_6^1 and t_6^2 are small or compatible with zero, as well as t_7^o and t_8^o thus indicating the presence of a spin 3 object (which we identify with the g^-) produced via helicity zero unnatural parity (e.g. π) exchange.

5.4 Cross sections

The differential cross sections for the ρ^- and the g^- mass regions (fig. 17) were fitted to the form $dN/dt = Ae^{-b|t|}$ in the $|t|$ regions 0.21 to 0.44 GeV^2 for the ρ^- and 0.17 to 0.42 GeV^2 for the g^- where the acceptance is purely geometric. The slopes obtained were $b(\rho^-) = (8.8 \pm 0.4)$ and $b(g^-) = 6.3 \pm 0.3)$ GeV^{-2}.

The cross section determined for these t intervals are

$$\Delta\sigma(\rho^-) = (10.2 \pm 0.5)\mu b$$
$$\Delta\sigma(g^-) = (2.5 \pm 0.3)\mu b.$$

6. THE CHANNEL $\pi^- p \to \pi^- \pi^- \pi^+ p$ (128 404 EVENTS)

6.1 Event selection

The final state $p\pi^+\pi^-\pi^-$ which appears in Omega as a 4-prong topology is selected after kinematic fitting as a four-constraint hypothesis. In a certain fraction of cases the apparatus or the reconstruction program fails to detect one of the pions, usually of low momentum, while in other cases a spurious track is attached to the vertex. The first loss (40%)(*) was

(*) This loss reduces to 25% when events are selected for the Partial Wave Analysis (PWA).

recovered by one-constraint kinematic fitting and it was found possible to eliminate cleanly the spurious track in the second case (5%). Suitable cuts on the fit probability and missing mass squared were applied resulting in a sample of 128 404 events. Study of the $p\pi^-$ mass spectrum shows that in 6% of this channel a Λ^o satisfied the trigger and has been incorrectly associated to the primary vertex. These are eliminated by a cut on the $p\pi^-$ mass. In addition there is an unresolved contamination from the $pK^+K^-\pi^-$ channel which is estimated to be at the 2% level.

6.2 General features of the mass spectra

The total $\pi^+\pi^-\pi^-$ mass spectrum, (fig. 18(a)) shows A_2^- and A_3^- signals. No signal above the A_3 is evident. The total $\pi^+\pi^-$ mass spectrum (fig. 18(e)) shows strong ρ^o, f^o production and possibly some g^o production.

Effective mass distributions for $\rho^o\pi^-$, $f^o\pi^-$ and $g^o\pi^-$ selections (figs 18(b), 18(c) and 18(d)) show how the A_2^- and A_3^- are associated with the $\rho^o\pi^-$ and $f^o\pi^-$ selections respectively. No enhancement is seen in the $g^o\pi^-$ distribution although evidence for an enhancement around 2.10 GeV has been suggested in previous studies [15,16]. Results on a detailed partial wave analysis of the 3π system are presented in sect. 7 below.

The $p\pi^+$ mass spectrum (fig. 19(a)) shows a large $\Delta^{++}(1232)$ signal. The mass distribution of the exotic $\pi^-\pi^-$ system for events with a $p\pi^+$ mass lying in the Δ^{++} region viz. $M(p\pi^+) < 1.4$ GeV (fig. 19(b)) shows no evidence of resonance structure. Combining those $p\pi^+$ mass combinations lying in the Δ^{++} region with a π^- indicates that the peak at 1.70 GeV seen in the $p\pi^+\pi^-$ mass spectrum (fig. 20(a)) is mainly associated with $\Delta^{++}\pi^-$ (fig. 20(b)).

6.3 Longitudinal phase-space analysis

The distribution of events on the Longitudinal Phase-Space plot (LPS), where the

$$x(= 2p^*_{iL}/\sum_1^4 |p^*_{iL}|)$$

of the slowest negative pion has been plotted against the x of the positive pion, is shown in fig. 21 along with the kinematic configuration corresponding to each sector.

Sector 1 is dominated by the A_2^- and A_3^- mesons (fig. 22(a)). Fig. 22(b) shows the $\pi^+\pi^-$ mass distribution for events in sector 1 where the ρ^o and f^o mesons are evident. The $p\pi^+$ and $p\pi^-$ mass distributions (not shown) show no evidence for baryon resonances.

Sector 2, as might be guessed from the kinematic configuration, shows (fig. 23(a)) production of the $\Delta^o(1232)$ and N^* in the mass regions 1.53 and 1.7 GeV. The $\pi^+\pi^-$ mass distribution shows the ρ^o and f^o resonances which remain with little background when the combination with the fastest π^- is plotted (fig. 23(b)). Some overflow, from sector 1 of the A_2^- and A_3^- states is seen in the $\pi^+\pi^-\pi^-$ mass spectrum (not shown), but no evidence is seen for Δ^o or N^{*o}'s in the $M(p\pi_f^-)$ spectrum or Δ^{++} in the $M(p\pi^+)$ spectrum which suggests the LPS sectors separate rather well the different kinds of quasi 2-body reactions.

Sector 3 isolates an almost background free Δ^{++} signal (fig. 24(a)). The $\pi^-\pi^-$ mass spectrum is shown in fig. 24(b). The $p\pi^+\pi^-$ mass spectrum for sector 4 (fig. 25) shows signals at the 1.53 and 1.7 GeV.

7. PARTIAL WAVE ANALYSIS OF THE $\pi^+\pi^-\pi^-$ SYSTEM

We present in this section the results of a PWA of the 3π system over the mass range 1.0 - 2.0 GeV using the University of Illionis' program [17]. This assumes that the production process may be represented by

$$\pi^- p \to p + (3\pi)^- \hookrightarrow (\pi^+\pi^-)_R + \pi^- ,$$

where $(\pi^+\pi^-)_R$ is a resonant dipion such as a ρ^o, f^o or ε^o. In fact, the final p3π state is also produced to a significant extent by processes of the type

$$\pi^- p \to \Delta^{++} + \pi^- + \pi^-$$
$$\to N^{*o} + \pi^+ + \pi^- \quad .$$

This is dealt with by excluding from the analysis all events with a $p\pi^+$ combination of mass less than 1.4 GeV or a $p\pi^-$ combination of mass < 1.6 GeV. These cuts are allowed for in the normalization integrals. In addition to this cut, data were used only in the range $0.2 \leq |t| \leq 0.4$ GeV^2. This ensures that the data analyzed lies in a region where the experimental acceptance is well understood and has no rapid variations (fig. 2). After these selection criteria are applied the sample contained 38 226 events. The acceptance of the trigger affects only the recoil proton and hence the decay of the 3π system does not depend on it. Therefore, the fit does not formally include the trigger acceptance. However, we have checked that including the acceptance does not change the results. In the fits the ρ^o, f^o mesons have been represented by Breit-Wigner functions and the ε by the $\pi\pi$ phase shifts [13].

7.1 Results of the PWA

We first of all present those features of the mass dependence of the various waves which do not change when other waves are included or removed from the fit. We then discuss the phase of the waves whose mass dependence shows a clearly resonant like shape and compare our data with other experiments. This will be followed by considering any remaining possible structures. The section will then be closed by a study of the production properties in the A_2 and A_3 regions.

A bubble chamber experiment at the nearby energy of 11.2 GeV [18] is used to indicate which states may be important in the fit. We have examined the properties of all states of spin parity $\leq 3^{\pm}$, for the case of production by both natural parity exchange and unnatural parity exchange. Adding states not already used in the analysis of Thomson et al. [18] we have

found no extra state which requires to be included. The PWA program also allows the possibility of including in the fit an uncorrelated decay into 3π. This has been tried but found to be unnecessary.

The 14 states, which we retain as candidates for the fit are listed in table 2(a); where there are listed in addition those states which are required for the study of specific regions e.g. the A_2 region but which are not included in the general fits.

7.1.1 Mass dependence of the fit

We first of all tried a fit using the main states of table 2(a) (14 in all). Examination of the resulting mass dependence of this fit (fit A) showed that some waves are present only to a slight degree if at all. We then carried out a fit (fit B) with only those states (10 in all) where the state was required in at least part of the mass range (table 2(b)). The results of fit B are shown in fig. 26.

The following features were seen:

(a) At lower masses the $J^P \ell M_\eta = 1^+ S0+ (\rho\pi)$ wave is dominant, forming a structure centred at $\sim$ 1.2 GeV with a width of $\sim$ 300 MeV. This is probably associated with the shoulder seen in the 3π mass spectrum below the A_2 peak (fig. 18(a)), which we identify as the A_1 meson and which has been strongly suppressed in the mass plot by the effects of the trigger.

(b) Above this, there is a peak centred at $\sim$ 1.3 GeV in the 2^+D 1+ $(\rho\pi)$ wave. This we identify with the A_2 meson. The shape of this peak, up to a mass of 1.5 GeV^2, is well represented by a relativistic Breit-Wigner and a second order polynomial background and yields a mass and with of

$$M = (1.310 \pm .002)\text{GeV}$$
$$\Gamma = (97 \pm 5)\text{MeV}.$$

(c) Above the A_2 region, the dominant wave is the 2^-SO+ ($f\pi$) wave which begins to increase above 1.4 GeV, reaches a maximum $\sim$ 1.7 GeV and has a width of $\sim$ 250 MeV. This corresponds to the peak seen in the mass plot of $f^o\pi^-$ combinations which we associated with the A_3. A fit to the structure with an S wave relativistic Breit-Wigner and no background yields

$$M = (1.676 \pm .006)\text{GeV}$$
$$\Gamma = (260 \pm 20)\text{MeV}.$$

(d) All other waves except for the 0^-SO+ ($\varepsilon\pi$) wave discussed in the next section are relatively featureless compared to these structures.

7.1.2 Phase variarions of the A_1, A_2 and A_3 waves

A partial wave analysis does not determine an absolute phase variation, but only gives the variation relative to some wave chosen as reference. Normally the reference wave is chosen to be one that has little mass variarion in the hope that the phase of that wave is itself not varying and hence that the relative phase measured mirrors the changes of the absolute phase of the wave under study. For the A_2 resonance the 2^-PO+ ($\rho\pi$) wave have been used as reference wave. The phase relative to this wave (fig. 27) shows the classical 180° variation over the mass peak, suggesting that in this mass range the 2^-PO+ wave has little absolute phase variation.

For the A_1 region, the 2^-PO+ ($\rho\pi$) wave has therefore been used as a reference wave. A phase variation of approximately 70° is observed (fig. 28(a)) over the mass range (1.0 - 1.4)GeV. Since it is known that the A_2 is a true resonance, we can also investigate the nature of the A_1 by using the 2^+D1+ ($\rho\pi$) wave as reference and correcting for the effect of the varying phase of the A_2 Breit-Wigner. This is shown in fig. 28(b) where a phase change of $\sim$ 70° across the A1 structure is also observed.

The phase of the 1^+SO+ wave relative to the 0^-SO+ wave is found to be approximately constant (fig. 28(c)). Since fig. 26 shows evidence of a

weak enhancement, above a rising background, in the mass region around 1.3 GeV, it is possible that the relative constancy of the $1^+SO+/0^-SO+$ phase indicates a resonant structure in the 0^-SO+ wave itself. Fig. 28(d) shows the phase of the 0^-SO+ wave using the 2^-PO+ wave as reference, where some indication of a rising phase is observed. A fit to the 0^-SO+ mass variation using a relativistic Breit-Wigner and a polynomial background gives values of mass and width of

$$M = (1.342 \pm 0.02)\text{GeV}$$
$$\Gamma = (220 \pm 70)\text{MeV}.$$

However, the uncertainties in the phase determination are such that we do not feel that the data, though suggestive, justifies claiming the existence of a resonant state in this wave.

For the A_3 region, three reference waves have been tried: 1^+PO+ ($\varepsilon\pi$), 0^-SO+ ($\varepsilon\pi$) and 2^+D1+ ($\rho\pi$). As can be seen in fig. 29 no clear picture emerges. The phase relative to 0^-SO+ has no regular behaviour perhaps indicating some structure in the 0^-SO+ wave itself; that relative to 1^+PO+ shows the usual slow increase in phase that has been observed in several experiments while that relative to 2^+D1+ (which as the high mass tail of the A_2 might have little absolute phase variation) shows a variation of 120° across the peak suggesting resonant behaviour. However, for this relative phase the errors are large and the fit is not too stable. We conclude that our evidence is insufficient to establish that the A_3 is resonant.

We now compare our data to previous experiments. There have been many experiments studying the production and decay of 3π systems [18-24]. Until recently, experiments studying the 3π system produced opposite a proton have observed, in addition to the well established A_2 resonance, two other resonant-like structures in the mass distributions at a mass of $\sim$ 1.1 GeV (A_1) and $\sim$ 1.64 GeV (A_3). However, since the phase increase across the mass peaks was small it was not possible to establish these structures as resonant.

An experiment by Pernegr et al. [23], studying the coherent production of 3π systems off nuclei have found evidence for a resonant phase behaviour for the A_1 meson. Their experiment can involve different production mechanisms for the 3π system from those in our experiment. The phase variation they observe is of a complex nature and it is not possible to make a clear comparison between that experiment and ours.

Recently Daum et al. (a),(b),(c)[24] in a high statistics PWA of the $p\pi^+\pi^-\pi^-$ system produced at energies of 63 and 94 GeV have presented evidence that the A_1 has a resonant component near 1.3 GeV masked by a Deck amplitude, and that the A_3 can be interpreted as a true resonance.

For the A_1 meson, they find considerable dependence of the mass distribution of the 1^+SO+ wave on the t' range considered (b)[24]. The t' range in their data most similar to ours is $0.15 \leq t' \leq 0.3$ GeV^2, and comparing that data with ours shows some difference in the mass dependence. Our data has a larger component at low mass and is more similar to their data in the t' range $0.05 \leq t' \lesssim 0.7$ GeV^2.

Despite this differing mass dependence, the phase relations are similar. Of the reference waves used by Daum et al., the 0^-PO+ wave is not important in our data, but the phase of the 1^+SO+ with respect to the 2^-PO+ and with respect to 2^+D1+ (corrected for the Breit-Wigner phase of the A_2) show similar behaviour to that of ref. (b)[24]. Furthermore, when the 0^-SO+ wave is used as reference, both experiments show only a slowly rising phase.

For the A_3 meson, both experiments show an almost identical mass distribution for the 2^-SO+ wave, as can be seen by comparing the masses and widths obtained in the two experiments.

7.1.3 Other structures in the mass dependence

There have been suggestions from other partial wave analyses of the existence of possibly resonant states occurring in the 3π system, produced relatively weakly compared to the A_1, A_2 and A_3 mesons. We have

searched for these but, apart from the 0^-S0+ wave discussed in the previous section, are unable to present any which we regard as significant. While a number of structures appear, some of which are consistent with previous suggestions these are not stable with regard to changes in the number of waves in the fit.

7.1.4 Production properties in the A_2, A_3 regions

If all possible values of M, and production by both natural and unnatural parity exchange is considered for a given J^P state, the partial wave analysis allows the determination of the density matrix (real and imaginary parts) for that state. We have followed this procedure for the A_2 and A_3 regions. In such a study, a wide mass range is considered, the mass variation being represented by an appropriate Breit-Wigner shape. For the A_2 and A_3 regions the values of mass and width quoted in previous sections are used.

The values of the density matrix elements found for A_2 production are presented in table 3(a) together with results from other experiments for comparison. The main features are the dominance by natural parity exchange processes ($\sim$ 98%) and the dominance of production of the A_2 in a helicity 1 state ($\sim$ 82%).

The density matrix for the A_3 region is given in table 3(b). Again, over the t range of our experiment, production is mainly by natural parity exchange ($\sim$ 90%) and it is predominantly ($\sim$ 75%) produced in a helicity zero state. Indeed within the errors, our data are compatible with no production by unnatural parity exchange at all.

7.1.5 Cross sections

The cross section for A_2 production has been evaluated by integrating the mass dependence of the 2^+D1+ wave. A correction for the t cut used in our analysis has been made by assuming the dependence [21]

$$\frac{d\sigma}{dt'} \alpha\ t' e^{-8.3t'} .$$

This gives a result (after correction for the $\rho^-\pi^0$ decay mode and taking account of all possible helicity states of the A_2) of

$$\sigma(\pi^- p \to A_2^- p) = (86.4 \pm 6.4)\mu b,$$

which is compatible with the results of other experiments in this energy range.

For A_3 production, we have in the t range

$$0.2 \lesssim |t| \lesssim 0.4 \text{ GeV}^2$$

that

$$\sigma(\pi^- p \to A_3^- p) = (17.1 \pm 1.5)\mu b \ ,$$
$$\quad \big|\to f^o \pi^-$$
$$\quad\ \ \big|\to \pi\pi$$

where the $f^o \to \pi^o\pi^o$ has been allowed for and all helicity states of A_3 production are included. We correct for the missing t range using the result of Otter et al. [20] that at 16 GeV/c

$$\frac{d\sigma}{dt'} \propto e^{-(6.2 \pm 0.14)t'}$$

This yields the result

$$\sigma(\pi p \to A_3^- p) = (73 \pm 7)\mu b,$$

which is compatible with previous experiments [18].

8. THE CHANNEL $\pi^- p \to \pi^-\pi^-\pi^+\pi^0 p$ (84 149 EVENTS)

8.1 Event selection

The criteria used for selection are:

(a) Probability of the π^o fit > 5%.

(b) Events having also a fit to the four-constraint hypothesis (no π^o) and having a probability of > 1% for the 4C hypothesis were assigned to the 4C fit (3% of events).

(c) Events which have an ambiguous fit in which the proton mass could be assigned to either of the positive particles were solved by taking the more probable fit (6% of events).

After applying these criteria 84 149 events were selected representing a sample of about three times that previously reported in this energy range [25,26]. As with the four-constraint channel, events were lost due to either a track not being found (3-prong event) or an extra track being associated to the vertex (5-prong event). Whereas the latter could be recovered by eliminating the spurious track, the former is not solvable in the case of a one-constraint fit. This represents a serious handicap if one wishes to study angular distributions.

8.2 General features of the mass spectra

The mass distributions of the $p\pi^+$, $p\pi^o$ and $p\pi^-_s$ systems (fig. 30(a,b,c)) shows evidence for the $\Delta(1232)$ in the $p\pi^+$ and $p\pi^o$ but not in the $p\pi^-$ system. In the $p2\pi$ combinations, not shown, only a small signal at 1.68 GeV is observed in the $p\pi^-\pi^o$ system. The $\pi^+\pi^-$, $\pi^-\pi^o$ and $\pi^+\pi^o$ mass spectra (fig. 31) shows ρ signals and the η^o and ω^o are seen as narrow signals in the $\pi^+\pi^-\pi^o$ mass spectra of fig. 32(a). The A_2^o and a shoulder in the 1.0 GeV region is also present in this figure. Fig. 32(b) shows the same spectra in 10 MeV bins and a peak is seen above the ω^o centred at 985 MeV. In the $\rho^o\pi^o$ mass spectrum (not shown) the peak is retained almost entirely. We may interpret this peak as a reflection of the $\eta' \to \pi^+\pi^-\gamma$. The corresponding $\pi^+\pi^-\gamma$ mass spectrum does indeed show a peak at 960 MeV so that, since we have seen evidence of the $\eta' \to \eta^o\pi^+\pi^-$ in a similar production reaction viz $\pi^- p \to \pi^-\eta' p$ (fig. 6(b,c)), the $\eta' \to \pi^+\pi^-\gamma$ decay hypothesis is probably the correct interpretation.

Fig. 33(a) shows the $\pi^-\pi^-\pi^+$ spectrum, where A_2^- production is visible. This signal is enhanced (fig. 33(b)) selecting the events with a $\pi^+\pi^-$ lying in the ρ^o band ($0.64 \lesssim M(\pi^+\pi^-) \lesssim 0.88$ GeV) and a $p\pi^o$ lying in the Δ^+ band ($M(p\pi^o) \lesssim 1.32$ GeV). No signal is detected in the A_1 region.

Fig. 34 displays the four pion effective mass spectrum. An enhancement is visible at $\sim$ 1.25 GeV and a broad shoulder appears in the 1.7 GeV mass region. As known from previous experiments these enhancements are due to the overlapping of different decay modes of various states which we study in more detail below.

8.2.1 The $\eta^0\pi^-$ mass spectrum

Selecting on the $\eta^0(0.53 \lesssim M(\pi^+\pi^-\pi^0) \lesssim 0.57$ GeV) and plotting the $\eta^0\pi^-$ effective mass (fig. 35, 1462 events) brings out a clean A_2^- signal, no δ^- at 960 MeV but an apparent excess of events around 1.82 GeV, which still remains if the Δ's are removed. However, the $\eta^0\pi^-$ spectrum of fig. 11 does not confirm the signal. A scatter plot of $\cos\theta_J$ vs ϕ_J, where θ_J and ϕ_J are the Gottfried-Jackson decay angles for the $\eta^0\pi^-$ system in the A_2^- region (fig. 36), shows the distribution expected of a $J^P = 2^+$ state. The asymmetry in $\cos\theta_J$ is probably associated with the loss of slow π's in the laboratory system.

8.2.2 The $\omega^0\pi^-$ mass spectrum

The $\omega^0\pi^-$ mass spectrum (ω^0 selected in the range $0.75 \lesssim M(\pi^+\pi^-\pi^0) \lesssim 0.81$ GeV, Δ^+, Δ^{++} removed), (fig. 37), shows signals in the B meson region at 1.24 GeV and the g region at 1.70 GeV, the latter of which is similar in mass and width to the $\pi^-\pi^0$ signal seen in fig. 14(a). A fit to the mass spectrum with relativistic Breit-Wigner functions for the B^- and g^- and a smooth background gives the following parameters:

$$M_B = (1.239 \pm 0.005)\text{GeV}, \quad \Gamma_{B^-} = (170 \pm 15)\text{MeV}$$

$$M_g = (1.690 \pm 0.015)\text{GeV}, \quad \Gamma_{g^-} = (190 \pm 65)\text{MeV}.$$

Although, as stated in the introduction, the losses of the slow pions make a detailed study of angular distributions not possible we have nevertheless carried out a PWA of the $\omega\pi^-$ system in the 1.2 GeV mass region which allows us to conclude that the dominant wave is 1^+, consistent with the assigned quantum numbers for the B meson.

8.2.3 4π mass spectrum (no η^0, no ω^0)

The $\pi^-\pi^-\pi^+\pi^0$ mass spectrum after anti-selection of the events lying in the η^0, ω^0, Δ^+ and Δ^{++} bands is shown in fig. 38(a). A broad shoulder is still visible in the (1.6 - 1.8)GeV region over a large background. This shoulder as known from previous experiments, is expected to be related to the g meson decay into 4π. As shown in fig. 38(b) this structure is enhanced if a ρ^- and a ρ^0 selection is imposed ($.64 \leq M(2\pi) \leq .88$ GeV). A fit of a fifth order polynomial background and a Breit-Wigner gives resonance parameters

$$M = (1.694 \pm 0.006)\text{GeV}$$
$$\Gamma = (123 \pm 13)\text{MeV}.$$

It is well known that due to the Q value of the $g \to 4\pi$ decay it is difficult to separate $\rho\rho$ from $A_2\pi$ decays. Indeed as shown in fig. 38(c,d), the $A_2^0\pi^0$ mass spectra (A_2 defined as $1.24 \leq M(3\pi) \leq 1.40$ GeV where the 3π system contains a ρ combination) shows a large structure in the g region. Fits using a fifth order polynomial plus a Breit-Wigner give for the resonance the following parameters in the case of $A_2^-\pi^0$

$$M = (1.718 \pm 0.010)\text{GeV}, \quad \Gamma = (230 \pm 28)\text{MeV}$$

and in the case of $A_2^0\pi^-$

$$M = (1.673 \pm 0.009)\text{GeV}, \quad \Gamma = (184 \pm 33)\text{MeV}$$

which are in agreement with those of the g^- meson ($g^- \to \pi^-\pi^0$).

9. THE CHANNEL $\pi^- p \to 3\pi^- 2\pi^+ p$ (8244 EVENTS)

Events were selected for this channel provided that the probability for the kinematic four-constraint fit was greater than 5%. A total of 8244 events were selected. Losses are considerable, we estimate our sample represents approximately one third of the total, and therefore we present only the salient features of the mass distributions.

9.1 Features of the mass spectra

The $\pi^+\pi^-$ mass distribution of fig. 39 shows a strong ρ^o signal ($\sim$ 8000 ρ^o). If we look at the $\pi^+\pi^-\pi^\pm$ mass distribution, where one might expect to see an A_2 meson at a mass of 1.3 GeV, a shoulder is present ($\sim$ 400 combinations above background), as can be seen in fig. 40. The $2\pi^+2\pi^-$ mass spectrum (fig. 41) shows a shoulder at 1.27 GeV which can be due to the superposition of the 4π decays of the f^o and D^o mesons.

Since the D^o meson is seen to decay into $\delta^\pm\pi^\mp$ (sect. 4.2) and the $2\pi^+2\pi^-$ mass spectrum enhancement at 1.27 GeV of fig. 41 can be due to the 4π decay mode of the D, we have looked for evidence of a $\rho^o\pi^\pm$ decay mode of the $\delta^\pm$. Fig. 42 which displays the $\rho^o\pi^\pm$ mass spectra, gives no evidence for a $\delta^\pm \to \rho^o\pi^\pm$ decay. In the $(5\pi)^-$ mass spectrum (fig. 43) we looked for signs of the enhancement reported by Baltay et al. [15] at a mass of 2.34 GeV but find no statistically significant signal.

10. THE CHANNEL $\pi^- p \to 3\pi^- 2\pi^+ \pi^o p$ (14 258 EVENTS)

This channel was selected from the kinematical fits provided it did not have a four-constraint fit and that its probability for the one-constraint π^o fit was greater than 5%.

10.1 Features of the mass spectra

The $\pi^+\pi^-\pi^o$ mass spectrum, shown in fig. 44, shows evidence for η^o and ω^o meson production. Selecting the η^o and plotting the $\eta^o\pi^+\pi^-$ mass spectrum produces signals for the $\eta'(958)$ and D^o mesons (fig. 45). The $\omega^o\pi^+\pi^-$ mass spectrum is shown in fig. 46 and has no significant structure, which is also true of the $(6\pi)^-$ mass spectrum shown in (fig. 47).

11. CONCLUSIONS AND DISCUSSION

We have studied the properties of the reaction $\pi^- p \to X^- p$ at 12 GeV/c in an experiment which triggered on the proton with $0.2 < |t| < 0.4$ GeV^2 and gave a mean sensitivity of 200 events/μb.

As a result of this study we make the following observations:

(a) In the missing mass spectrum X^- of the reaction $\pi^- p \to X^- p$ we confirm the absence of narrow peaks in the region of 1.7 GeV (i.e. the mass resolution, $\pm$ 24 MeV).

(b) In the reaction $\pi^- p \to \pi^- X^0 p$ we confirm the observation of a narrow peak in the X^0 mass spectrum at 1.28 GeV and show that this is associated with the D^0 meson decaying in the mode $\eta^0\pi^+\pi^-$. This D^0 is seen to be produced preferentially in association with a fast batchelor π^-. The $\eta' \to \eta^0\pi^+\pi^-$ is also observed in the X^0 mass spectrum and is also produced preferentially in association with a fast π^-.

The mass and width of the D^0 meson was measured to be

$$M(D^0) = (1.278 \pm .004)\text{GeV}, \quad \Gamma(D^0) = (26 \pm 12)\text{MeV}$$

in the final state $\eta^0\pi^+\pi^-$. The $\delta^\pm$ meson was observed via the decay of the D^0 to $\delta^\pm\pi^\mp$. The mass and width of the δ were measured to be

$$M(\delta) = (0.986 \pm .003)\text{GeV}, \quad \Gamma(\delta) = (62 \pm 15)\text{MeV}.$$

No signal other than the A_2^- (e.g. the δ^-) was observed in the $\eta^0\pi^-$ mass spectrum of the reaction $\pi^- p \to \eta^0\pi^- p$.

(c) In the exotic X^{--} mass spectrum observed in the reaction $\pi^- p \to X^{--}\pi^+ p$ no evidence for narrow exotic states was seen.

(d) In the reaction $\pi^- p \to \pi^- \pi^o p$ we observed the ρ^- and g^- mesons with mass and widths which were determined to be

$$M(\rho^-) = (0.763 \pm .002)\text{GeV}; \quad \Gamma(\rho^-) = (134 \pm 7)\text{MeV}$$
$$M(g^-) = (1.677 \pm .014)\text{GeV}; \quad \Gamma(g^-) = (246 \pm 37)\text{MeV}.$$

A moments analysis of the $\pi^- \pi^o$ angular distribution showed a strong negative t_2^2 moment in the ρ^- region indicating the dominance of natural parity exchange (ω^o, A_2^o) in ρ^- production. A positive signal was observed in t_6^o in the g^- region suggesting $J^P = 3^-$ for this state.

(e) In a partial wave analysis of the $(3\pi)^-$ system produced in the reaction $\pi^- p \to \pi^+ \pi^- \pi^- p$ we observe the A_2 and A_3 with masses and widths of

$$M(A_2) = (1.310 \pm .002)\text{GeV}, \quad \Gamma(A_2) = (97 \pm 5)\text{MeV}$$
$$M(A_3) = (1.676 \pm .006)\text{GeV}, \quad \Gamma(A_3) = (260 \pm 20)\text{MeV}$$

and the density matrix elements of their production were determined. These showed the dominance of natural parity exchange for both the A_2 and the A_3, with the A_2 being produced preferentially in a helicity 1 state and the A_3 preferentially in a helicity zero state. Evidence is presented suggesting a possible resonance in the 0^-S0+ wave with mass and width of $M = (1.342 \pm .02)\text{GeV}$ and $\Gamma = (220 \pm 70)\text{MeV}$. A phase variation of $\sim 70°$ was observed across the A_1 region.

(f) In the reaction $\pi^- p \to \pi^+ \pi^- \pi^- \pi^o p$ and B^- and g^- mesons were observed in the decay mode $\omega^o \pi^-$ with masses and widths

$$M(B^-) = (1.239 \pm .005)\text{GeV}, \quad \Gamma(B^-) = (170 \pm 15)\text{MeV}.$$
$$M(g^-) = (1.690 \pm .015)\text{GeV}, \quad \Gamma(g^-) = (190 \pm 65)\text{MeV}.$$

The g^- is also observed in the decay modes $\rho^- \rho^o$ and $A^o \pi^-$.

(g) In the reaction $\pi^- p \to 2\pi^+ 3\pi^- \pi^o p$ the η' and D^o were observed in the decay mode $\eta^o \pi^+ \pi^-$ ($\eta^o \to \pi^+ \pi^- \pi^o$).

(h) No evidence for high mass meson states decaying to $2\pi^+ 3\pi^-$ or $2\pi^+ 3\pi^- \pi^o$ was observed in either of the reaction $\pi^- p \to 2\pi^+ 3\pi^- p$ or $\pi^- p \to 2\pi^+ 3\pi^- \pi^o p$.

Acknowledgements

We should like to acknowledge the valuable support of both the hardware and the software Omega resident groups.

REFERENCES

[1] M.N. Foccacci et al., Phys. Rev. Lett. 17 (1966) 890.

[2] D. Bowen et al., Phys. Rev. Lett. 29 (1972) 890 and Phys. Rev. Lett. 30 (1973) 332.

[3] R. Thun et al., Phys. Rev. Lett. 28 (1972) 1733.

[4] B. Ghidini et al., Nucl. Inst. Meth. 147 (1977) 313.

[5] O. Gildemeister, Int. Conf. on Instrumentation for High Energy Physics, Frascati (1973).

[6] ROMEO User Manual (OM Development Note AP-12) CERN 1972 and D. Townsend CERN OM/SPS/11 (1976);
KOMEGA, CERN Hydra Application Library.

[7] W. Kienzle et al., Phys. Lett. 19 (1965) 438.

[8] H. Grässler et al., Nucl. Phys. B121 (1977) 189.

[9] N.H. Fuchs, Phys. Rev. D14 (1976) 1912.

[10] V.A. Novikov et al., Phys. Lett. 86B (1979) 347.

[11] D. Robson, Nucl. Phys. B130 (1977) 328.

[12] B. Ghidini et al., Nucl. Phys. B132 (1977) 189.

[13] G. Grayer et al., Nucl. Phys. B75 (1974) 189.

[14] R. Baldi et al., Phys. Lett. 74B (1978) 413.

[15] C. Baltay et al., Phys. Rev. D17 (1978) 62.

[16] Y.M. Antipov et al., Nucl. Phys. B119 (1977) 45.

[17] J.D. Hansen et al., Nucl. Phys. B81 (1974) 403.

[18] G. Thompson et al., Nucl. Phys. B101 (1975) 285.

[19] G. Ascoli et al., Phys. Rev. Lett. 25 (1970) 962.

[20] Y.M. Antipov et al., Nucl. Phys. B63 (1973) 153.

[21] Y.M. Antipov et al., Nucl. Phys. B63 (1973) 141.

[22] G. Otter et al., Nucl. Phys. B80 (1974) 1.

[23] J. Pernegr et al., Nucl. Phys. B134 (1978) 436.

REFERENCES (Cont'd)

[24] (a) C. Daum et al., Phys. Lett. 89 (1980) 276;
(b) C. Daum et al., Phys. Lett. 89 (1980) 281;
(c) C. Daum et al., Phys. Lett. 89 (1980) 285.

[25] R. Gessaroli et al., Nucl. Phys. B126 (1977) 382.

[26] A. Forino et al., Nucl. Phys. B139 (1978) 413.

TABLE 1

MISSING MASS RESOLUTION

MOMENTUM (GeV/c)	EVENT NOS.	MASS RESOLUTION $\delta(MM^2)$, GeV^2, (FWHM)	REFERENCE
12	1.272×10^6	0.16	This expt.
8	0.25×10^6	0.07	(2)
11	0.12×10^6	0.11	(2)
13.4	0.09×10^6	0.11	(2)
16	0.15×10^6	0.17	(2)

TABLE 2a

States used in fit A

State	$J^P{}_{Z}M_{\eta}$	Decay Mode	Use
1	1^+S0+	$(\rho\pi)$	General fit to all mass bins
2	1^+P0+	$(\varepsilon\pi)$	
3	2^-S0+	$(f\pi)$	
4	2^-P0+	$(\rho\pi)$	
5	2^-D0+	$(\varepsilon\pi)$	
6	1^+S1+	$(\rho\pi)$	
7	1^+P1+	$(\varepsilon\pi)$	
8	2^+D1+	$(\rho\pi)$	
9	2^+P1+	$(f\pi)$	
10	0^-S0+	$(\varepsilon\pi)$	
11	0^-P0+	$(\rho\pi)$	
12	3^+P0+	$(f\pi)$	
13	3^+D0+	$(\rho\pi)$	
14	3^+F0+	$(\varepsilon\pi)$	
15	2^+D2+	$(\rho\pi)$	A_2 density matrix measurement
16	2^+D0-		
17	2^+D1-		
18	2^+D2-		
19	2^-S1+	$(f\pi)$	A_3 density matrix measurement
20	2^-S2+		
21	2^-S1-		
22	2^-S2-		

$J^P{}_{Z}M_{\eta}$ refers to spin parity J^P, Z the orbital momentum between the dipion resonance and the bachelor pion, M the Z component of the spin and η the naturality of the exchange mechanism.

TABLE 2b

States used in fit B

State	$J^P{}_{ZMn}$	Decay Mode
1	1^+S0+	$(\rho\pi)$
2	1^+P0+	$(\varepsilon\pi)$
3	2^-S0+	$(f\pi)$
4	2^-P0+	$(\rho\pi)$
5	2^-D0+	$(\varepsilon\pi)$
6	2^+D1+	$(\rho\pi)$
7	0^-S0+	$(\varepsilon\pi)$
8	3^+D0+	$(f\pi)$
9	3^+D0+	$(\rho\pi)$
10	3^+F0+	$(\varepsilon\pi)$

TABLE 3a

Density Matrix for A_2

Density Matrix Element	This Experiment (12 GeV)	Ref(18) $p3\pi$ (11.2 GeV)	Ref(19) $p\eta\pi$ (11.2 GeV)	
ρ_{11}	0.413 ± .015	0.435 ± .11	0.43 ± .18	
ρ_{1-1}	0.405 ± .015	0.14 ± .11	0.42 ± .18	
ρ_{00}	0.0037 ± .015	0.07 ± .07	0.1 ± .06	
$Re\rho_{01}$	-0.003 ± .008	-0.03 ± .05	-.05 ± .05	
$Im\rho_{01}$	-0.001 ± .041	-0.01 ± .21	-	
$Re\rho_{02}$	0.002 ± .0075	0.0 ± .05	-0.02 ± .07	
$Im\rho_{02}$	0.002 ± .026	0.0 ± .15	-	
ρ_{22}	0.085 ± .015	0.03 ± .11	0.02 ± .07	
ρ_{2-2}	-0.078 ± .015	0.0 ± .11	0.0 ± .07	
$Re\rho_{12}$	-0.034 ± .011	0.035 ± .08	-0.04 ± .06	
$Im\rho_{12}$	-0.002 ± .038	-0.04 ± .27	-	
$Re\rho_{1-2}$	0.027 ± .011	-0.025 ± .08	0.03 ± .06	
$Im\rho_{1-2}$	0.000 ± .038	-0.03 ± .27	-	
$\rho_{11} + \rho_{1-1}$	0.818 ± .024	0.85 ± .08	0.85 ± .03	$\eta=+1$
$\rho_{22} - \rho_{2-2}$	0.163 ± .024	0.03 ± .07	0.02 ± .07	$\eta=+1$
$\rho_{11} - \rho_{1-1}$	0.009 ± .015	0.02 ± .07	0.01 ± .13	$\eta=-1$
$\rho_{22} + \rho_{2-2}$	0.008 ± .018	0.03 ± .08	0.02 ± .07	$\eta=-1$

TABLE 3b

Density Matrix for A_3

Density Matrix Element		Real Part	Imaginary Part
	ρ_{00}	0.749 ± .047	-
	ρ_{11}	0.076 ± .051	-
	ρ_{22}	0.049 ± .046	-
	ρ_{01}	0.137 ± .018	0.059 ± .066
	ρ_{02}	-0.031 ± .022	-0.024 ± .069
	ρ_{1-1}	-0.073 ± .051	-
	ρ_{2-2}	0.022 ± .046	-
	ρ_{12}	-0.018 ± .041	0.011 ± .115
	ρ_{1-2}	-0.009 ± .041	0.009 ± .115
$\eta=+1$	ρ_{00}	0.749 ± .047	-
	$\sqrt{2}\,\rho_{01}$	0.194 ± .025	0.033 ± .094
	$\sqrt{2}\,\rho_{02}$	-0.058 ± .031	-
	$\rho_{11} - \rho_{1-1}$	0.150 ± .039	-
	$\rho_{12} + \rho_{1-2}$	-0.027 ± .03	0.019 ± .088
	$\rho_{22} + \rho_{2-2}$	0.072 ± .038	-
$\eta=-1$	$\rho_{11} + \rho_{1-1}$	0.003 ± .033	
	$\rho_{12} - \rho_{1-2}$	0.009 ± .029	0.002 ± .074
	$\rho_{22} - \rho_{2-2}$	0.026 ± .037	-

FIGURE CAPTIONS

Fig. 1 Experimental layout of the Omega Spectrometer.

Fig. 2 (a) Acceptance for mass X^- in the reaction $\pi^- p \to X^- p$ at 12 GeV/c in the $|t|$ region 0.2 to 0.4 GeV^2.

(b) Acceptance as a function of $|t|$ for various values of the mass of X^-.

Fig. 3 An example of an event as displayed on-line showing the sparks as seen by the Plumbicon camera and the position of hit on the slow proton counter.

Fig. 4 Histograms of the missing mass to the proton in the reaction $\pi^- p \to X^- p$:

(a) missing mass squared distribution for the total sample;

(b) missing mass distribution for the total sample;

(c) missing mass squared distribution for the 2-prong sample;

(d) missing mass squared distribution for the 4-prong sample.

Fig. 5 Neutral missing mass distribution X^o for the reaction $\pi^- p \to \pi^- X^o p$.

Fig. 6 (a) Missing mass distribution X^o for the reaction $\pi^- p \to X^o \pi^+ \pi^- \pi^- p$.

FIGURE CAPTIONS (Cont'd)

(b,c) Effective mass distributions "η" $\pi^+\pi^-_s$ and "η" $\pi^+\pi^-_f$ from the reaction $\pi^- p \to X^o\pi^+\pi^-_f\pi^-_s p$ where the "η" mass is defined as $0.50 < M(X^o) < 0.58$ GeV and π^-_f, π^-_s refer to the faster and slower π^- in the laboratory system.

(d) Same as (b) and (c), but with $M(X^o)$ fixed at the η^o mass.

Fig. 7 (a) "η" $\pi^+\pi^-\pi^-$ effective mass distribution from the reaction $\pi^- p \to X^o\pi^+\pi^-\pi^- p$ with "η" defined as $0.5 < M(X^o) < 0.58$ GeV.

(b) $\eta'\pi^-_f$ effective mass distribution with $0.84 < M(X^o) < 0.98$ GeV.

Fig. 8 (a) $D^o\pi^-_f$ effective mass distribution with $1.24 < M(D^o) < 1.32$ GeV.

(b) $D^o p$ effective mass distribution with $1.24 < M(D^o) < 1.32$ GeV.

Fig. 9 "η" $\pi^{\mp}$ effective mass distribution ($0.5 < M(\eta^o) < 0.58$ GeV) from the "η"$\pi^+\pi^-_s$ mass combinations lying in the D^o mass region i.e. 1.24 to 1.32 GeV. The full line curve is the result of the fit described in the text.

Fig. 10 Missing mass distribution (X^o) from the reaction $\pi^- p \to \pi^- X^o p$. The full line curve is the result of fitting the η^o signal with a gaussian and a polynomial background.

Fig. 11 "η" π^- mass spectrum from the reaction $\pi^- p \to \pi^- X^o p$, where "η" is chosen to be the X^o mass region $0.5 < M(X^o) < 0.58$ GeV.

FIGURE CAPTIONS (Cont'd)

Fig. 12 (a) The $p\pi_s^+$ effective mass spectrum for all events with two or more positively charged secondaries one of which is the trigger proton.

(b) The missing mass spectrum X^{--} opposite the Δ^{++} (defined to be $1.15 < M(p\pi_s^+) < 1.27$ GeV).

(c) The missing mass spectrum X^{--} opposite the $p\pi_s^+$ of the reaction $\pi^- p \to X^{--}\pi_s^+ p$.

Fig. 13 The unfitted missing mass squared spectrum to the $p\pi^-$ for the 2-prong events fitting the reaction $\pi^- p \to \pi^o\pi^- p$ after applying the selection criteria described in the text.

Fig. 14 (a) $\pi^-\pi^o$ effective mass spectrum (unweighted and weighted for acceptance) from the reaction $\pi^- p \to \pi^o\pi^- p$.

(b) Unweighted $p\pi^-$ mass spectrum; the inset shows the low mass region with an expanded vertical scale.

(c) Unweighted $p\pi^o$ mass spectrum.

(d) Unweighted $\pi^-\pi^o$ mass spectrum from events with a $p\pi^-$ or $p\pi^o$ mass combination < 1.8 GeV removed.

Fig. 15 Regions of zero acceptance (non hatched regions) in the $(\cos\theta_J, \phi_J)$ Gottfried-Jackson decay plane for the $\pi^-\pi^o$ system from the reaction $\pi^- p \to \pi^o\pi^- p$ for the ρ^- and g^- mass regions.

FIGURE CAPTIONS (Cont'd)

Fig. 16 Variation of the statistical tensors t_m^ℓ of the $\pi^-\pi^o$ system for the reaction $\pi^- p \to \pi^o\pi^- p$ as a function of the $\pi^-\pi^o$ effective mass, where $t_m^\ell = \varepsilon_m^\ell \langle \text{Re } Y_m^\ell \rangle$; $\varepsilon_m^\ell = 1$, $m = 0$; $\varepsilon_m = 1/2$, $m \neq 0$.

Fig. 17 Differential cross section for the ρ^- and g^- mass regions, corrected for acceptance, as a function of the four-momentum transfer t to the proton for the reaction $\pi^- p \to \pi^o\pi^- p$.

Fig. 18 (a) Effective mass of the $\pi^+\pi^-\pi^-$ system for the reaction $\pi^- p \to \pi^+\pi^-\pi^- p$.

(b),(c) and (d) $\pi^+\pi^-\pi^-$ mass spectrum when a $\pi^-\pi^+$ combination has a mass lying within the ρ^o(0.64 - 0.84 GeV), f^o (1.16 - 1.38 GeV) and g^o (1.54 - 1.78 GeV) mass regions respectively.

(e) The total $\pi^+\pi^-$ effective mass spectrum from the reaction $\pi^- p \to \pi^+\pi^-\pi^- p$.

Fig. 19 (a) $p\pi^+$ effective mass spectrum for $\pi^- p \to \pi^+\pi^-\pi^- p$ events.

(b) $\pi^-\pi^-$ effective mass spectrum for events having a $p\pi^+$ mass combination in the Δ^{++} region i.e. $M(p\pi^+) < 1.4$ GeV.

Fig. 20 (a) $p\pi^+\pi^-$ effective mass spectrum, and

(b) $\Delta^{++}\pi^-$ effective mass spectrum for $\pi^- p \to \pi^+\pi^-\pi^- p$ events.

FIGURE CAPTIONS (Cont'd)

Fig. 21 Longitudinal Phase Space plot (LPS) for the reaction $\pi^- p \to \pi^+\pi^-\pi^- p$, X of the slower negative pion being plotted against X of the positive pion.

Fig. 22 (a) $\pi^+\pi^-\pi^-$ effective mass distribution, and

(b) $\pi^+\pi^-$ effective mass distribution for $\pi^- p \to \pi^+\pi^-\pi^- p$ events lying in sector 1 of the LPS plot.

Fig. 23 (a) $p\pi^-_s$ effective mass distribution, and

(b) $\pi^-_f\pi^+$ effective mass distribution for $\pi^- p \to \pi^+\pi^-\pi^- p$ events lying in sector 2 of the LPS plot.

Fig. 24 (a) $p\pi^+$ effective mass distribution, and

(b) $\pi^-\pi^-$ effective mass distribution for the $\pi^- p \to \pi^+\pi^-\pi^- p$ events lying in sector 3 of the LPS plot.

Fig. 25 $p\pi^+\pi^-_s$ effective mass distribution for $\pi^- p \to \pi^+\pi^-\pi^- p$ events lying in sector 4 of the LPS plot.

Fig. 26 Variation with mass of the $\pi^+\pi^-\pi^-$ system, of the various partial wave intensities for the reaction $\pi^- p \to \pi^+\pi^-\pi^- p$.

Fig. 27 Relative phase variation of the $J^P \ell = 2^+ D$ wave in the A_2 region of 3π mass.

FIGURE CAPTIONS (Cont'd)

Fig. 28 Relative phase variation of the $J^P\ell = 1^+S$ and $J^P\ell = 0^-S$ as a function of the 3π mass.

Fig. 29 Relative phase variation of the $J^P\ell = 2^-S$ wave as a function of the 3π mass in the A_3 region.

Fig. 30 (a) $p\pi^+$.

(b) $p\pi^o$, and

(b) $p\pi^-_s$ effective mass distributions for the reaction $\pi^- p \to \pi^+\pi^-\pi^-\pi^o p$.

Fig. 31 $\pi^+\pi^-$, $\pi^-\pi^o$ and $\pi^+\pi^o$ effective mass distributions for the reaction $\pi^- p \to \pi^+\pi^-\pi^-\pi^o p$.

Fig. 32 (a) and (b) $\pi^+\pi^-_f\pi^o$ and $\pi^+\pi^+_s\pi^o$ effective mass distributions for the reaction $\pi^- p \to \pi^+\pi^-\pi^-\pi^o p$ in 40 MeV and 10 MeV bins respectively.

Fig. 33 (a) $\pi^+\pi^-\pi^-$ effective mass distribution, and

(b) $\rho^o\pi^-$ effective mass distribution for the reaction $\pi^- p \to \pi^+\pi^-\pi^-\pi^o p$.

Fig. 34 $\pi^+\pi^-\pi^-\pi^o$ effective mass distribution for the reaction $\pi^- p \to \pi^+\pi^-\pi^-\pi^o p$.

FIGURE CAPTIONS (Cont'd)

Fig. 35 $\eta^o\pi^-$ effective mass distribution for the reaction $\pi^- p \to \pi^+\pi^-\pi^-\pi^o p$.

Fig. 36 $(\cos\theta_J,\ \phi_J)$ scatter plot and projections for $\eta^o\pi^-$ mass combinations lying in the A_2 mass region, where θ_J and ϕ_J are the decay angles of the $\eta^o\pi^-$ system in the Gottfried-Jackson frame.

Fig. 37 $\omega^o\pi^-$ effective mass distribution from the reaction $\pi^- p \to \pi^+\pi^-\pi^-\pi^o p$. The full line is the result of the fit described in the text.

Fig. 38 (a) (b), (c) and (d) the $\pi^+\pi^-\pi^-\pi^o$, $\rho^-\rho^o$, $A_2^o\pi^-$ and $A_2^-\pi^o$ effective mass distributions for the reaction $\pi^- p \to \pi^+\pi^-\pi^-\pi^o p$, where the full lines are the results of the fits described in the text.

Fig. 39 $\pi^+\pi^-$ effective mass distribution for the reaction $\pi^- p \to 2\pi^+ 3\pi^- p$.

Fig. 40 Sum of $\pi^+\pi^-\pi^-$ and $\pi^+\pi^+\pi^-$ mass distributions for the reaction $\pi^- p \to 2\pi^+ 3\pi^- p$.

Fig. 41 $2\pi^+ 2\pi^-$ effective mass distribution for the reaction $\pi^- p \to 2\pi^+ 3\pi^- p$.

FIGURE CAPTIONS (Cont'd)

Fig. 42 (a) and (b) the $\rho^o\pi^+$ and $\rho^o\pi^-$ effective mass distributions for the reaction $\pi^- p \to 2\pi^+ 3\pi^- p$.

Fig. 43 $2\pi^+ 3\pi^-$ effective mass spectrum for the reaction $\pi^- p \to 2\pi^+ 3\pi^- p$.

Fig. 44 $\pi^+\pi^-\pi^o$ effective mass spectrum for the reaction $\pi^- p \to 2\pi^+ 3\pi^- \pi^o p$.

Fig. 45 $\eta^o\pi^+\pi^-$ effective mass spectrum for the reaction $\pi^- p \to 2\pi^+ 3\pi^- \pi^o p$.

Fig. 46 $\omega^o\pi^+\pi^-$ effective mass spectrum for the reaction $\pi^- p \to 2\pi^+ 3\pi^- \pi^o p$.

Fig. 47 $2\pi^+ 3\pi^- \pi^o$ effective mass spectrum for the reaction $\pi^- p \to 2\pi^+ 3\pi^- \pi^o p$.

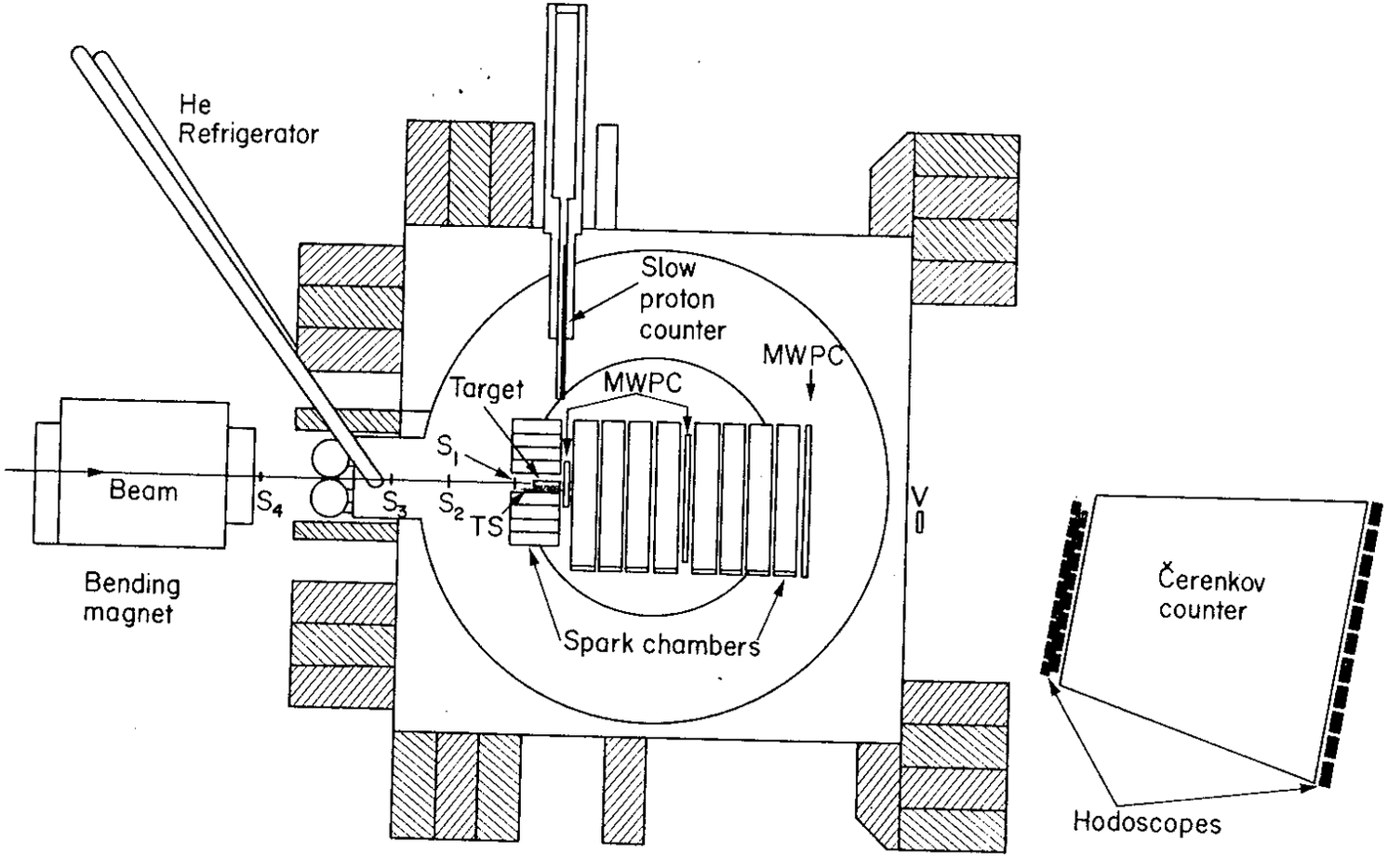
He
Refrigerator
Slow
proton
counter
MWPC
MWPC
Target
S_1
Beam
S_4
S_3
S_2
TS
V
Bending
magnet
Spark chambers
Čerenkov
counter
Hodoscopes

Fig. 1

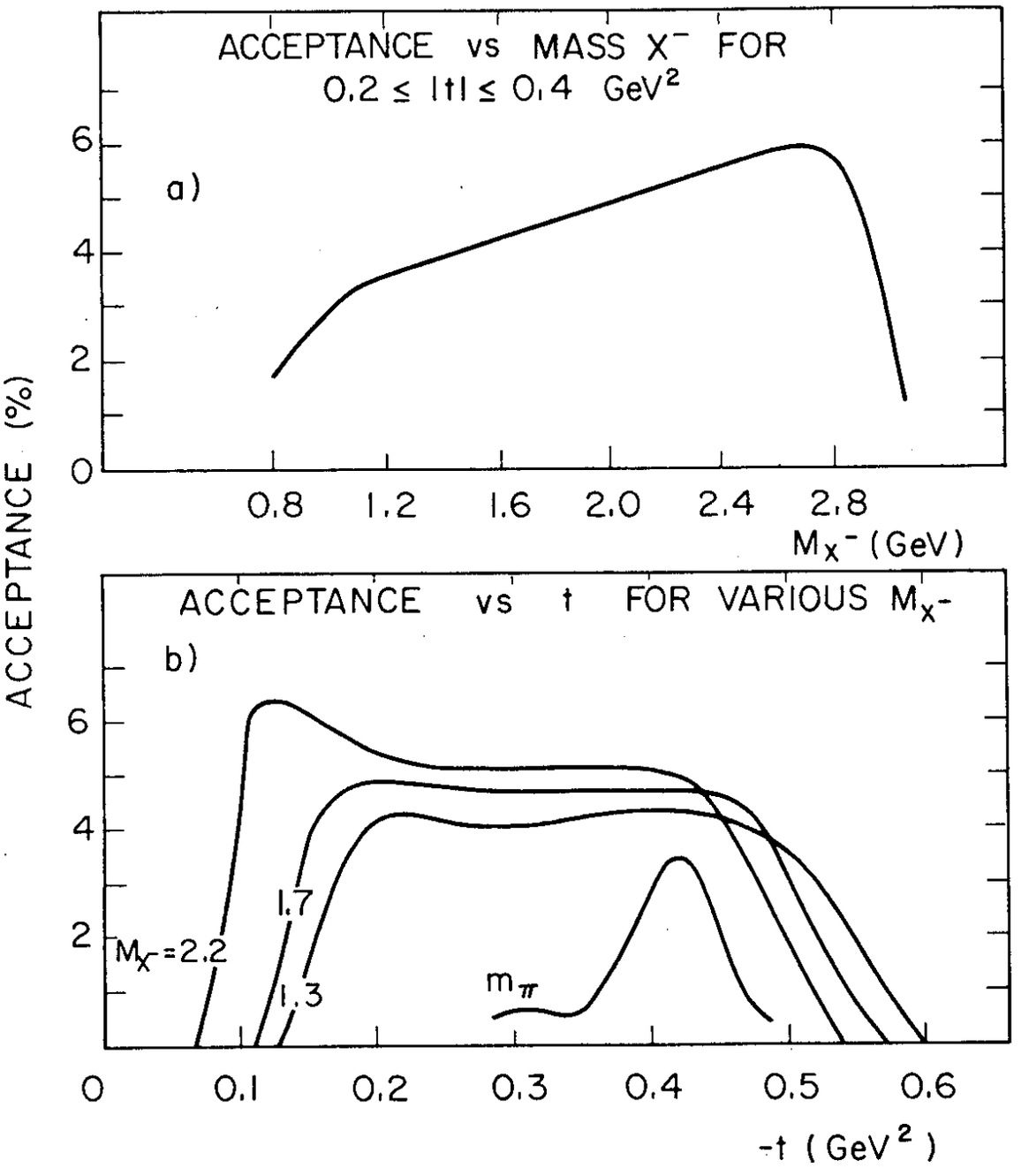
ACCEPTANCE vs MASS X⁻ FOR
0.2 ≤ |t| ≤ 0.4 GeV²
a)
6
4
2
0
0.8
1.2
1.6
2.0
2.4
2.8
Mx⁻ (GeV)
ACCEPTANCE (%)
ACCEPTANCE vs t FOR VARIOUS Mx⁻
b)
6
4
2
Mx⁻=2.2
1.7
1.3
mπ
0
0.1
0.2
0.3
0.4
0.5
0.6
-t (GeV²)

Fig. 2

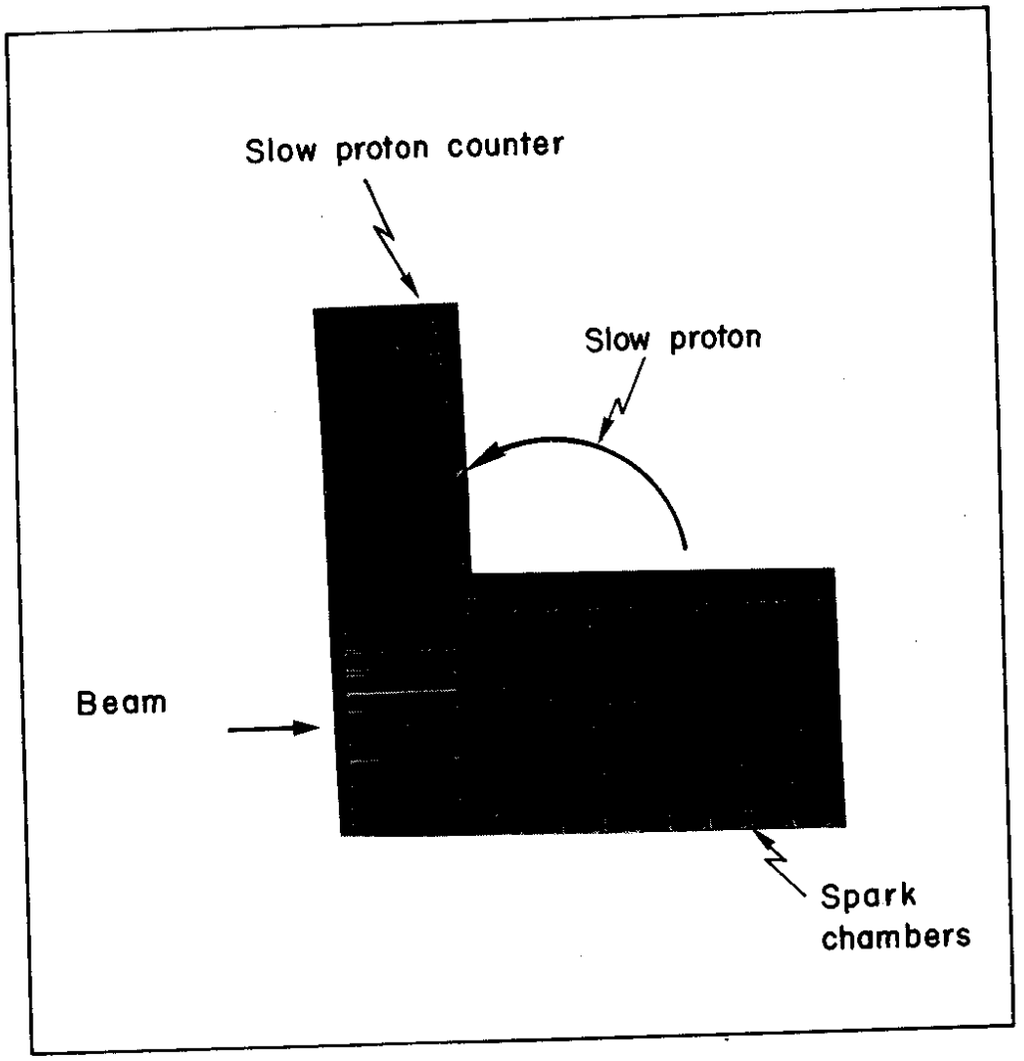

Fig. 3

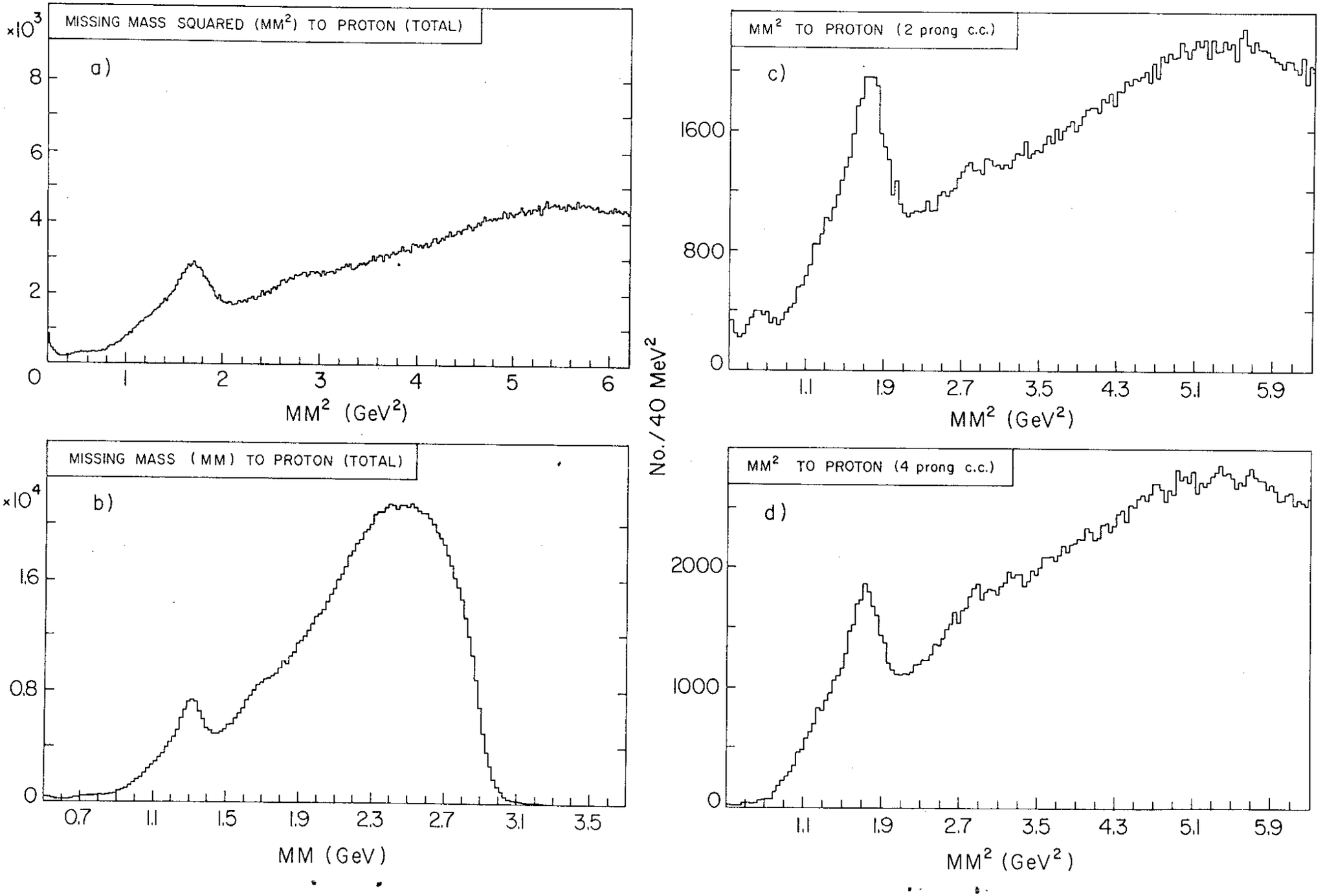
MISSING MASS SQUARED (MM²) TO PROTON (TOTAL)
a)
×10³
No/0.02 GeV²
MM² (GeV²)
MISSING MASS (MM) TO PROTON (TOTAL)
b)
×10⁴
No/20 MeV
MM (GeV)
MM² TO PROTON (2 prong c.c.)
c)
No./40 MeV²
MM² (GeV²)
MM² TO PROTON (4 prong c.c.)
d)
MM² (GeV²)

Fig. 4

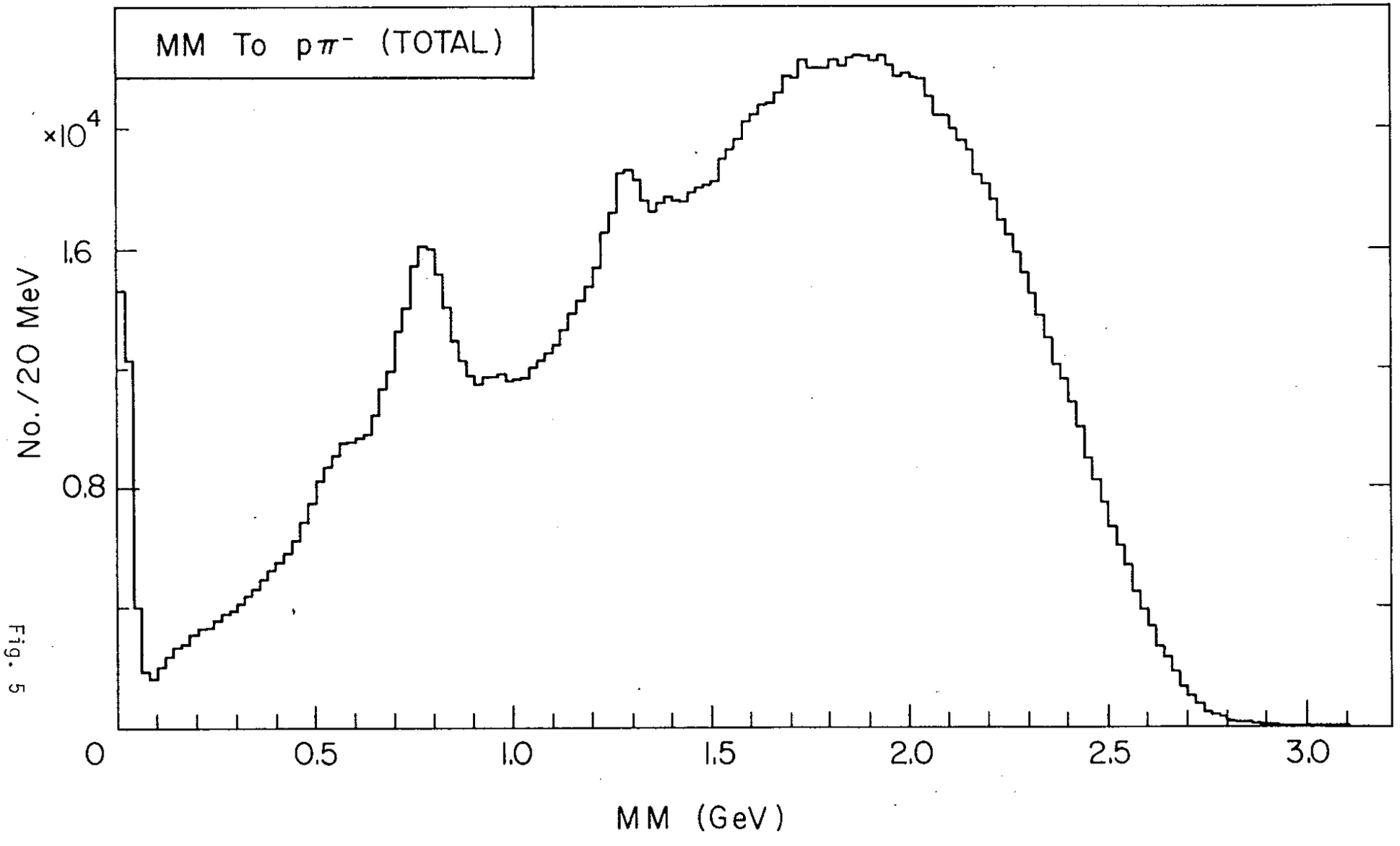

Fig. 5

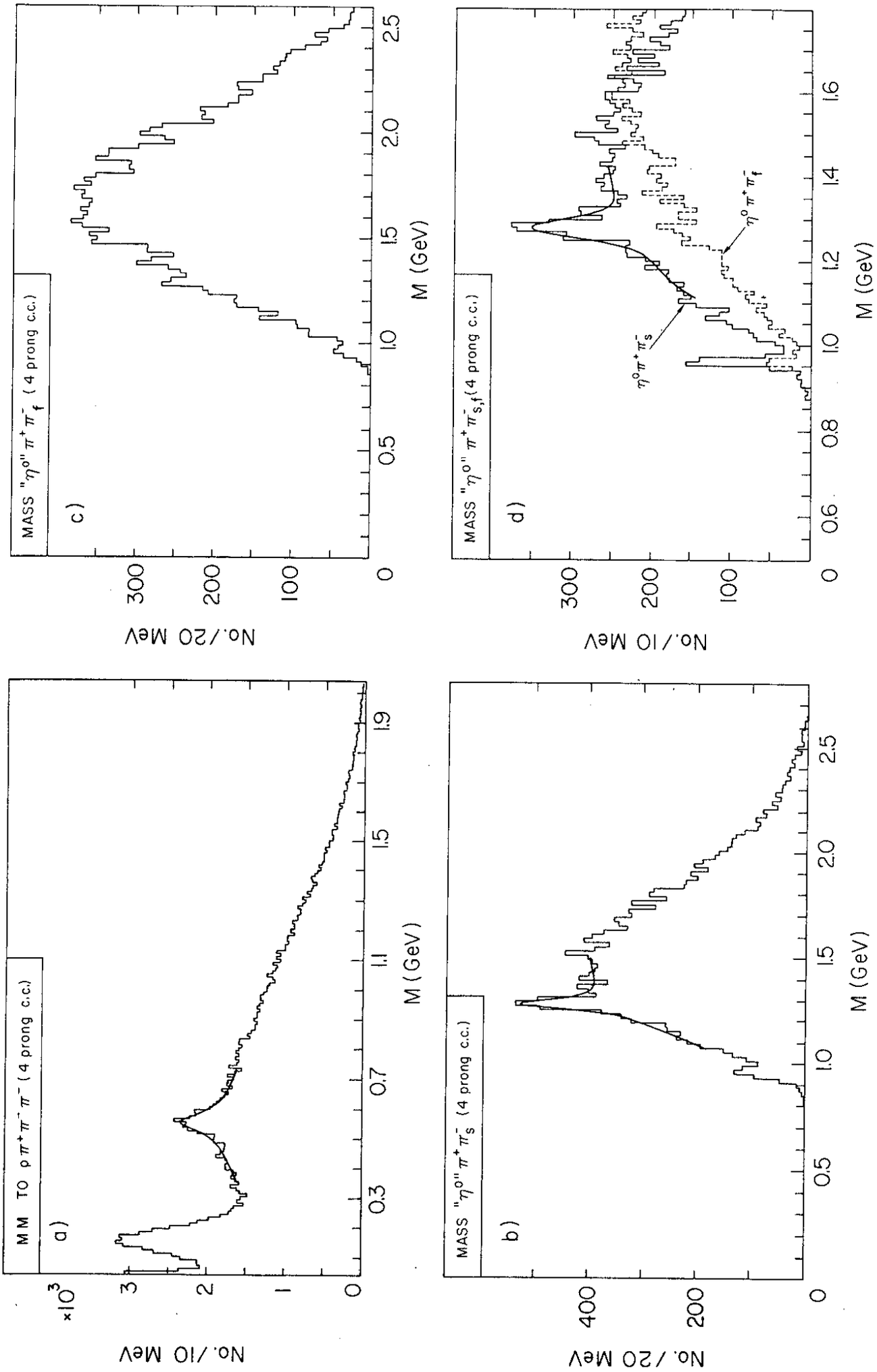
MASS "η^0" $\pi^+\pi^-_f$ (4 prong c.c.)
c)
No./20 MeV
M (GeV)
MASS "η^0" $\pi^+\pi^-_{s,f}$ (4 prong c.c.)
d)
$\eta^0\pi^+\pi^-_s$
$\eta^0\pi^+\pi^-_f$
No./10 MeV
M (GeV)
MM TO $p\pi^+\pi^-\pi^-$ (4 prong c.c.)
a)
$\times 10^3$
No./10 MeV
M (GeV)
MASS "η^0" $\pi^+\pi^-_s$ (4 prong c.c.)
b)
No./20 MeV
M (GeV)

Fig. 6

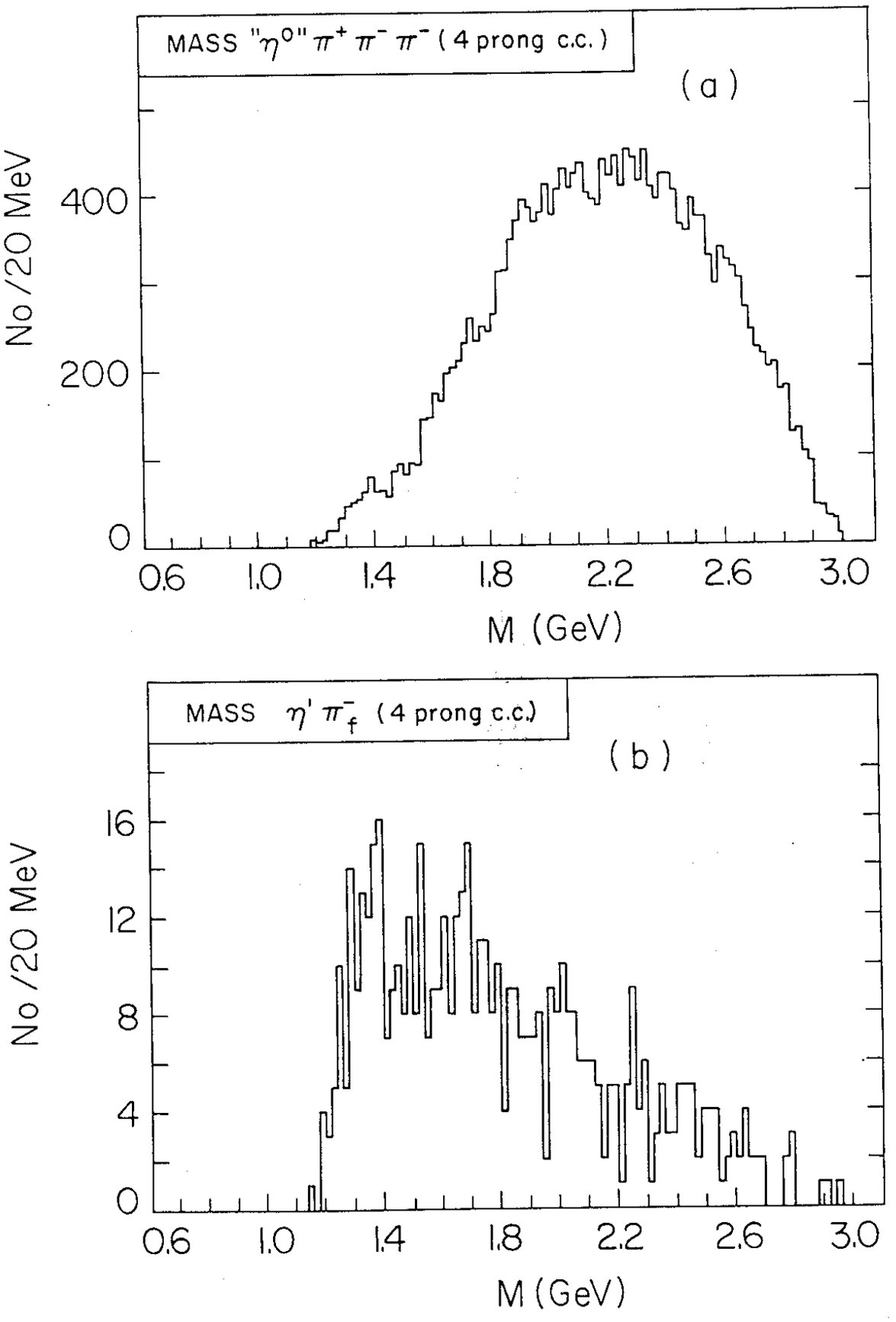
MASS "η⁰" π⁺ π⁻ π⁻ (4 prong c.c.)
(a)
No /20 MeV
400
200
0
0.6
1.0
1.4
1.8
2.2
2.6
3.0
M (GeV)
MASS η' π⁻f (4 prong c.c.)
(b)
No /20 MeV
16
12
8
4
0
0.6
1.0
1.4
1.8
2.2
2.6
3.0
M (GeV)

Fig. 7

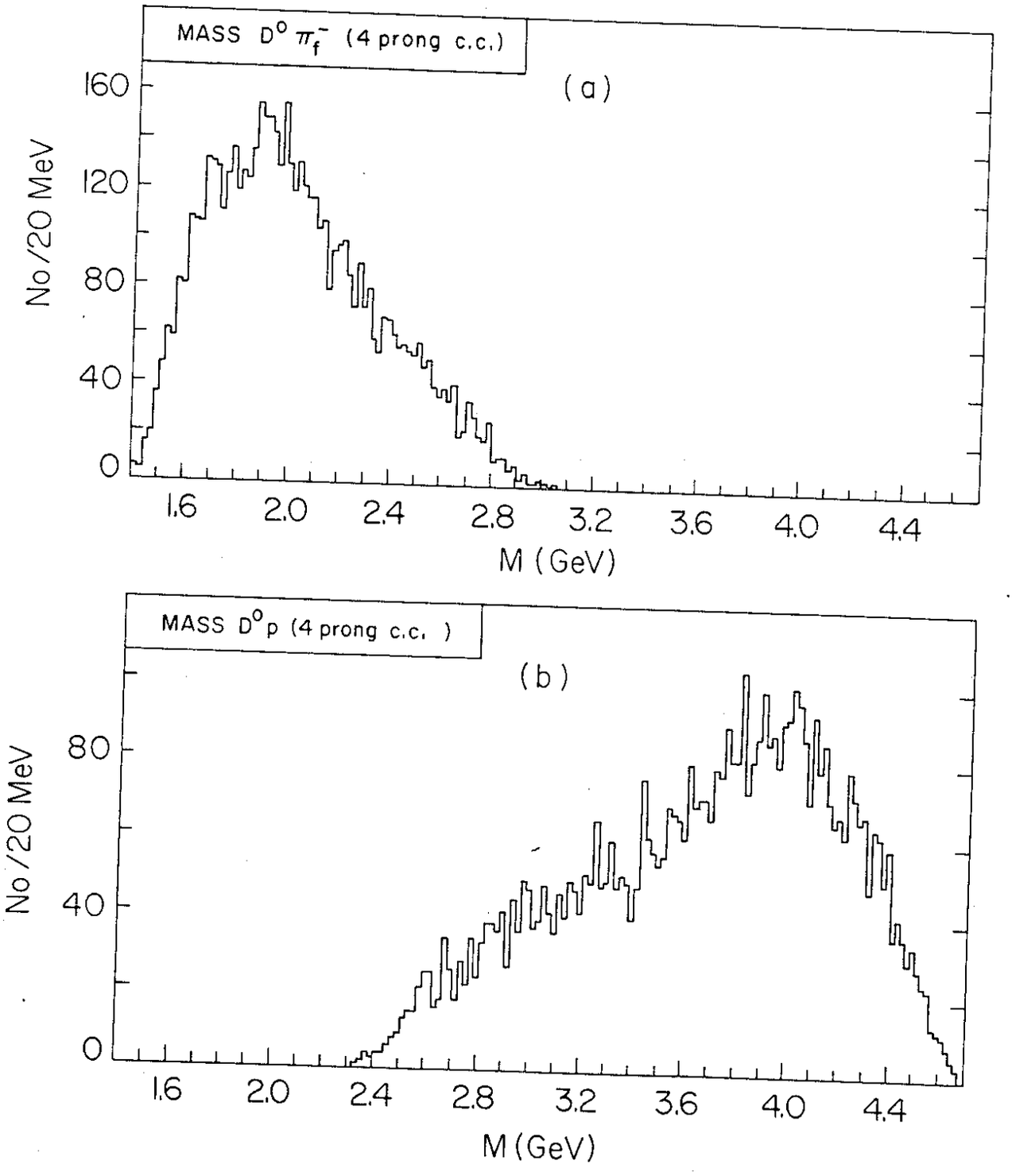
MASS $D^0 \pi_f^-$ (4 prong c.c.)
(a)
No /20 MeV
160
120
80
40
0
1.6
2.0
2.4
2.8
3.2
3.6
4.0
4.4
M (GeV)
MASS $D^0 p$ (4 prong c.c.)
(b)
No /20 MeV
80
40
0
1.6
2.0
2.4
2.8
3.2
3.6
4.0
4.4
M (GeV)

Fig. 8

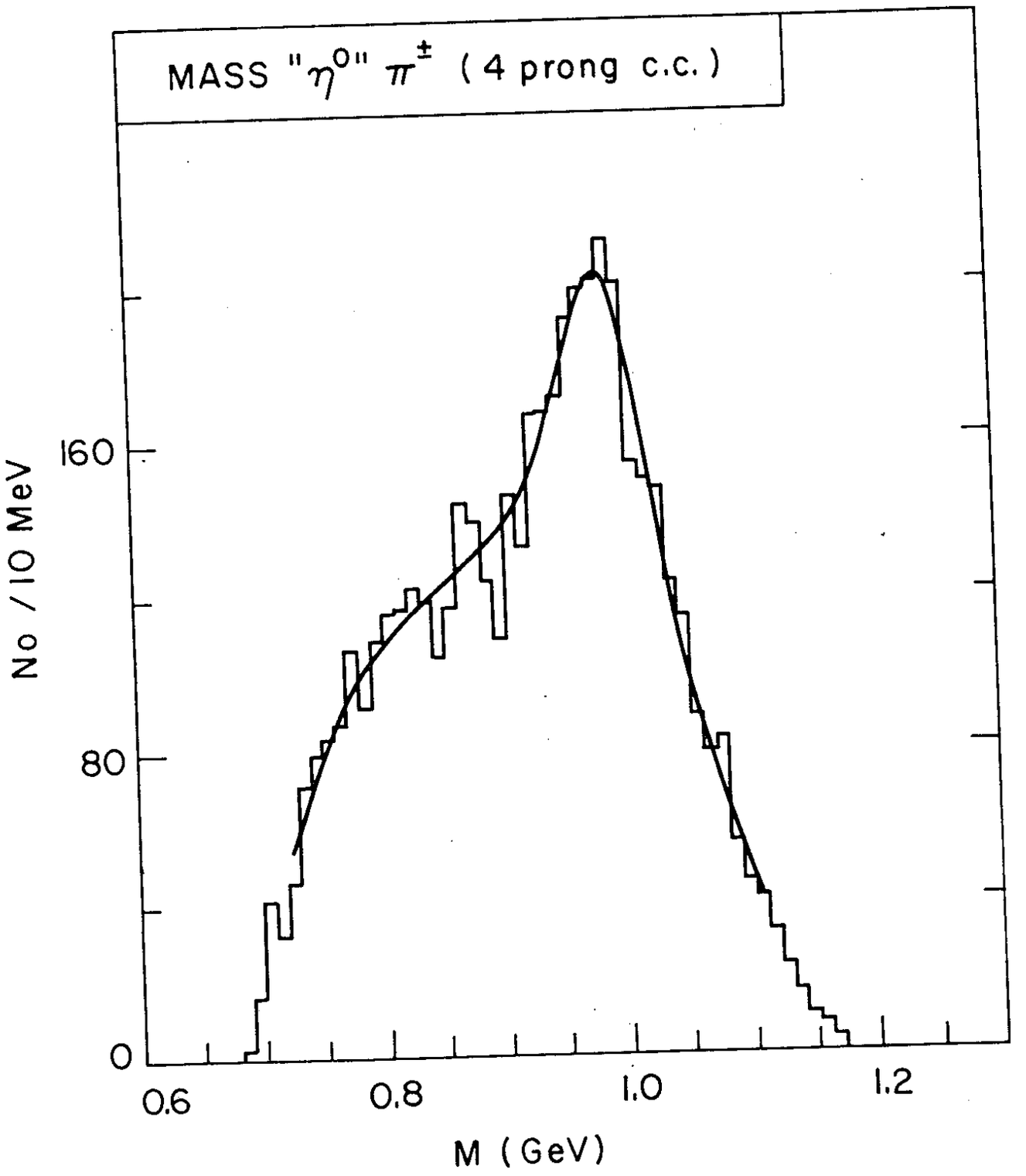

Fig. 9

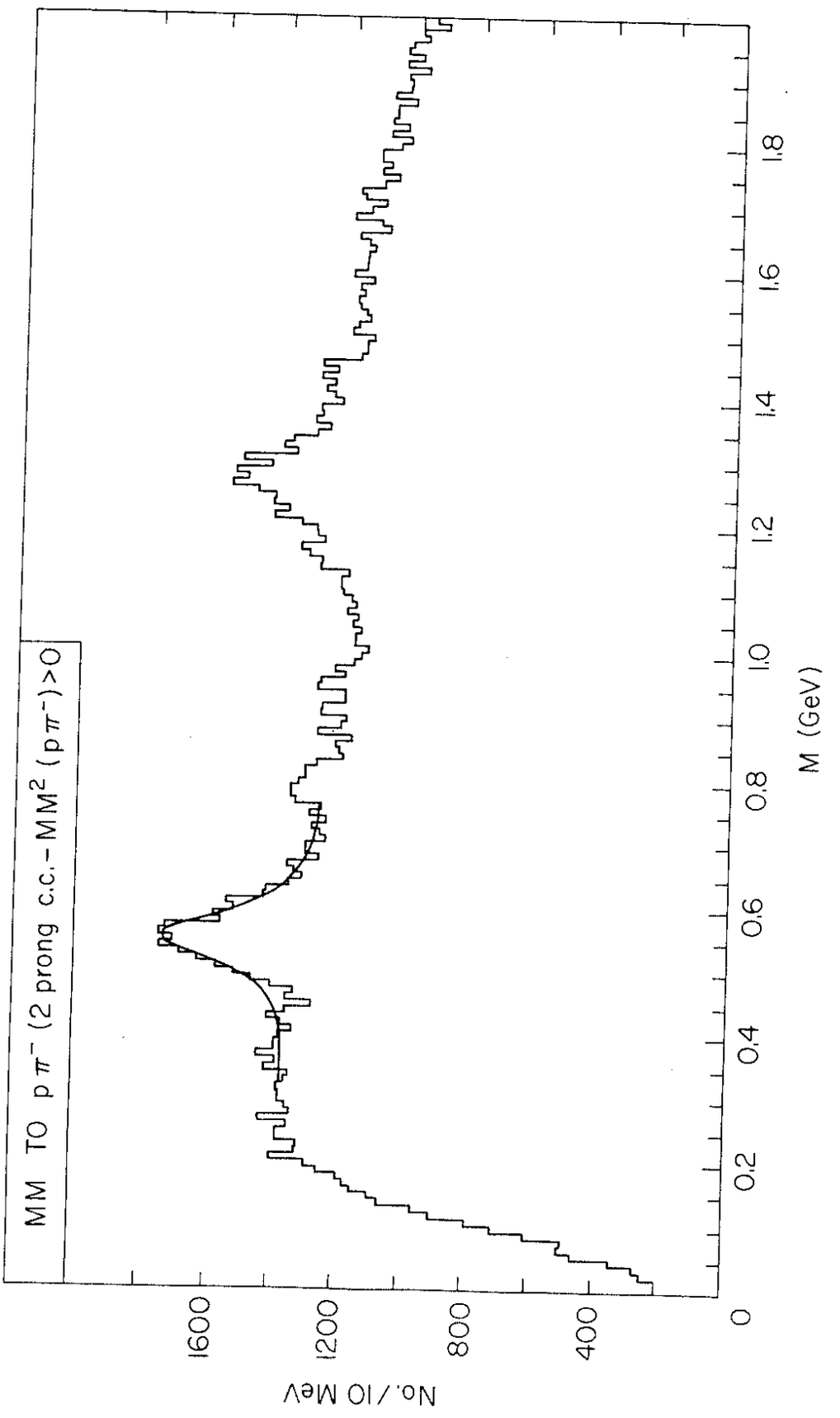
MM TO $p\pi^-$ (2 prong c.c. – MM^2 ($p\pi^-$) > 0
No./10 MeV
M (GeV)
0
400
800
1200
1600
0.2
0.4
0.6
0.8
1.0
1.2
1.4
1.6
1.8

Fig. 10

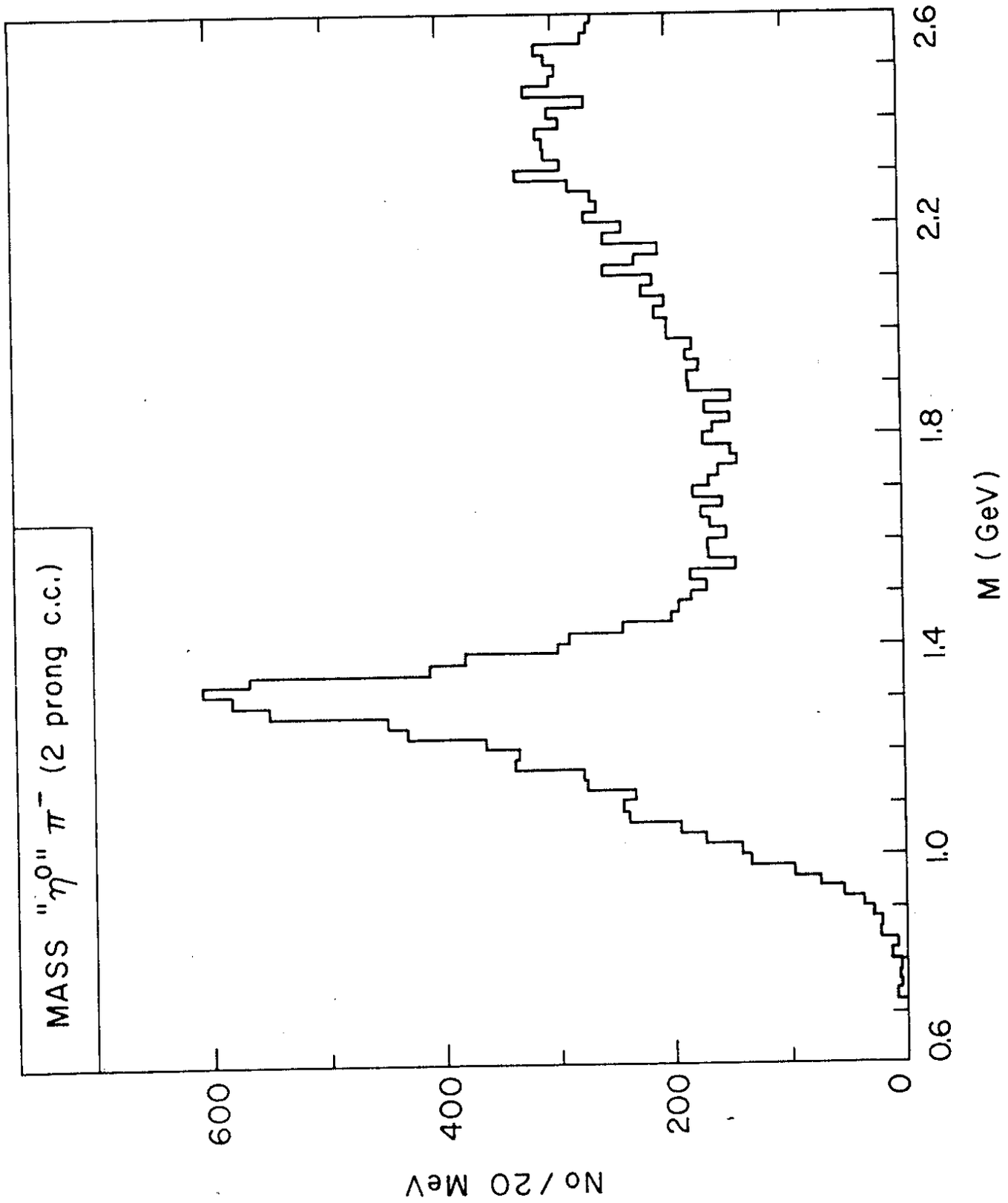
MASS "η^0" π^- (2 prong c.c.)
No / 20 MeV
0
200
400
600
0.6
1.0
1.4
1.8
2.2
2.6
M (GeV)

Fig. 11

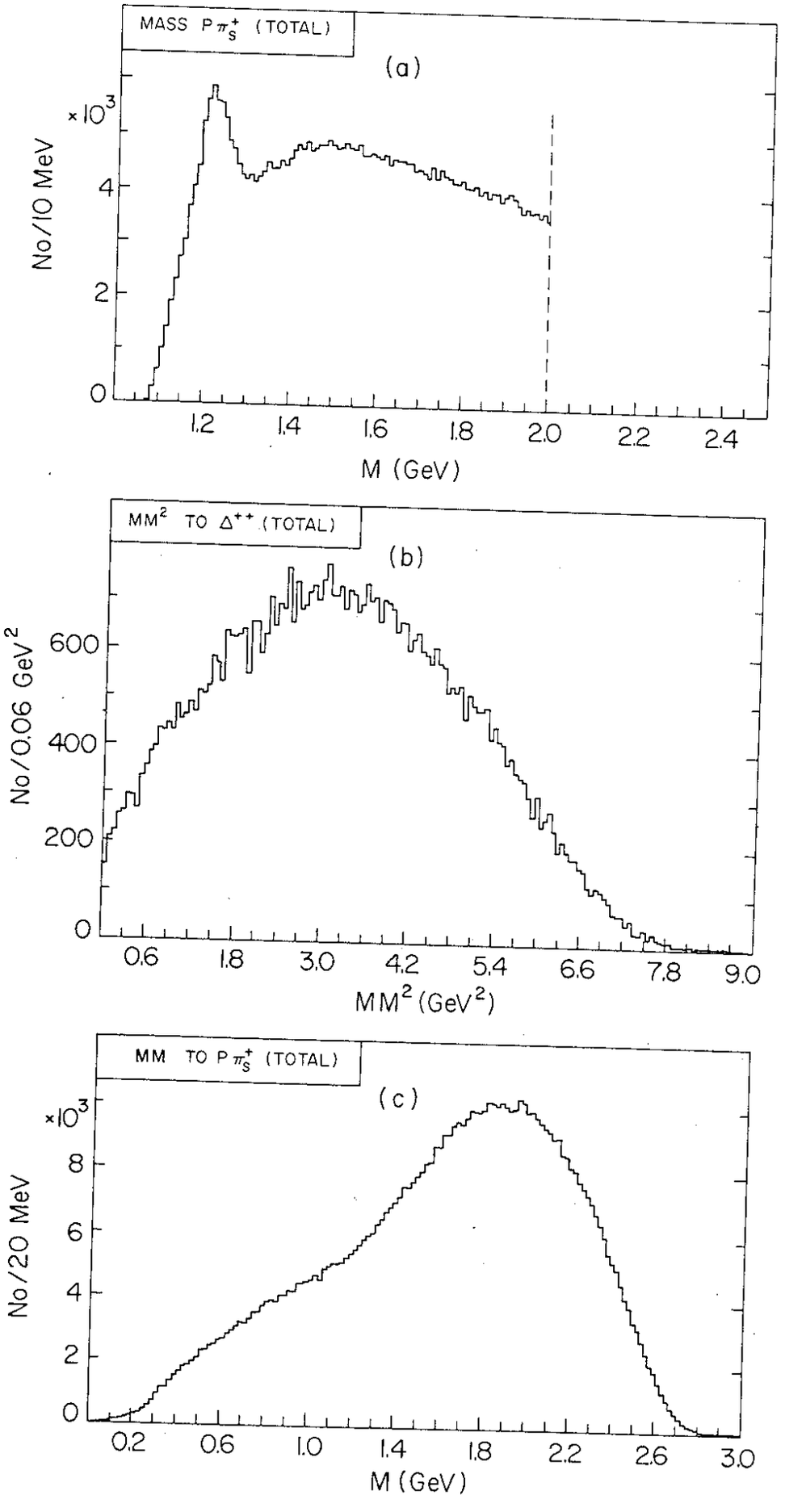
MASS $P\pi_S^+$ (TOTAL)
(a)
$\times 10^3$
No/10 MeV
0
2
4
1.2
1.4
1.6
1.8
2.0
2.2
2.4
M (GeV)
MM^2 TO Δ^{++} (TOTAL)
(b)
No/0.06 GeV^2
0
200
400
600
0.6
1.8
3.0
4.2
5.4
6.6
7.8
9.0
MM^2 (GeV^2)
MM TO $P\pi_S^+$ (TOTAL)
(c)
$\times 10^3$
No/20 MeV
0
2
4
6
8
0.2
0.6
1.0
1.4
1.8
2.2
2.6
3.0
M (GeV)

Fig. 12

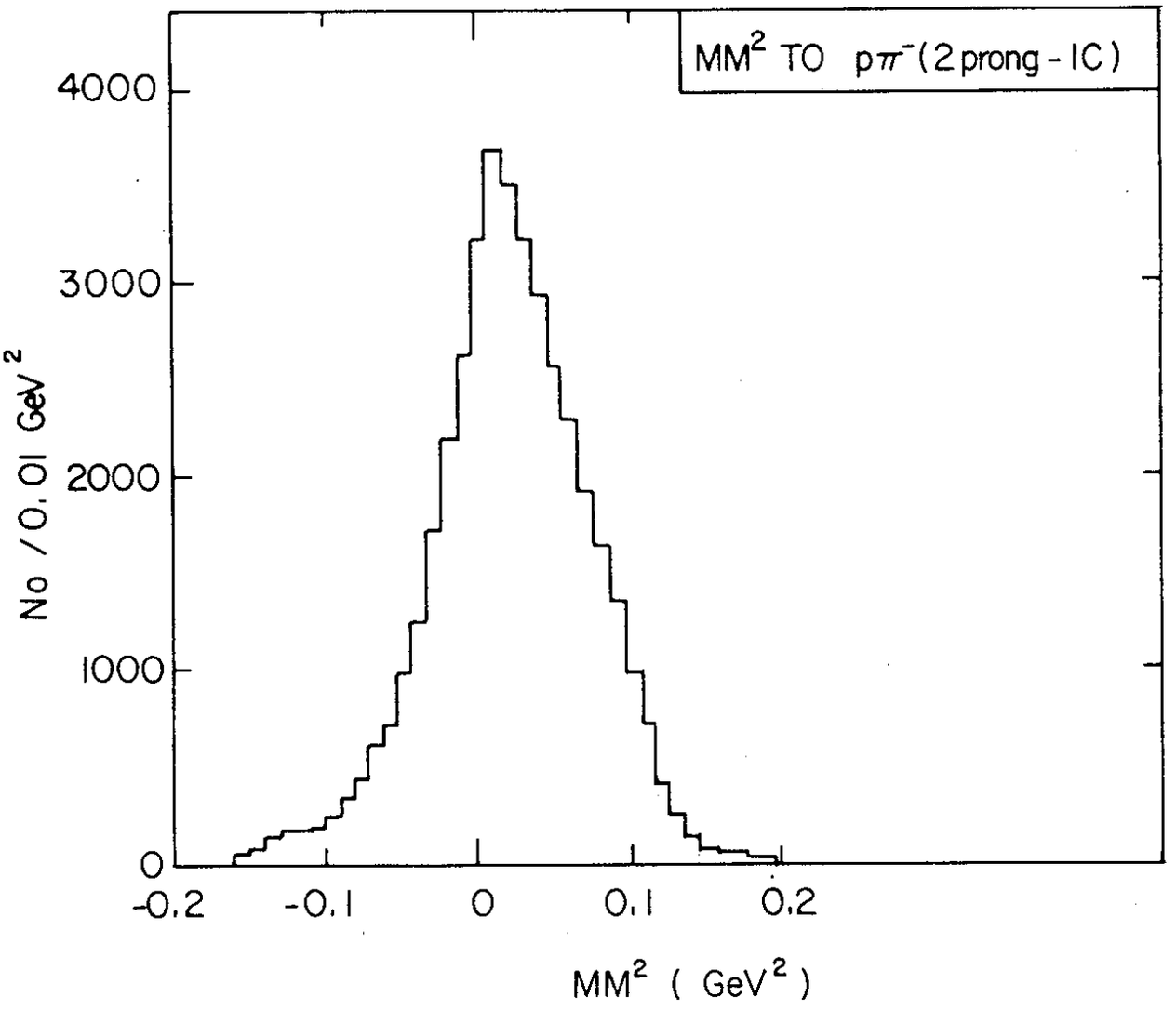
MM² TO pπ⁻(2prong-1C)
4000
3000
2000
1000
0
No /0.01 GeV²
-0.2
-0.1
0
0.1
0.2
MM² (GeV²)

Fig. 13

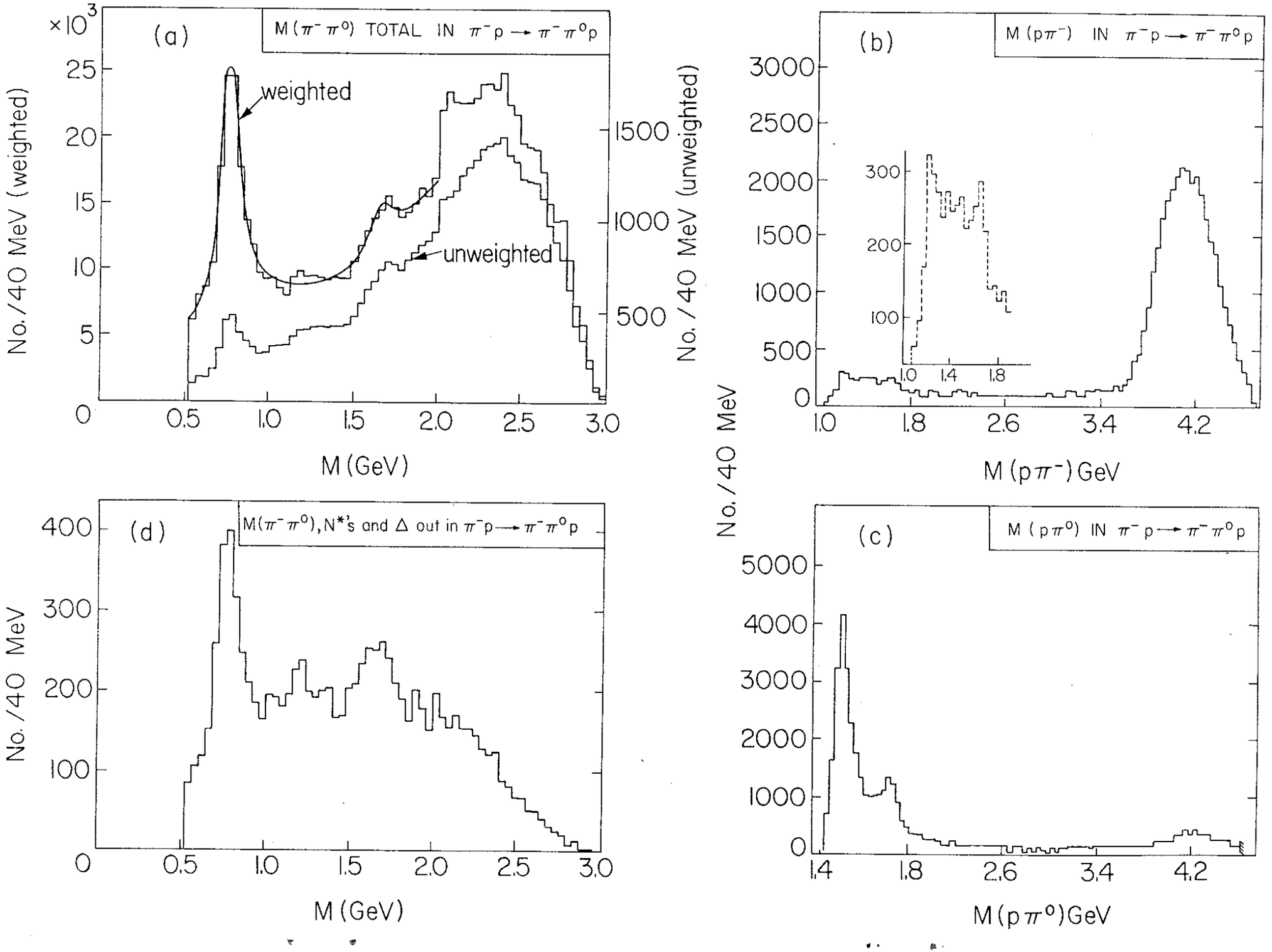
(a)
M(π⁻π⁰) TOTAL IN π⁻p → π⁻π⁰p
×10³
weighted
unweighted
No./40 MeV (weighted)
No./40 MeV (unweighted)
M (GeV)
(b)
M(pπ⁻) IN π⁻p → π⁻π⁰p
No./40 MeV
M(pπ⁻) GeV
(c)
M(pπ⁰) IN π⁻p → π⁻π⁰p
M(pπ⁰) GeV
(d)
M(π⁻π⁰), N*'s and Δ out in π⁻p → π⁻π⁰p
No./40 MeV
M (GeV)

Fig. 14

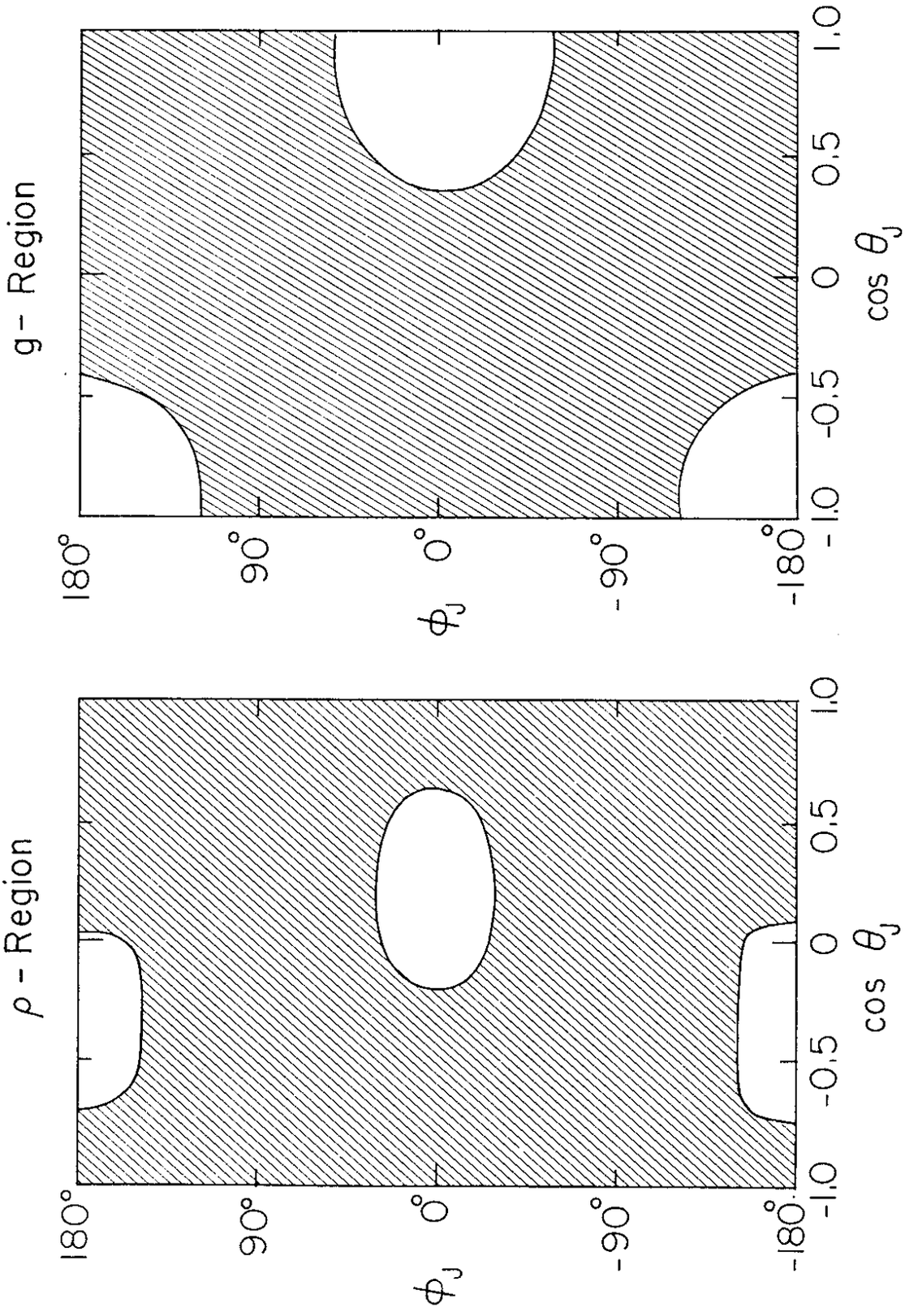

Fig. 15

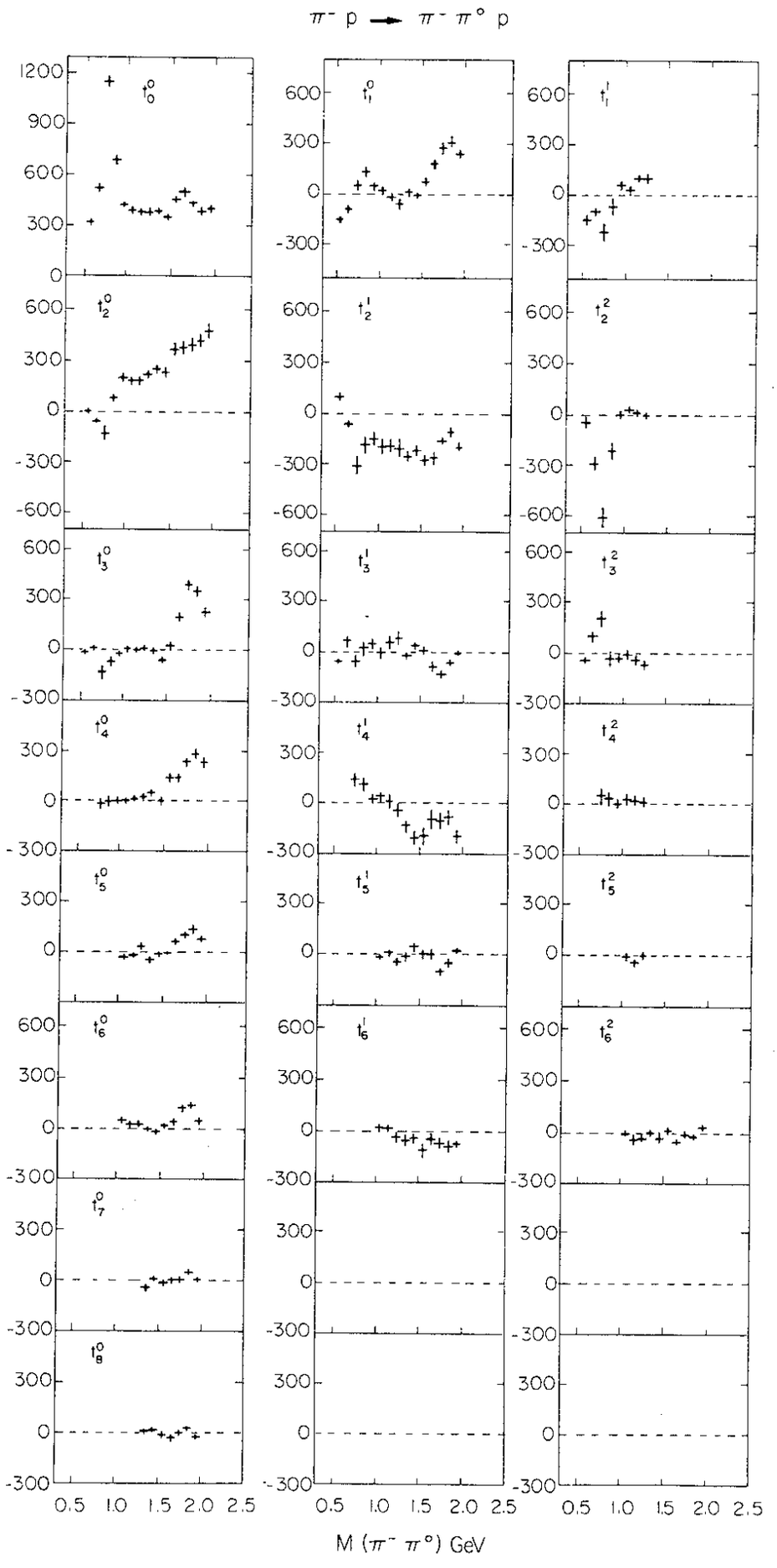
$\pi^- p \rightarrow \pi^- \pi^\circ p$
t_0^0
t_1^0
t_1^1
t_2^0
t_2^1
t_2^2
t_3^0
t_3^1
t_3^2
t_4^0
t_4^1
t_4^2
t_5^0
t_5^1
t_5^2
t_6^0
t_6^1
t_6^2
t_7^0
t_8^0
0.5 1.0 1.5 2.0 2.5
M ($\pi^- \pi^\circ$) GeV

Fig. 16

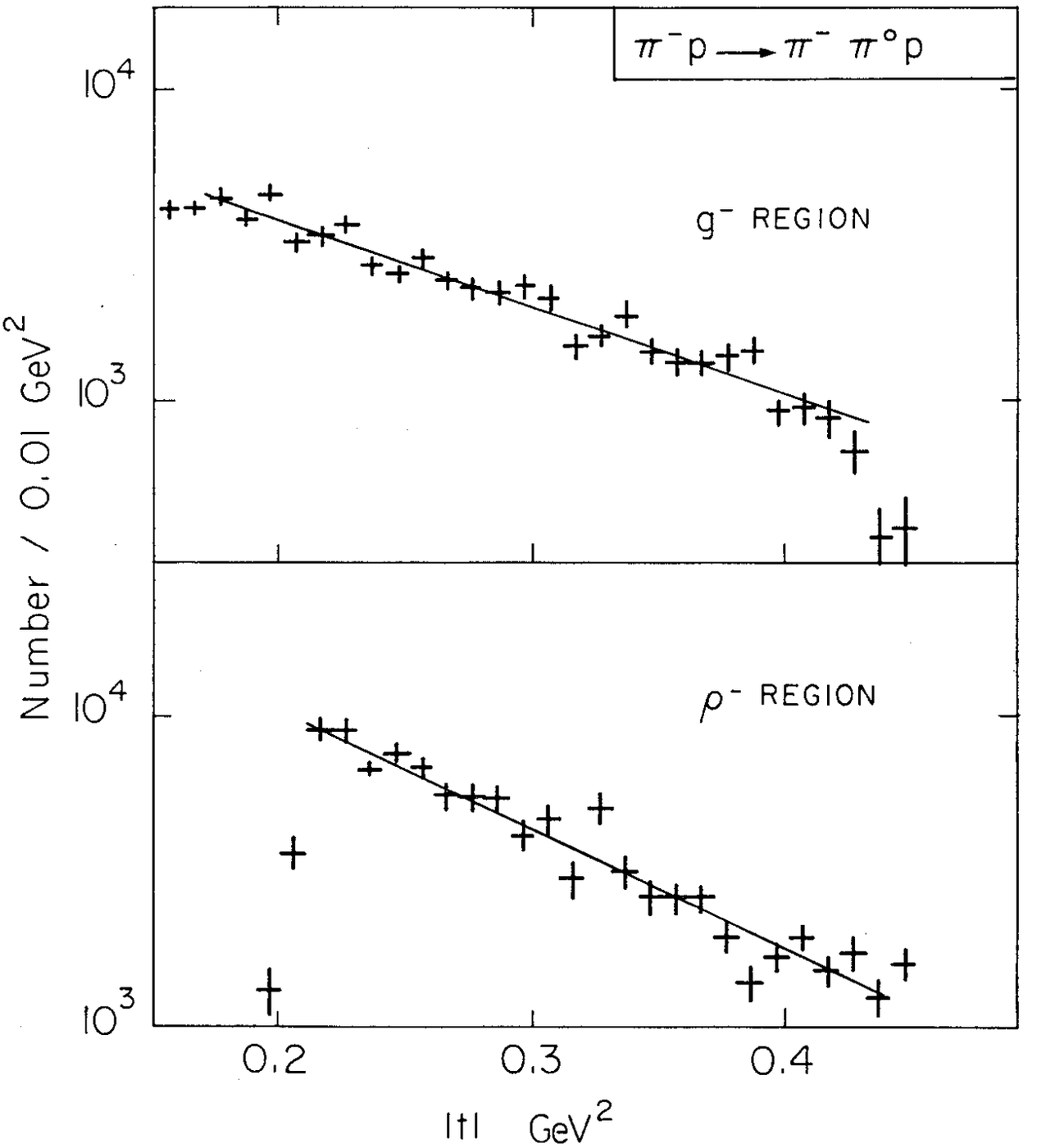
$\pi^- p \longrightarrow \pi^- \pi^\circ p$
g^- REGION
ρ^- REGION
Number / 0.01 GeV^2
10^4
10^3
10^4
10^3
0.2
0.3
0.4
$|t|$ GeV^2

Fig. 17

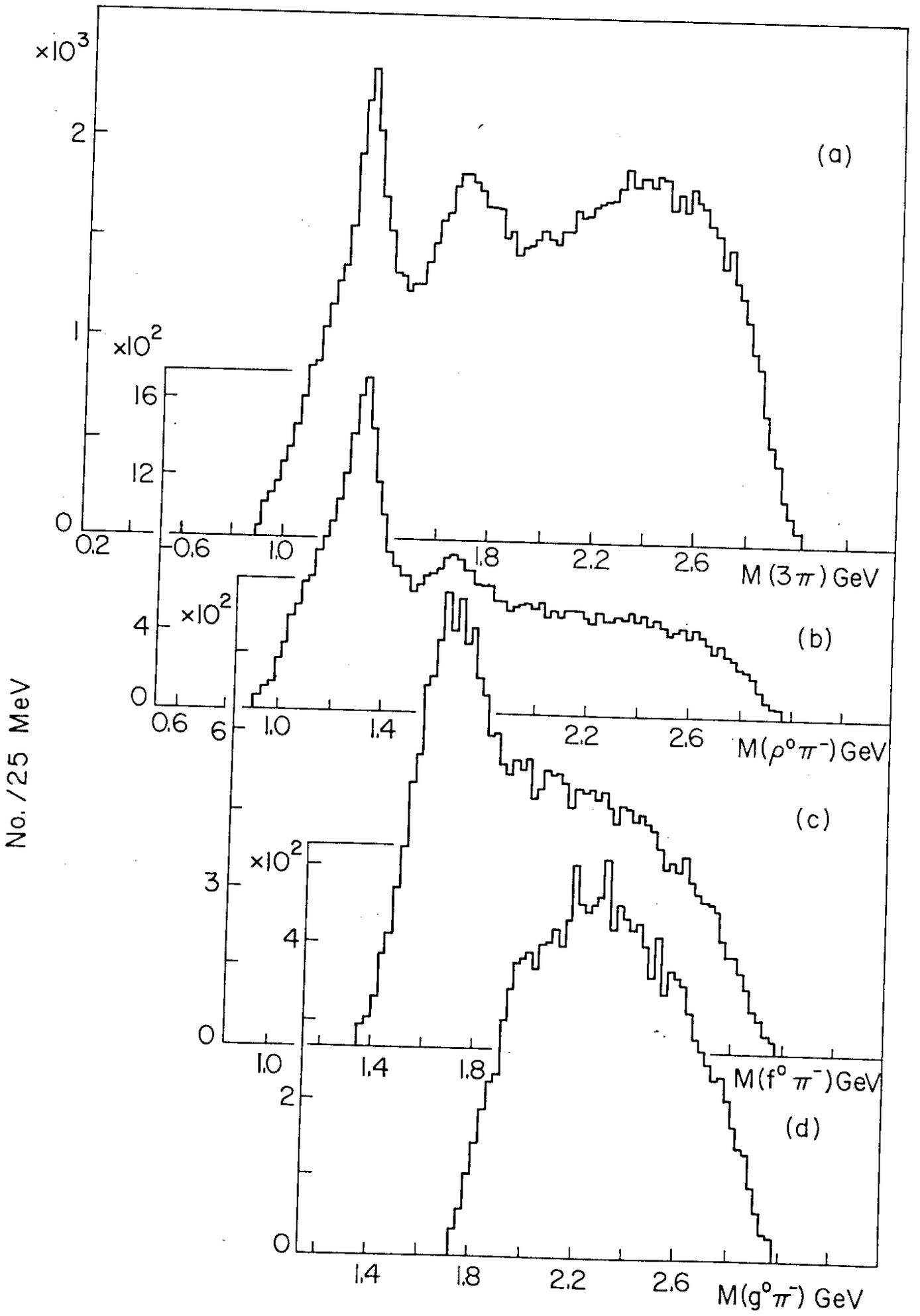
×10³
2
1
0
(a)
×10²
16
12
0.2
0.6
1.0
1.8
2.2
2.6
M (3π) GeV
×10²
4
0
0.6
1.0
1.4
2.2
2.6
M(ρ°π⁻) GeV
(b)
6
(c)
×10²
3
4
0
1.0
1.4
1.8
M(f°π⁻) GeV
2
(d)
0
1.4
1.8
2.2
2.6
M(g°π⁻) GeV
No./25 MeV

Fig. 18

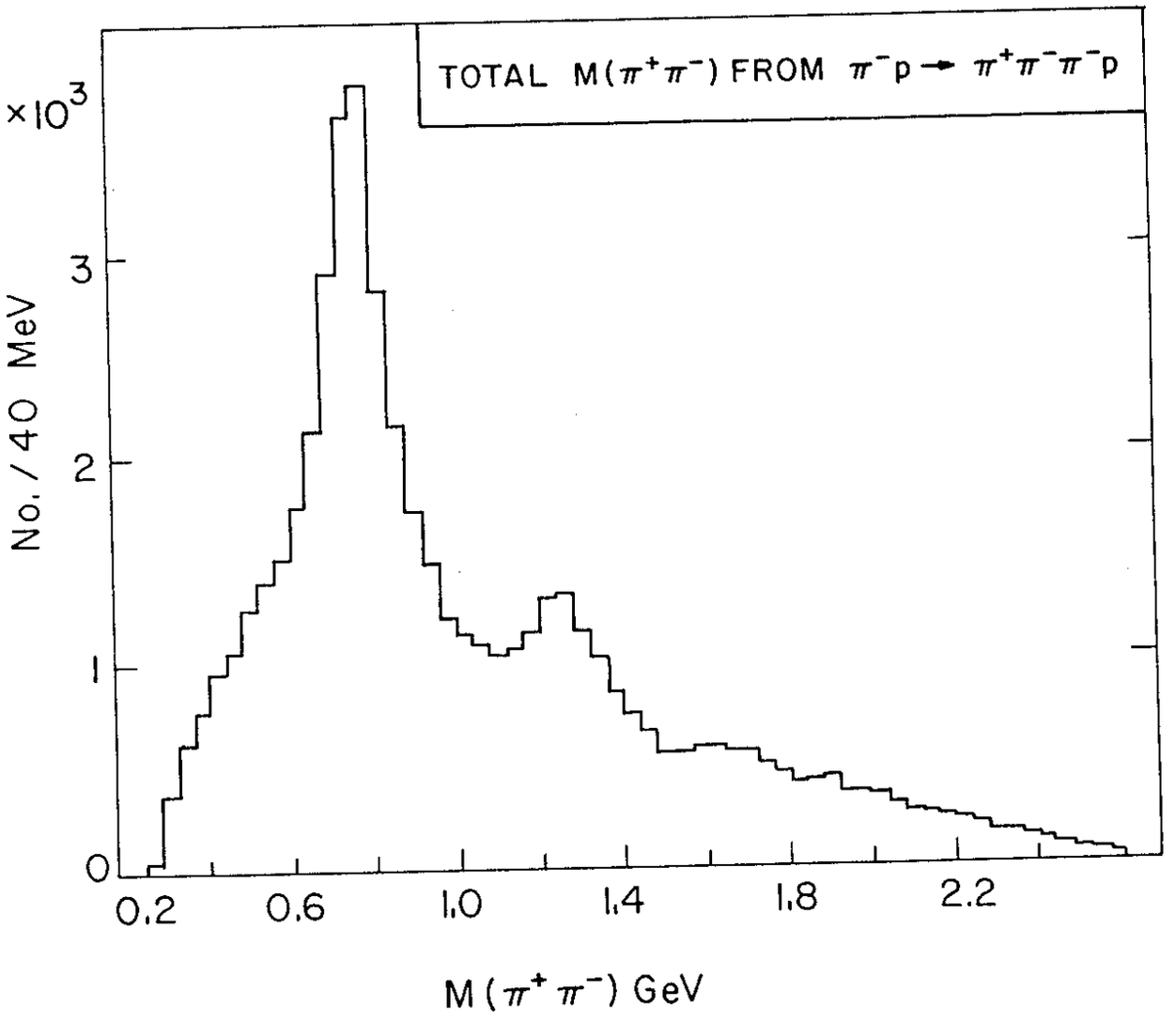
TOTAL M(π⁺π⁻) FROM π⁻p → π⁺π⁻π⁻p
×10³
No. / 40 MeV
3
2
1
0
0.2
0.6
1.0
1.4
1.8
2.2
M (π⁺ π⁻) GeV

Fig. 18e

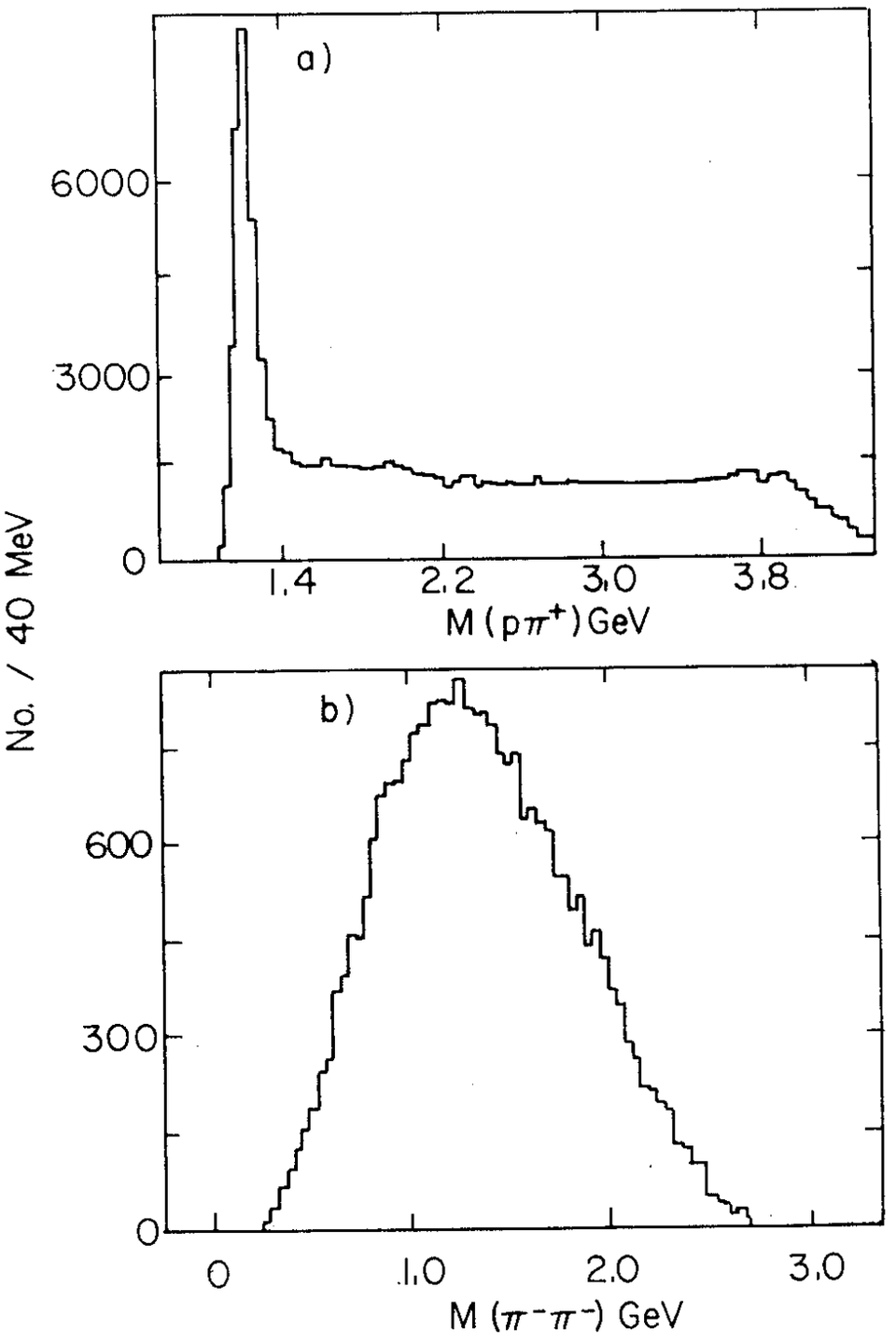
a)
6000
3000
0
1.4
2.2
3.0
3.8
M (pπ+) GeV
No. / 40 MeV
b)
600
300
0
0
1.0
2.0
3.0
M (π−π−) GeV

Fig. 19

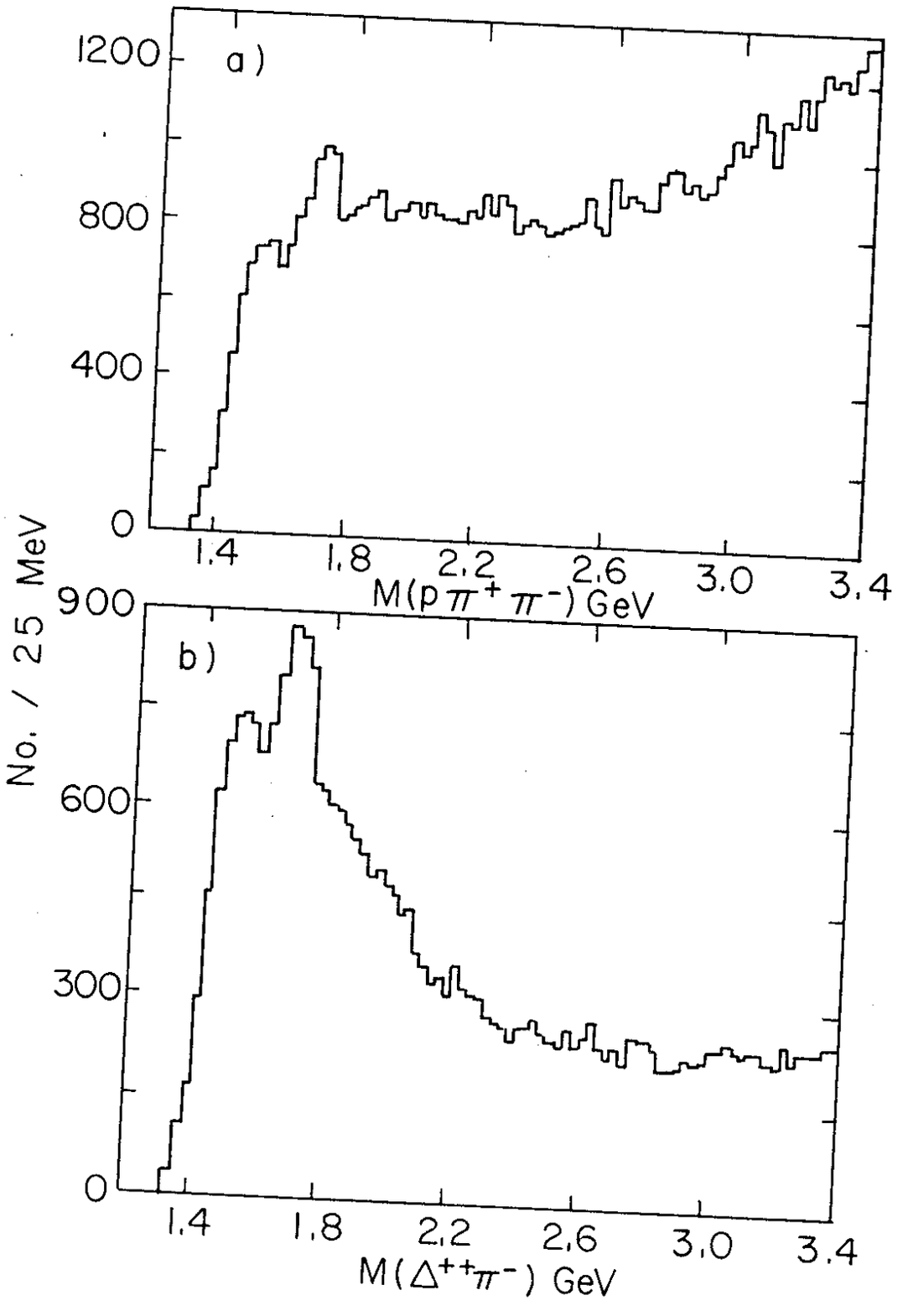
a)
1200
800
400
0
1.4
1.8
2.2
2.6
3.0
3.4
M(pπ+π−) GeV
b)
900
600
300
0
No. / 25 MeV
1.4
1.8
2.2
2.6
3.0
3.4
M(Δ++π−) GeV

Fig. 20

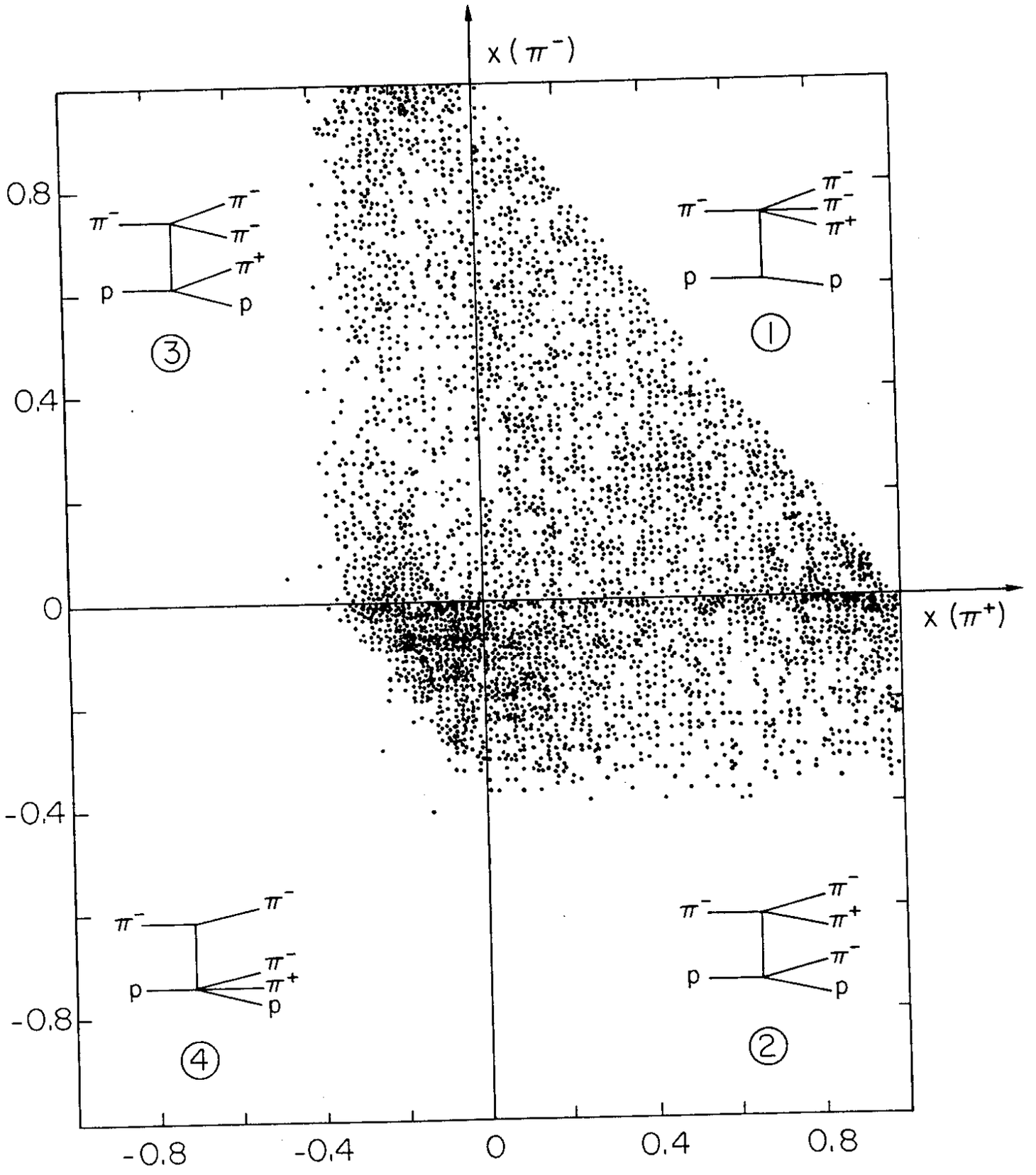

Fig. 21

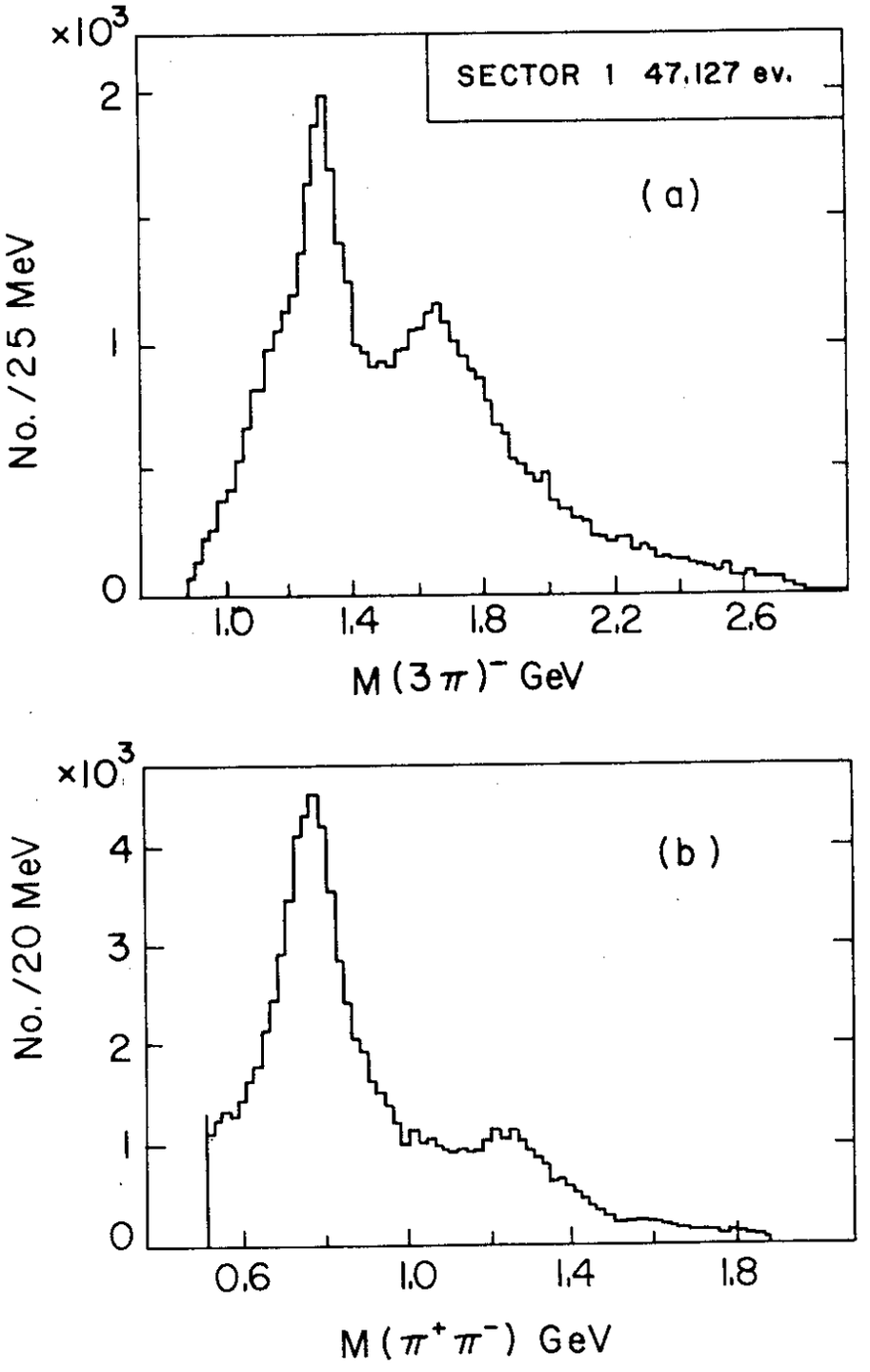
×10³
SECTOR 1 47,127 ev.
(a)
No./25 MeV
2
1
0
1.0
1.4
1.8
2.2
2.6
M(3π)⁻ GeV
×10³
(b)
No./20 MeV
4
3
2
1
0
0.6
1.0
1.4
1.8
M(π⁺π⁻) GeV

Fig. 22

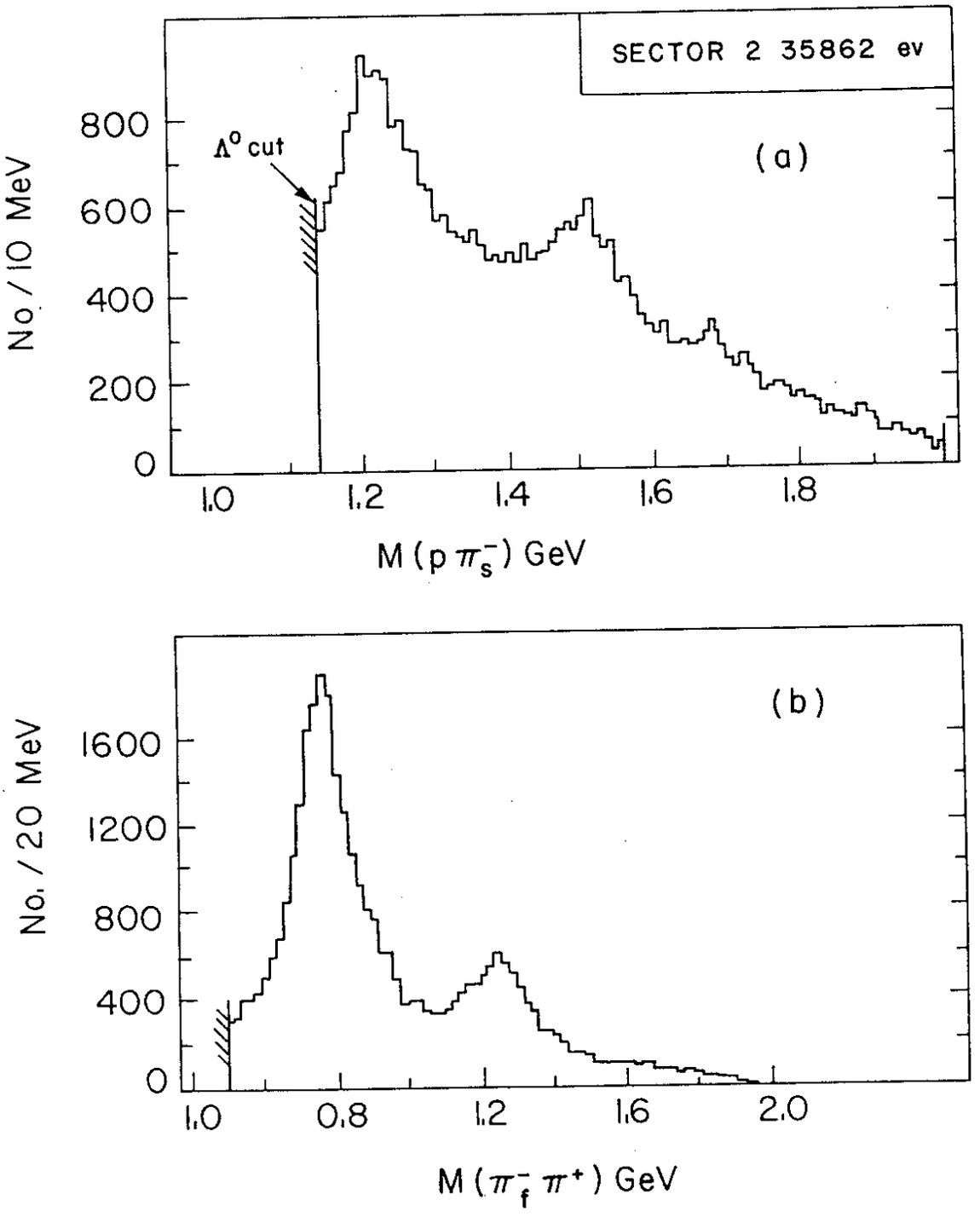
SECTOR 2 35862 ev
(a)
Λ^0 cut
No. / 10 MeV
800
600
400
200
0
1.0
1.2
1.4
1.6
1.8
M (p π_s^-) GeV
(b)
No. / 20 MeV
1600
1200
800
400
0
1.0
0.8
1.2
1.6
2.0
M (π_f^- π^+) GeV

Fig. 23

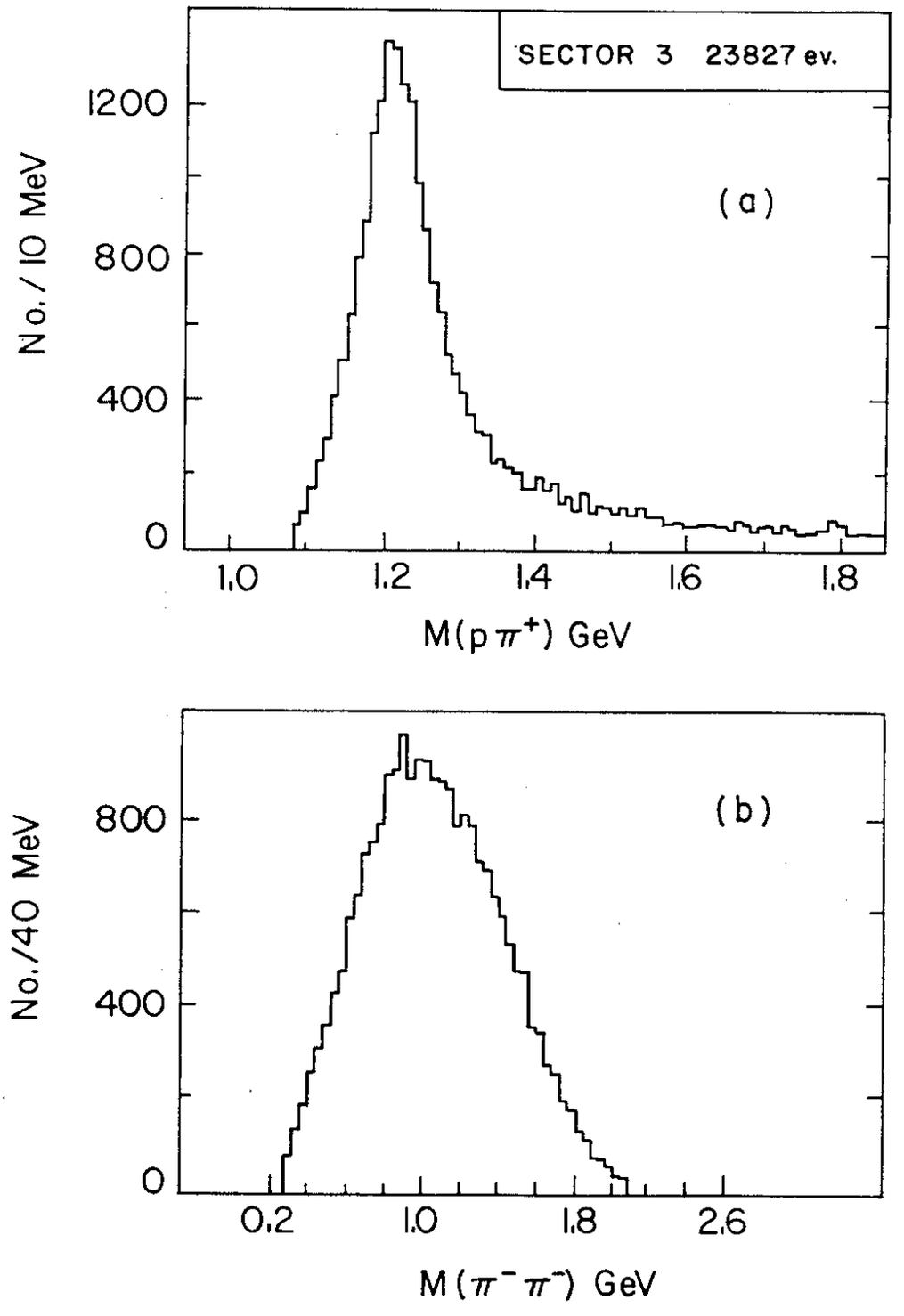
SECTOR 3 23827 ev.
(a)
No./ 10 MeV
1200
800
400
0
1.0
1.2
1.4
1.6
1.8
M(p π+) GeV
(b)
No./40 MeV
800
400
0
0.2
1.0
1.8
2.6
M(π⁻ π⁻) GeV

Fig. 24

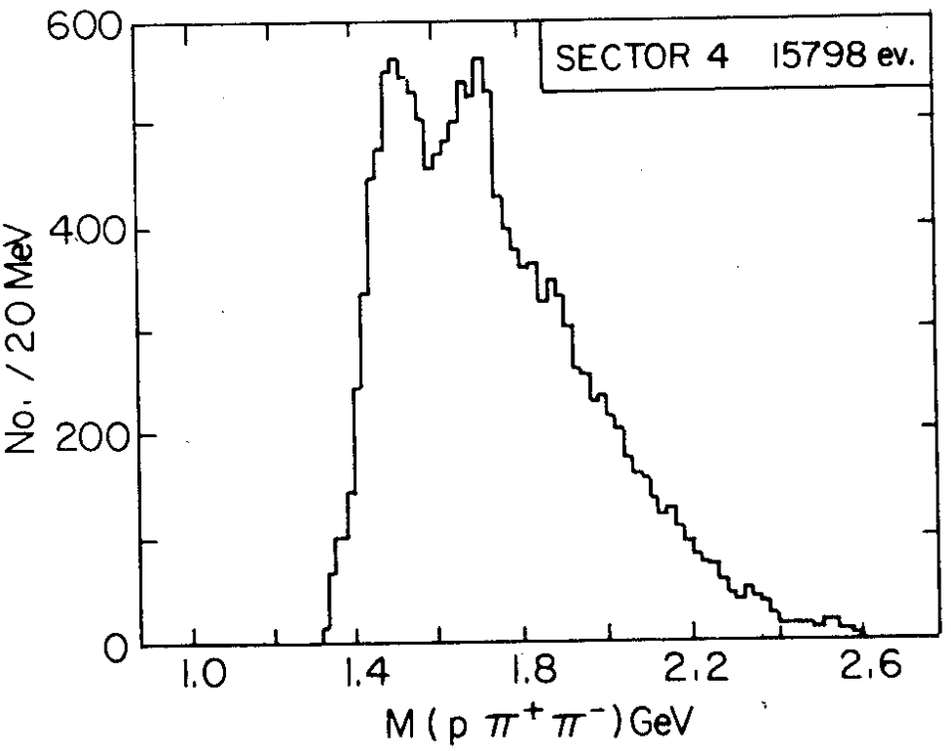

Fig. 25

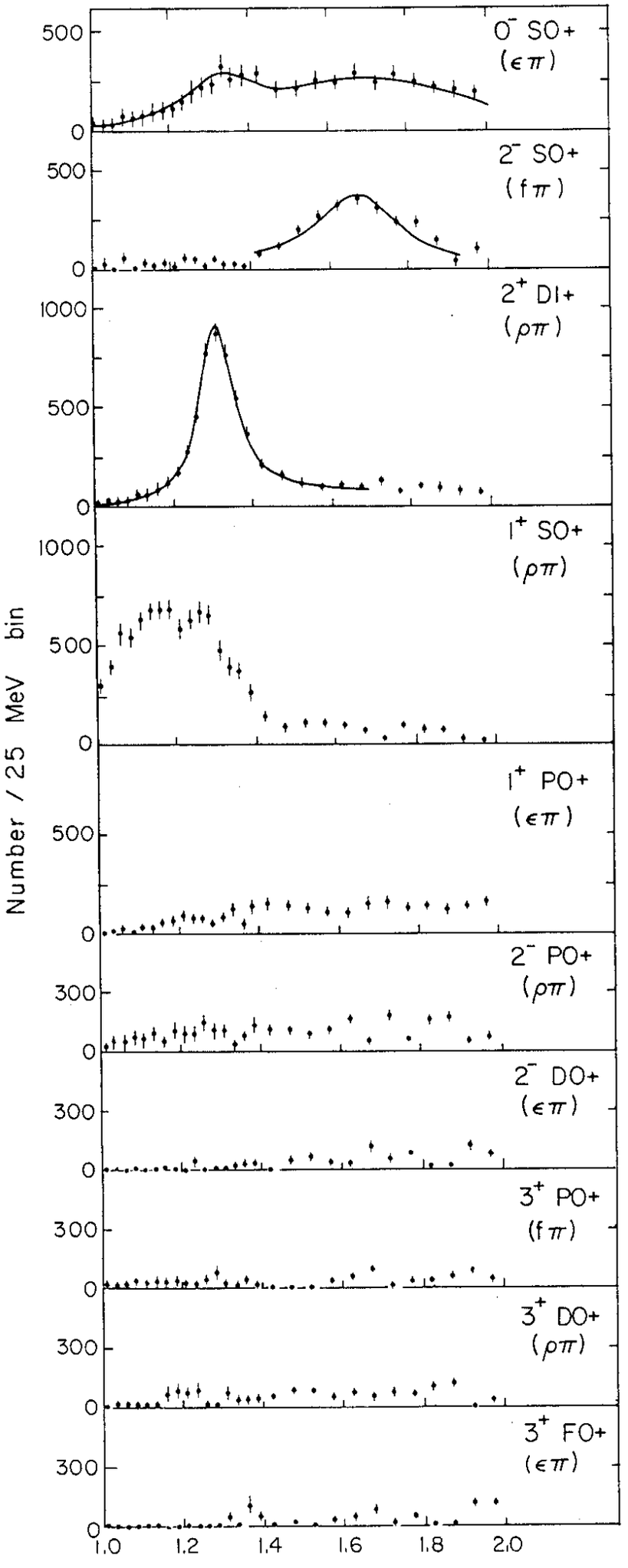
0⁻ SO+ (επ)
2⁻ SO+ (fπ)
2⁺ DI+ (ρπ)
1⁺ SO+ (ρπ)
1⁺ PO+ (επ)
2⁻ PO+ (ρπ)
2⁻ DO+ (επ)
3⁺ PO+ (fπ)
3⁺ DO+ (ρπ)
3⁺ FO+ (επ)
Number / 25 MeV bin
M (3π) GeV
1.0
1.2
1.4
1.6
1.8
2.0

Fig. 26

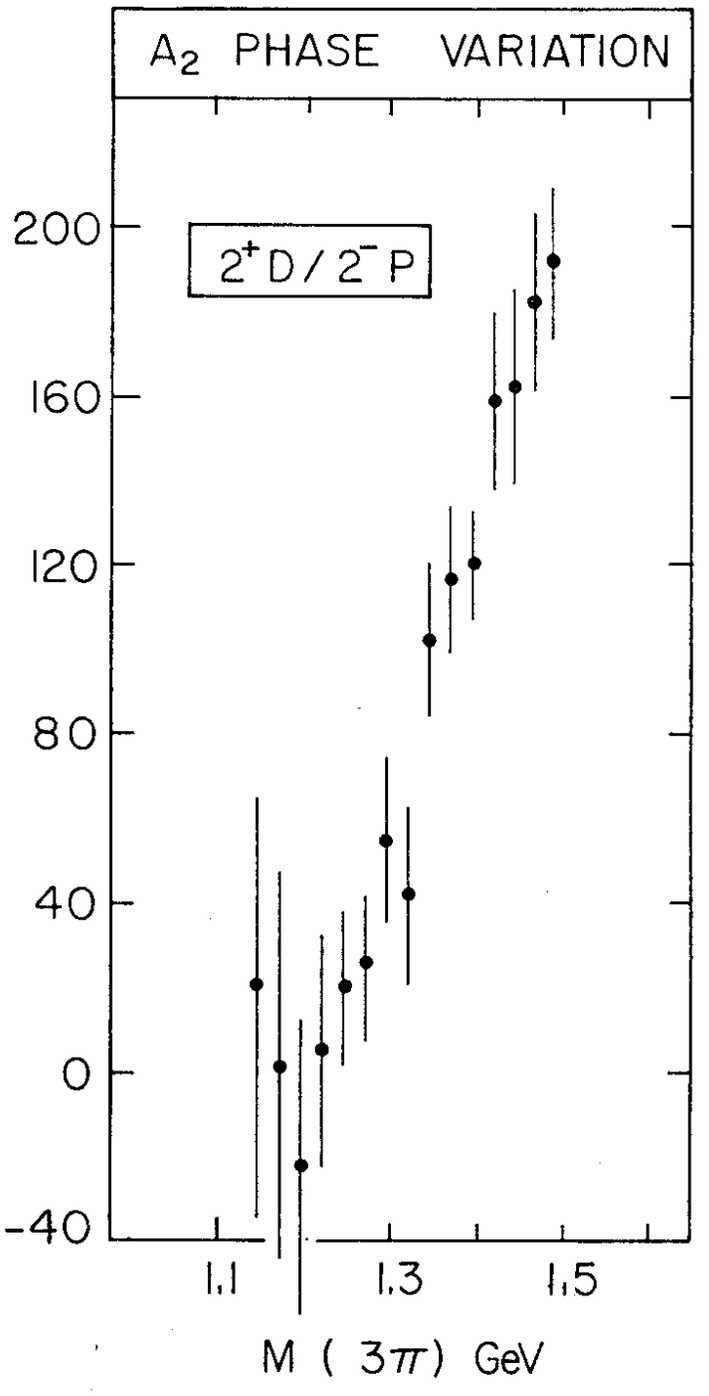

Fig. 27

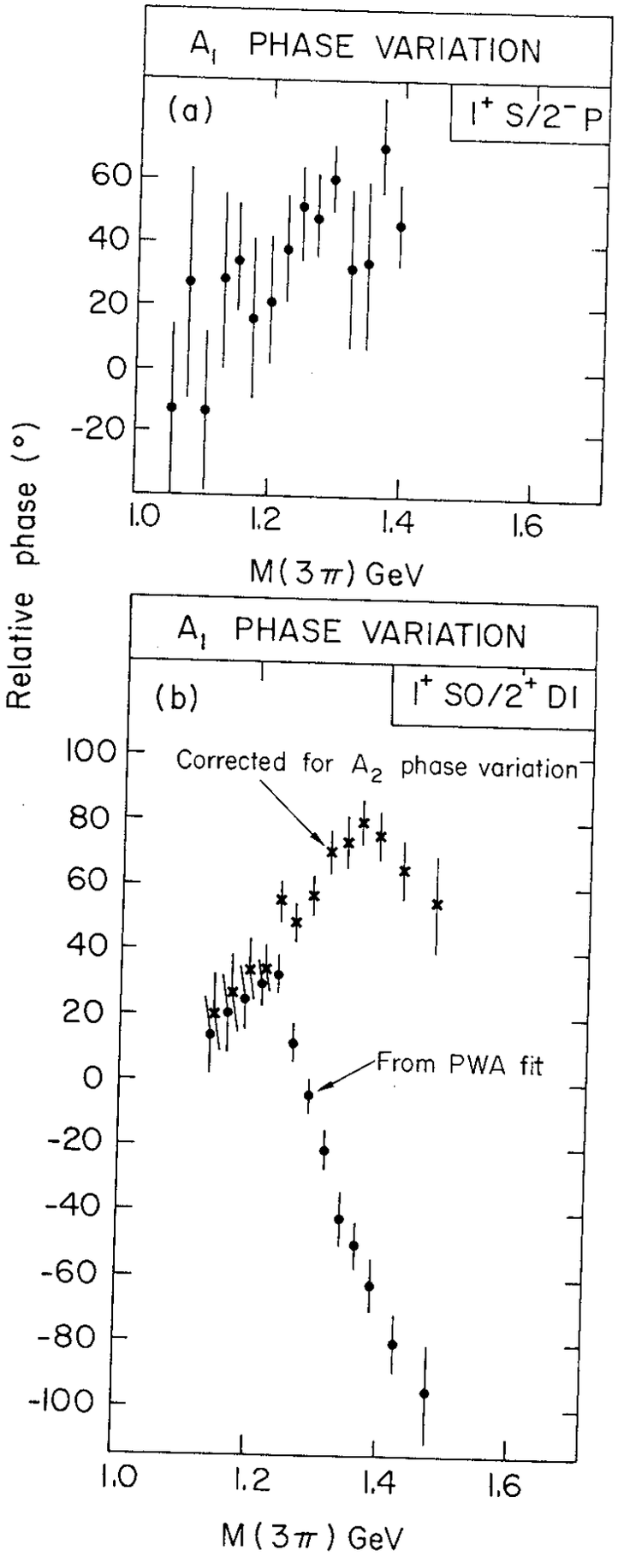
A1 PHASE VARIATION
(a)
1+ S/2- P
60
40
20
0
-20
1.0
1.2
1.4
1.6
M(3π) GeV
Relative phase (°)
A1 PHASE VARIATION
(b)
1+ S0/2+ D1
Corrected for A2 phase variation
From PWA fit
100
80
60
40
20
0
-20
-40
-60
-80
-100
1.0
1.2
1.4
1.6
M(3π) GeV

Fig. 28 a,b

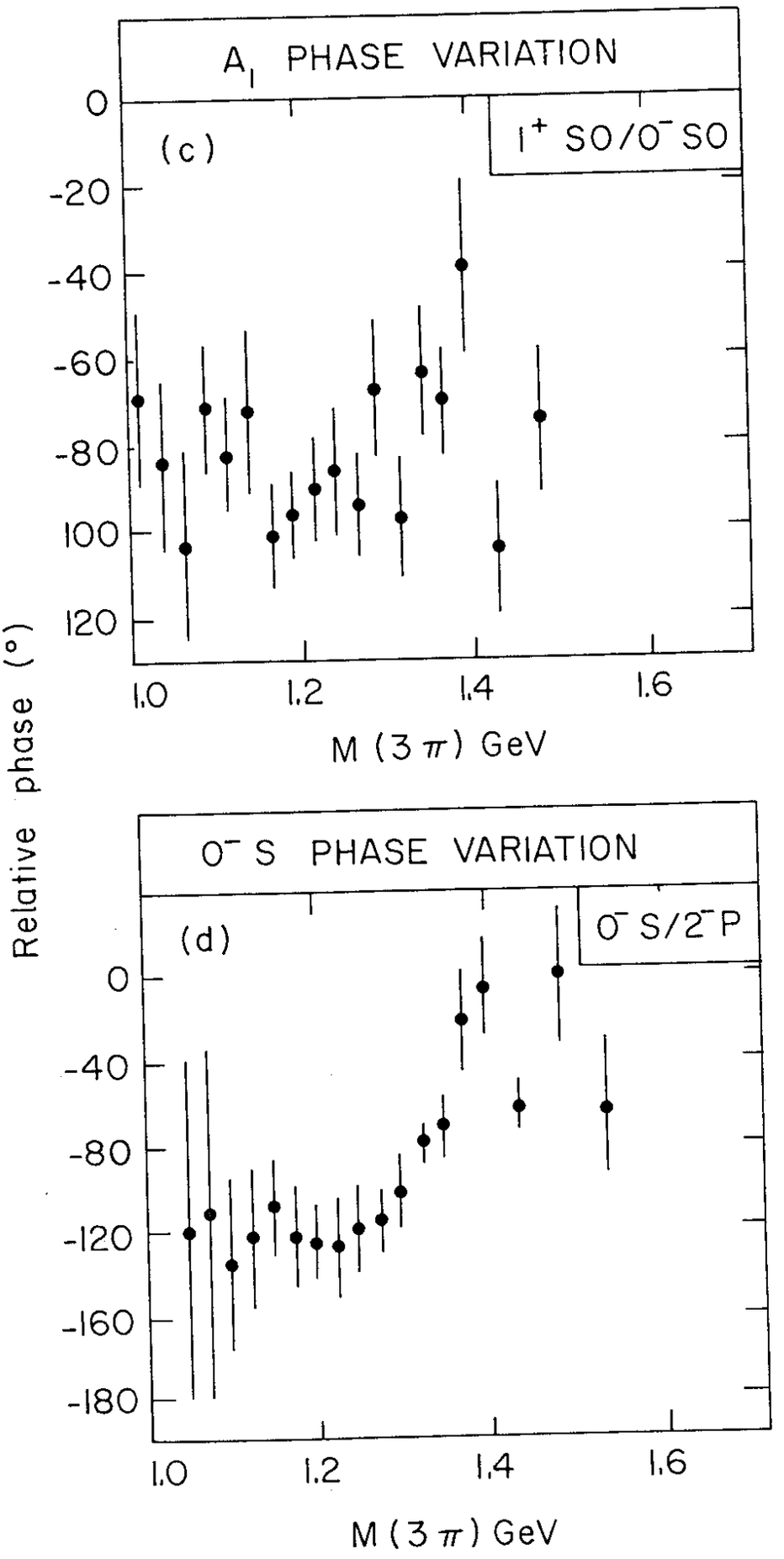
A1 PHASE VARIATION
(c)
1+ SO/0- SO
0
-20
-40
-60
-80
100
120
1.0
1.2
1.4
1.6
M (3π) GeV
Relative phase (°)
0- S PHASE VARIATION
(d)
0- S/2- P
0
-40
-80
-120
-160
-180
1.0
1.2
1.4
1.6
M (3π) GeV

Fig. 28 c, d

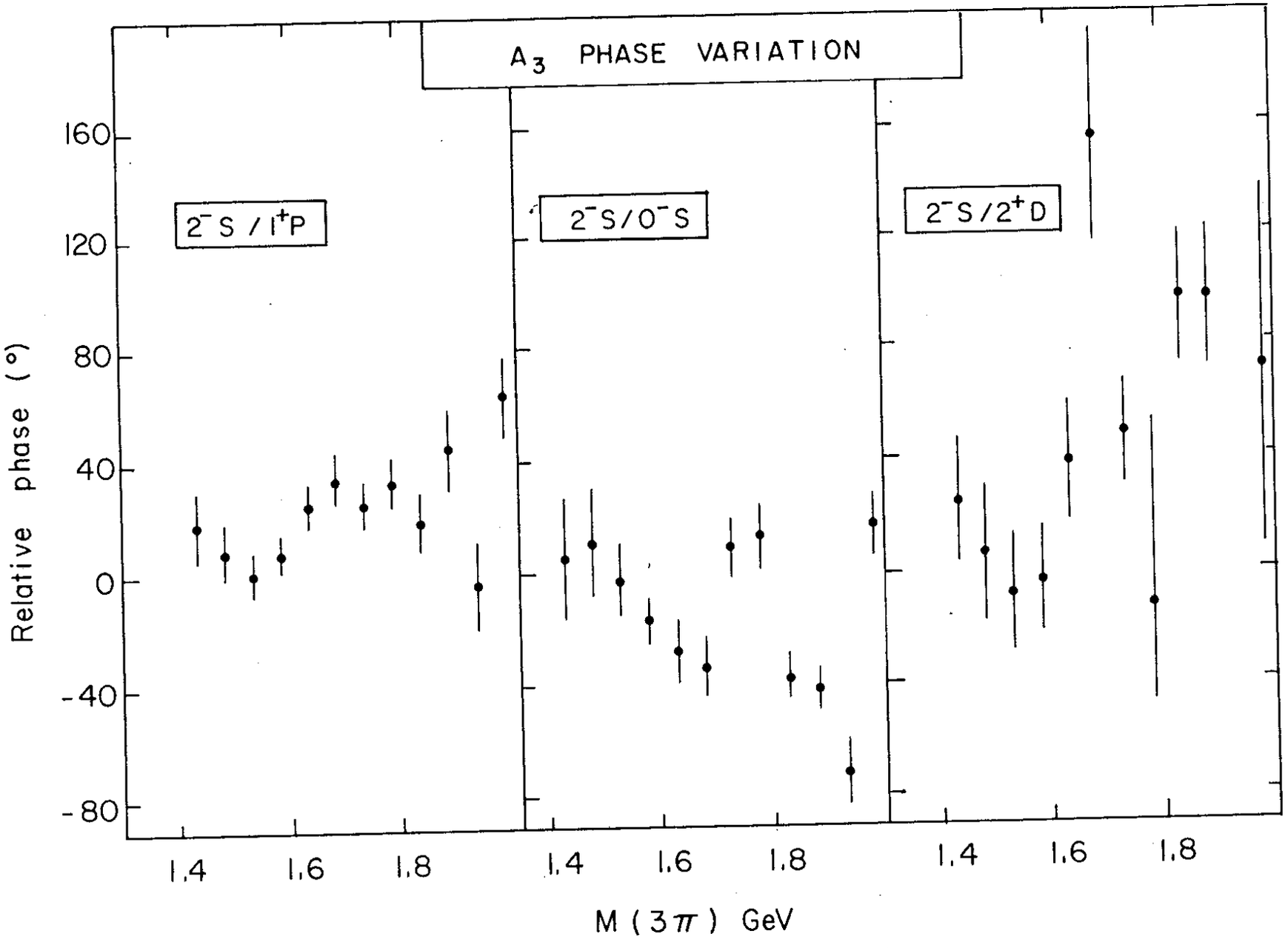
A3 PHASE VARIATION
2⁻S / 1⁺P
2⁻S / 0⁻S
2⁻S / 2⁺D
Relative phase (°)
160
120
80
40
0
-40
-80
1.4
1.6
1.8
M (3π) GeV

Fig. 29

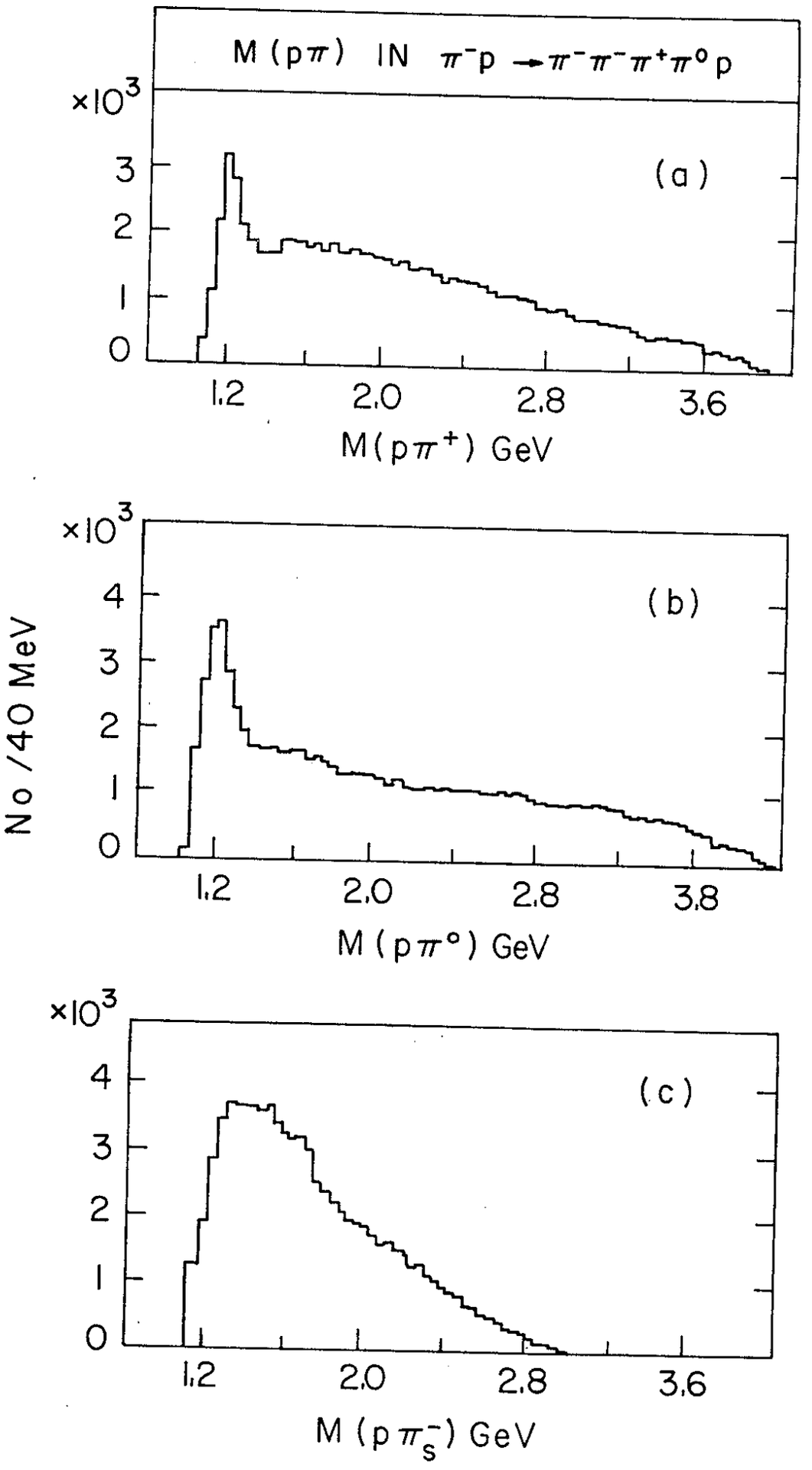
M (pπ) IN π⁻p → π⁻π⁻π⁺π°p
×10³
3
2
1
0
(a)
1.2
2.0
2.8
3.6
M(pπ⁺) GeV
×10³
4
3
2
1
0
(b)
No /40 MeV
1.2
2.0
2.8
3.8
M (pπ°) GeV
×10³
4
3
2
1
0
(c)
1.2
2.0
2.8
3.6
M (p π⁻s) GeV

Fig. 30

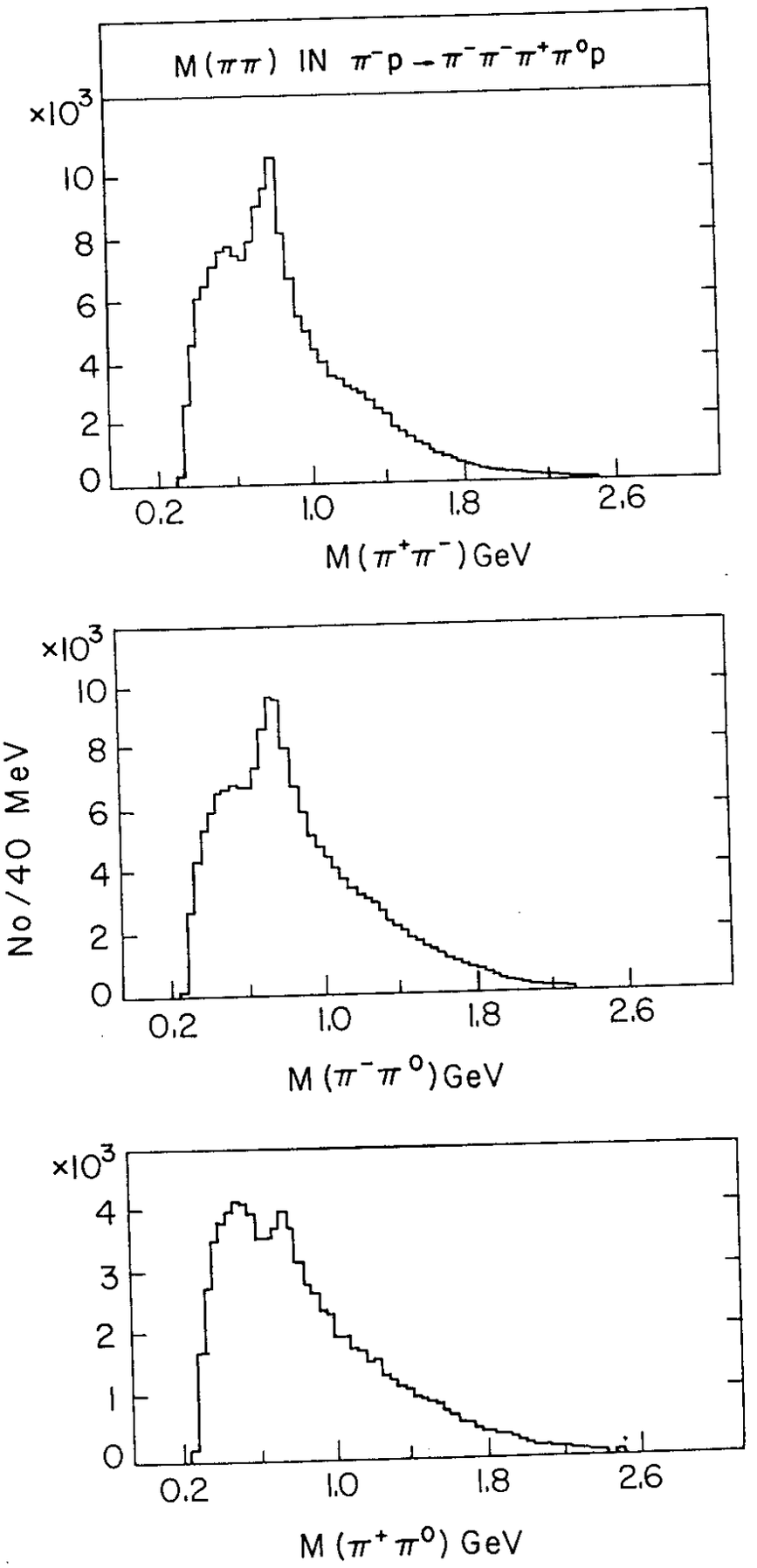
M(ππ) IN π⁻p → π⁻π⁻π⁺π⁰p
×10³
10
8
6
4
2
0
0.2
1.0
1.8
2.6
M(π⁺π⁻) GeV
No/40 MeV
M(π⁻π⁰) GeV
4
3
1
M(π⁺π⁰) GeV

Fig. 31

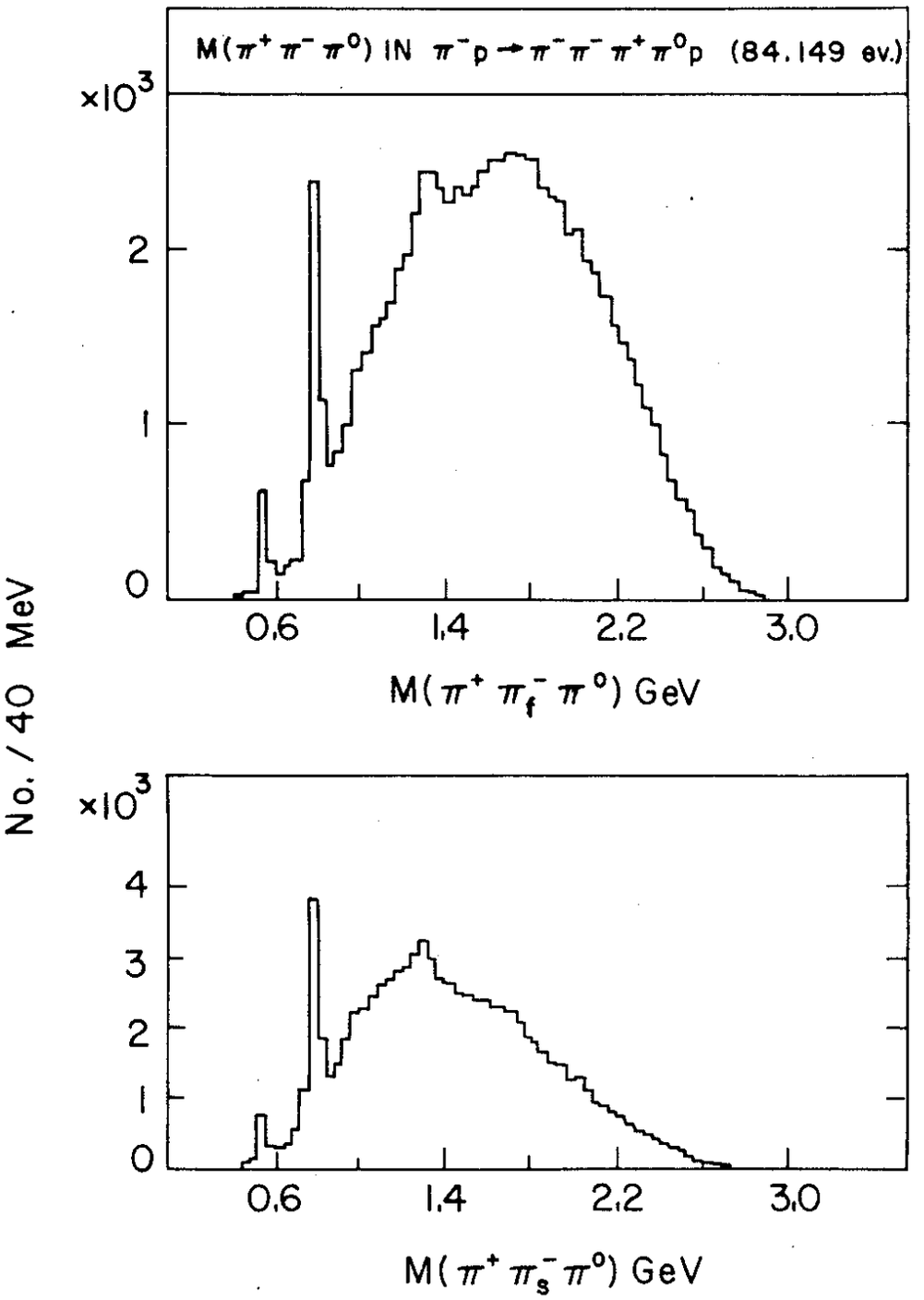
M(π⁺ π⁻ π⁰) IN π⁻p → π⁻π⁻π⁺π⁰p (84.149 ev.)
×10³
2
1
0
0.6
1.4
2.2
3.0
M(π⁺ π_f⁻ π⁰) GeV
No. / 40 MeV
×10³
4
3
2
1
0
0.6
1.4
2.2
3.0
M(π⁺ π_s⁻ π⁰) GeV

Fig. 32a

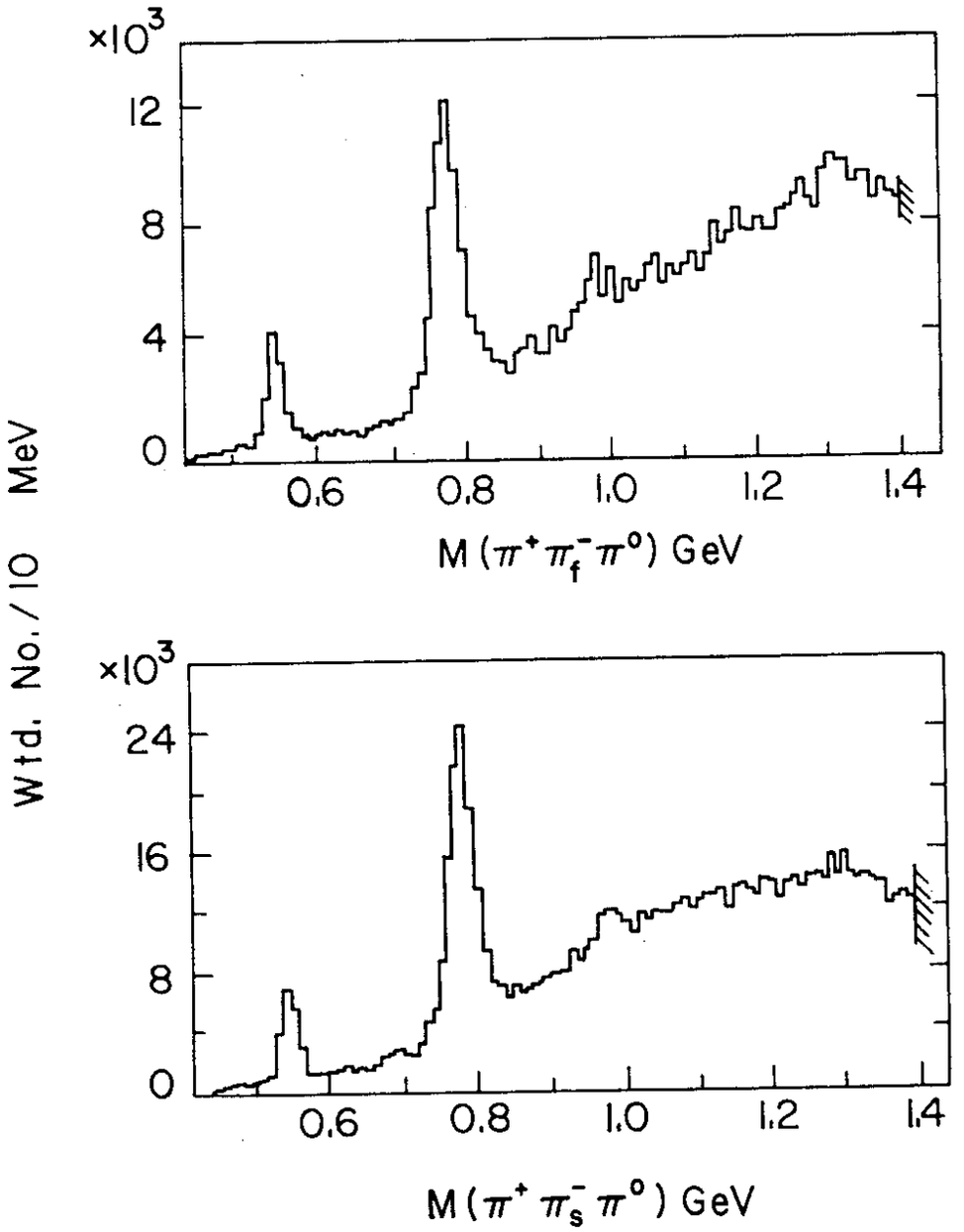
×10³
12
8
4
0
0.6
0.8
1.0
1.2
1.4
M (π⁺ π_f⁻ π⁰) GeV
Wtd. No. / 10 MeV
×10³
24
16
8
0
0.6
0.8
1.0
1.2
1.4
M (π⁺ π_s⁻ π⁰) GeV

Fig. 32b

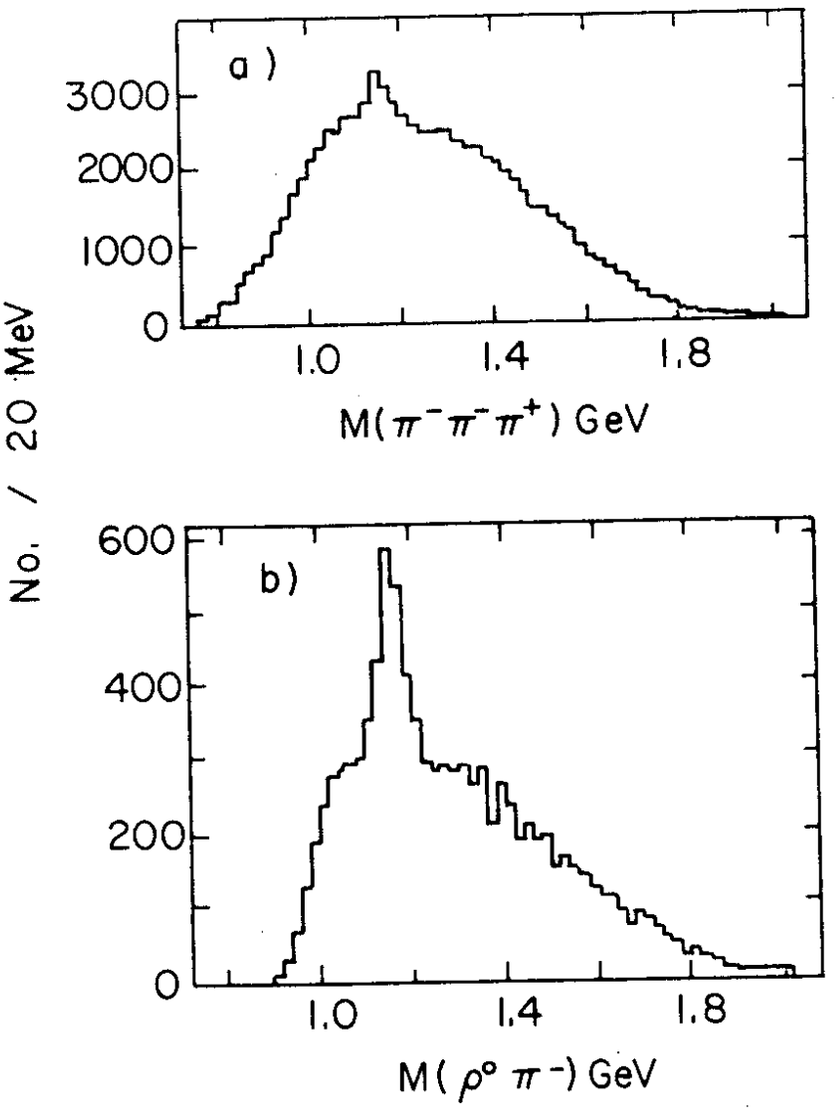
a)
3000
2000
1000
0
1.0
1.4
1.8
M(π⁻π⁻π⁺) GeV
No. / 20 MeV
b)
600
400
200
0
1.0
1.4
1.8
M(ρ° π⁻) GeV

Fig. 33

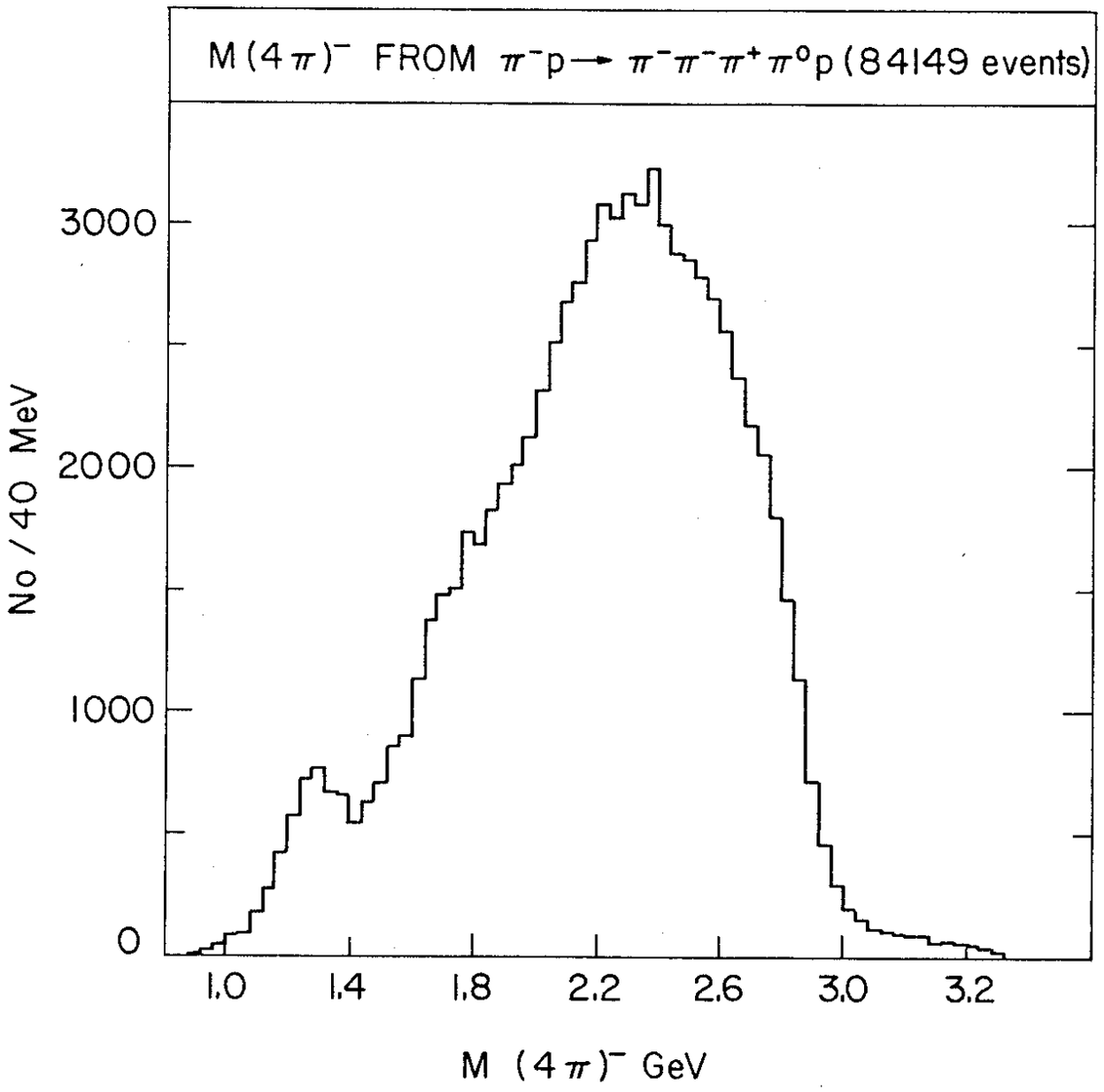
M (4π)⁻ FROM π⁻p → π⁻π⁻π⁺π⁰p (84149 events)
No / 40 MeV
3000
2000
1000
0
1.0
1.4
1.8
2.2
2.6
3.0
3.2
M (4π)⁻ GeV

Fig. 34

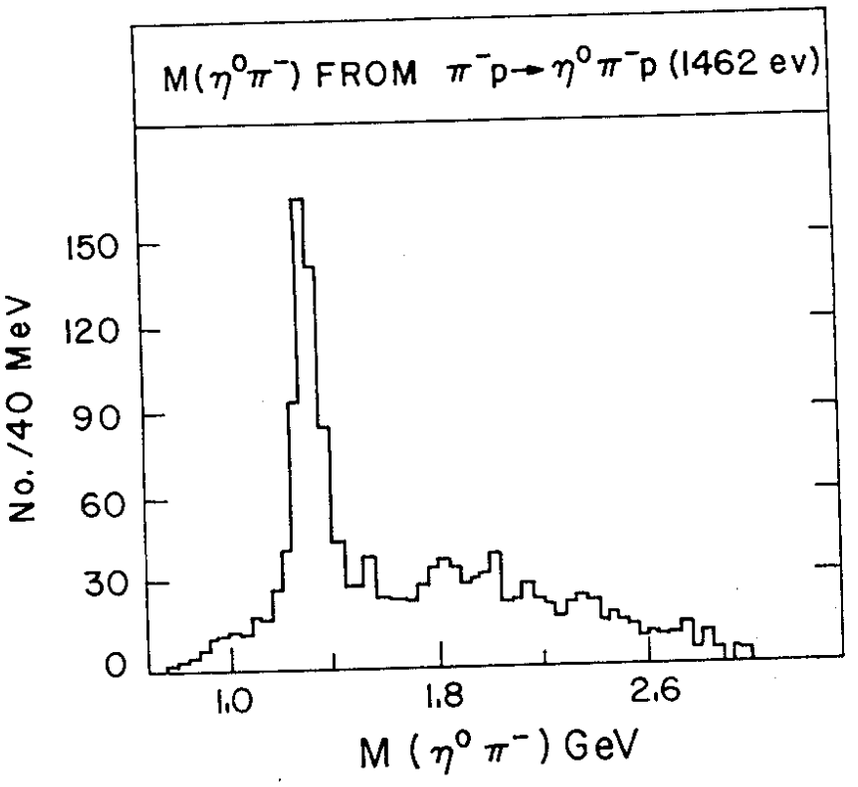
M(η⁰π⁻) FROM π⁻p→η⁰π⁻p (1462 ev)
No./40 MeV
150
120
90
60
30
0
1.0
1.8
2.6
M (η⁰ π⁻) GeV

Fig. 35

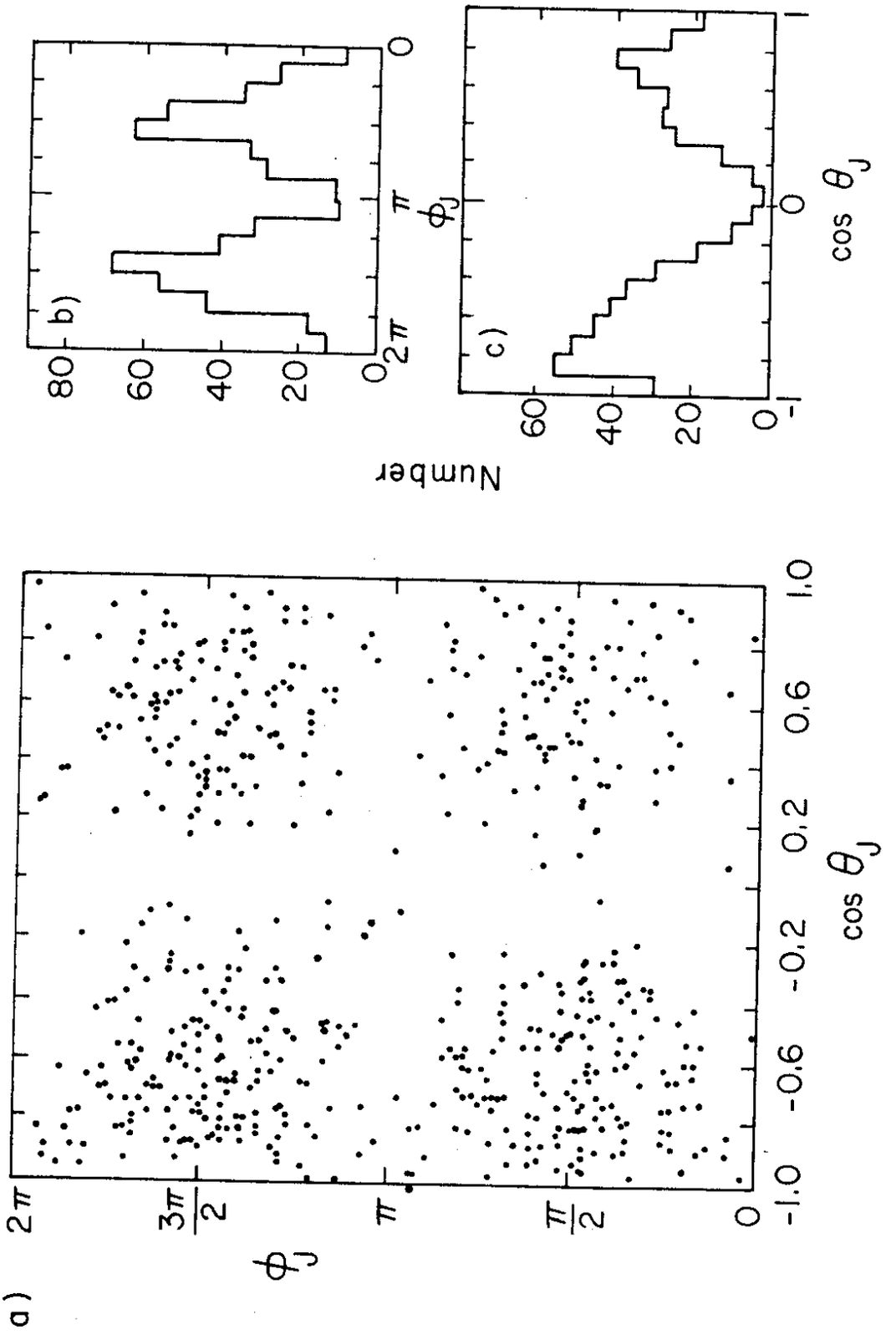
a)
2π
$\frac{3\pi}{2}$
π
$\frac{\pi}{2}$
0
ϕ_J
-1.0
-0.6
-0.2
0.2
0.6
1.0
cos θ_J
Number
b)
80
60
40
20
0
2π
π
0
ϕ_J
c)
60
40
20
0
-1
0
1
cos θ_J

Fig. 36

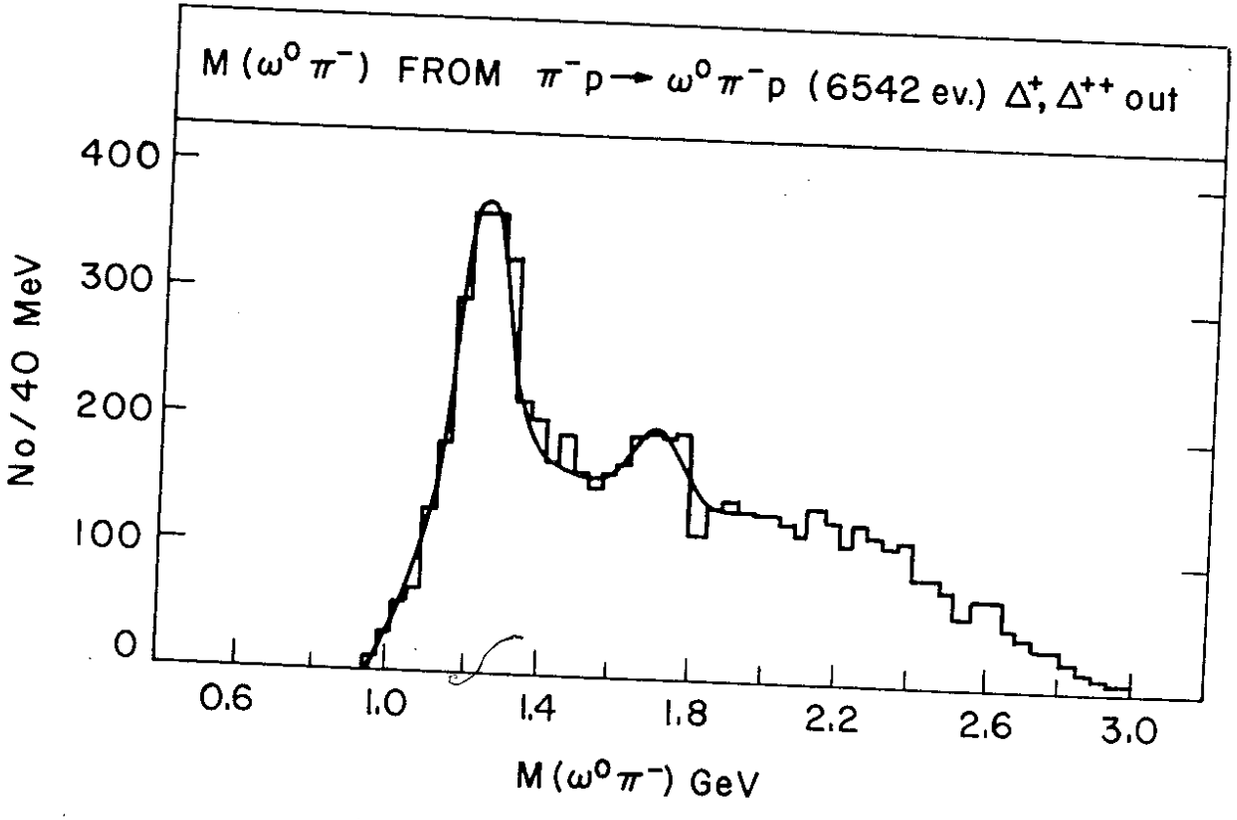
M (ω⁰ π⁻) FROM π⁻p → ω⁰π⁻p (6542 ev.) Δ⁺, Δ⁺⁺ out
400
300
200
100
0
No/40 MeV
0.6
1.0
1.4
1.8
2.2
2.6
3.0
M (ω⁰π⁻) GeV

Fig. 37

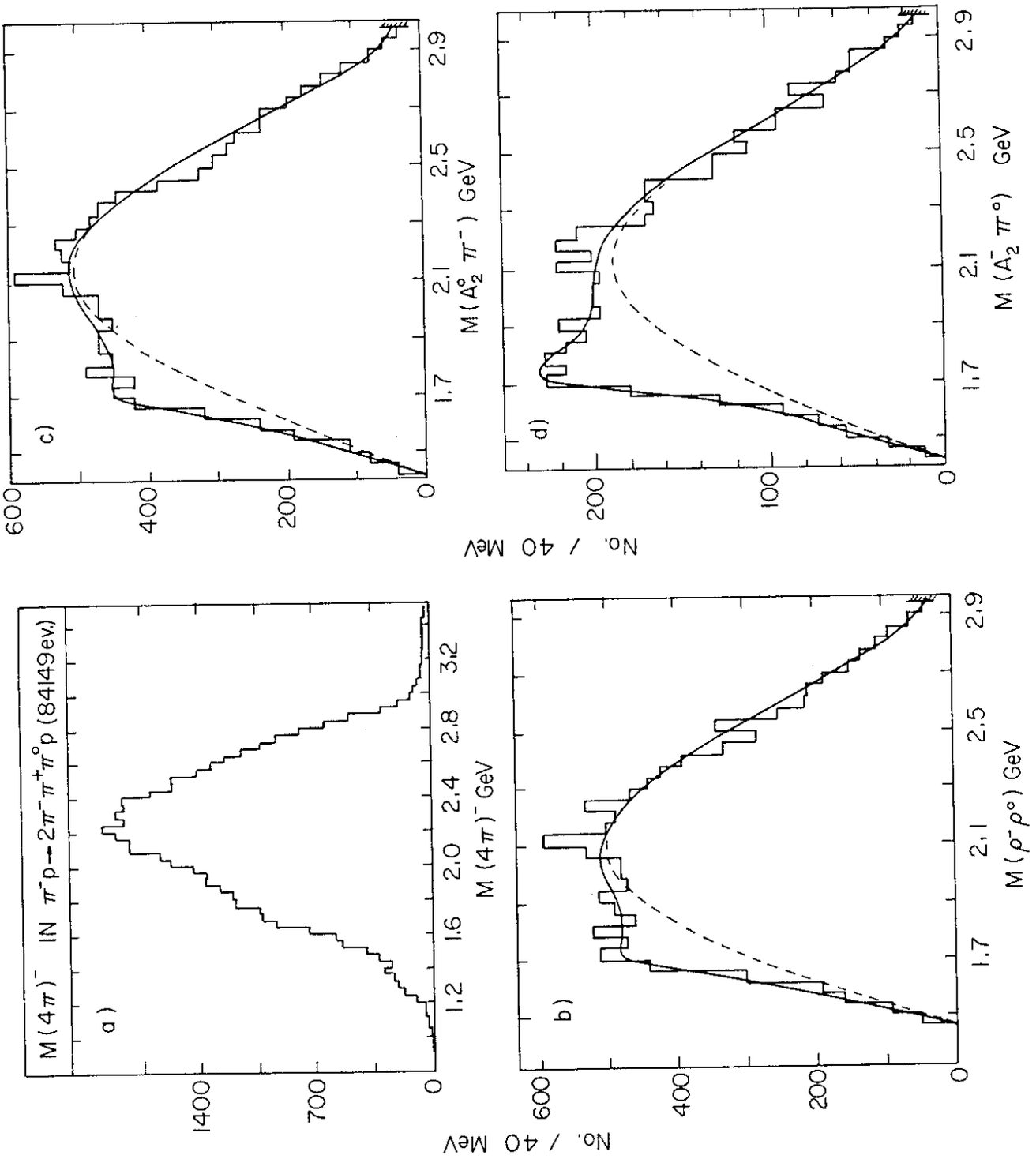
M(4π)⁻ IN π⁻p→2π⁻π⁺π°p (84149ev.)
a)
b)
c)
d)
M(4π)⁻ GeV
M(ρ⁻ρ°) GeV
M(A₂°π⁻) GeV
M(A₂⁻π°) GeV
No. / 40 MeV

Fig. 38

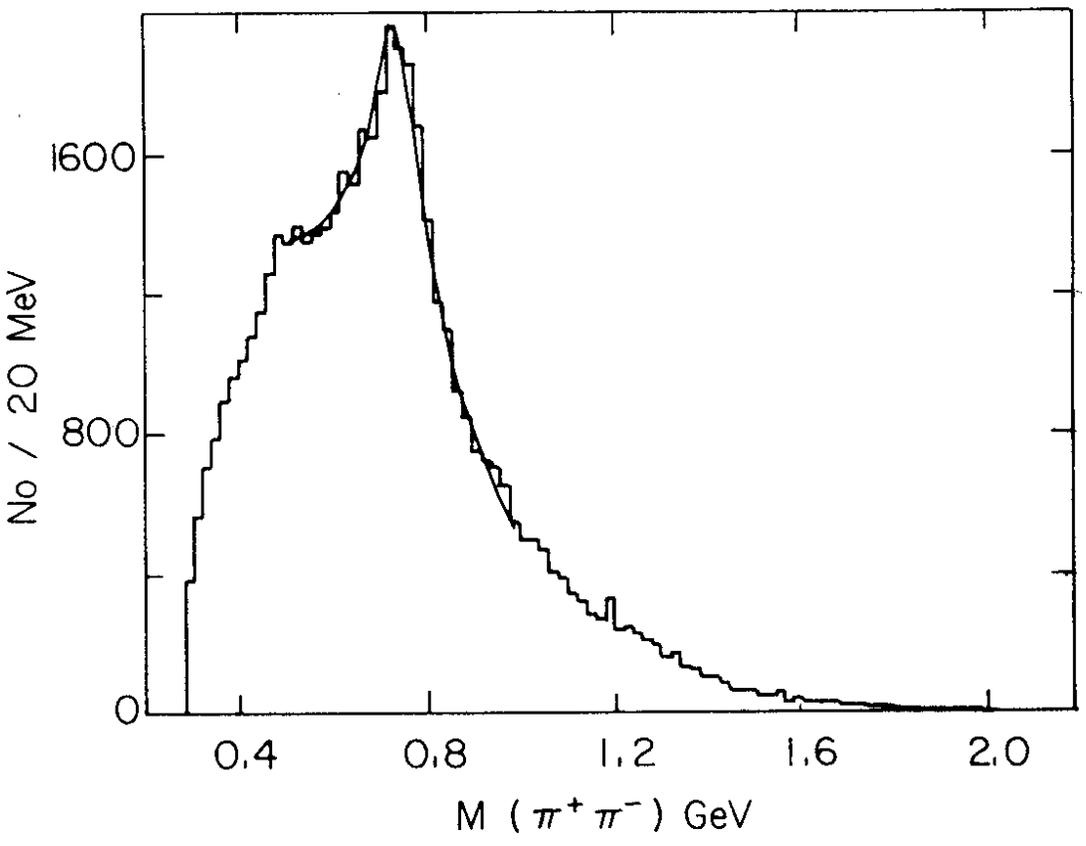

Fig. 39

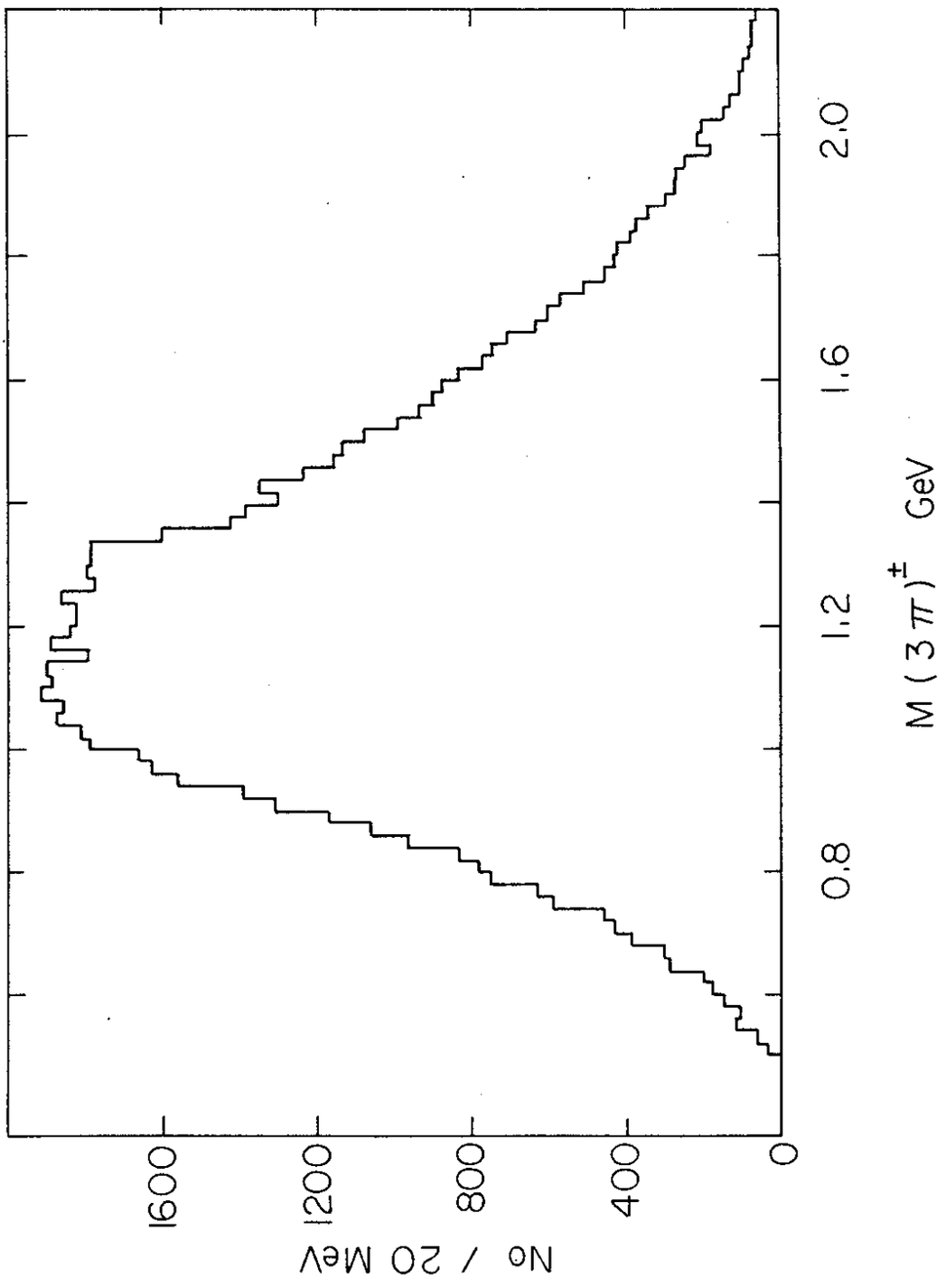

Fig. 40

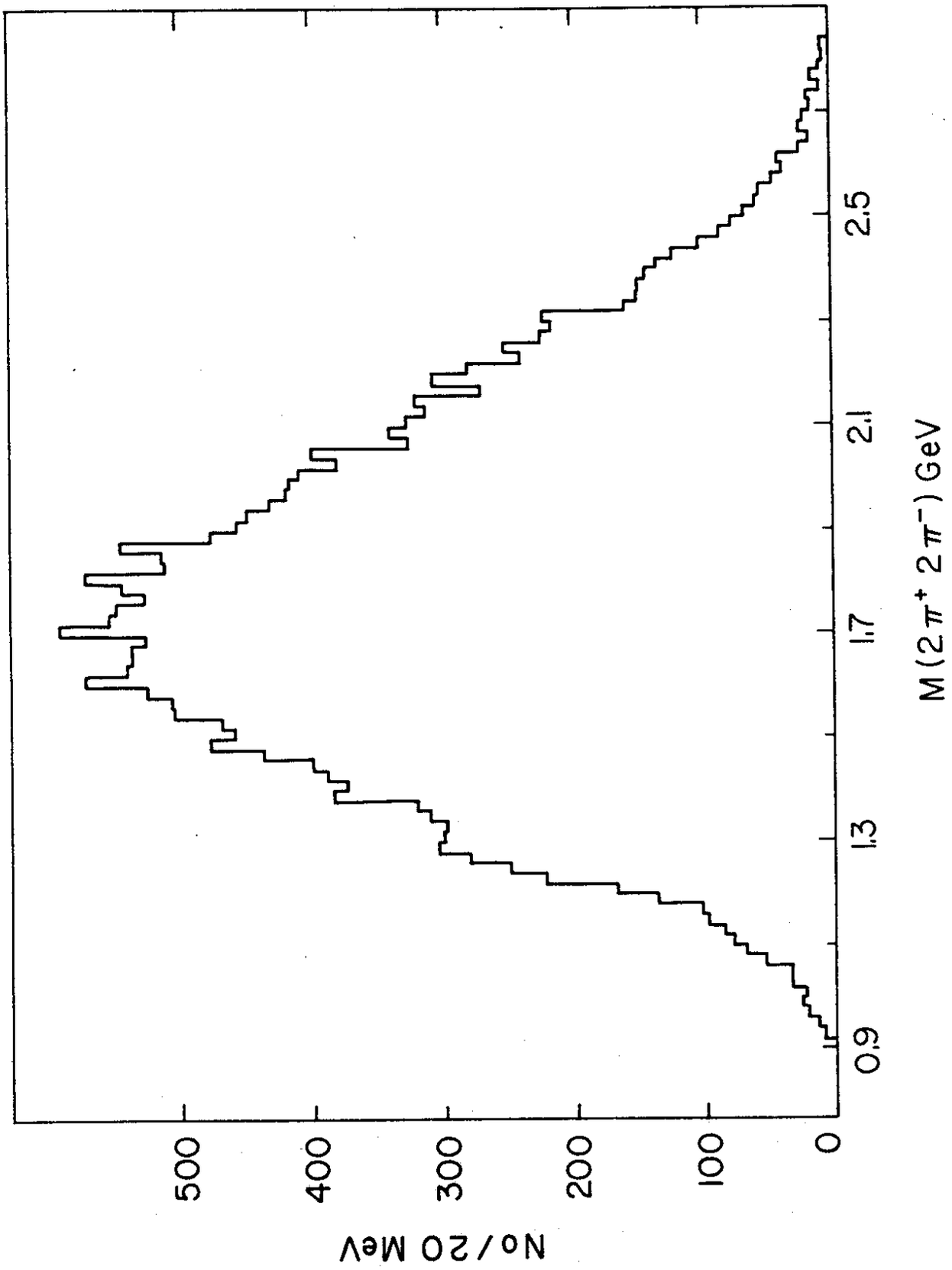

Fig. 41

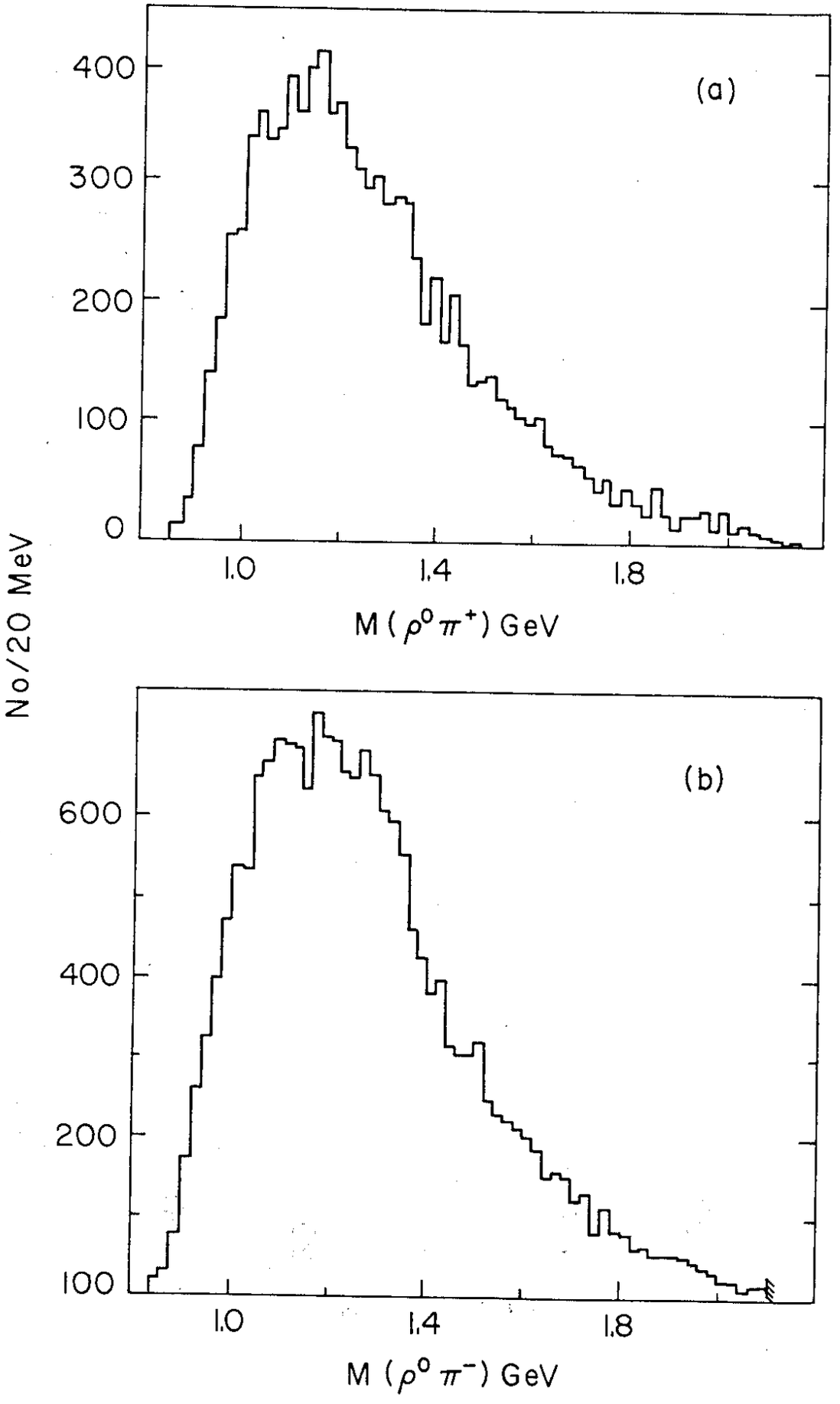
(a)
400
300
200
100
0
1.0
1.4
1.8
M ($\rho^0 \pi^+$) GeV
No/20 MeV
(b)
600
400
200
100
1.0
1.4
1.8
M ($\rho^0 \pi^-$) GeV

Fig. 42

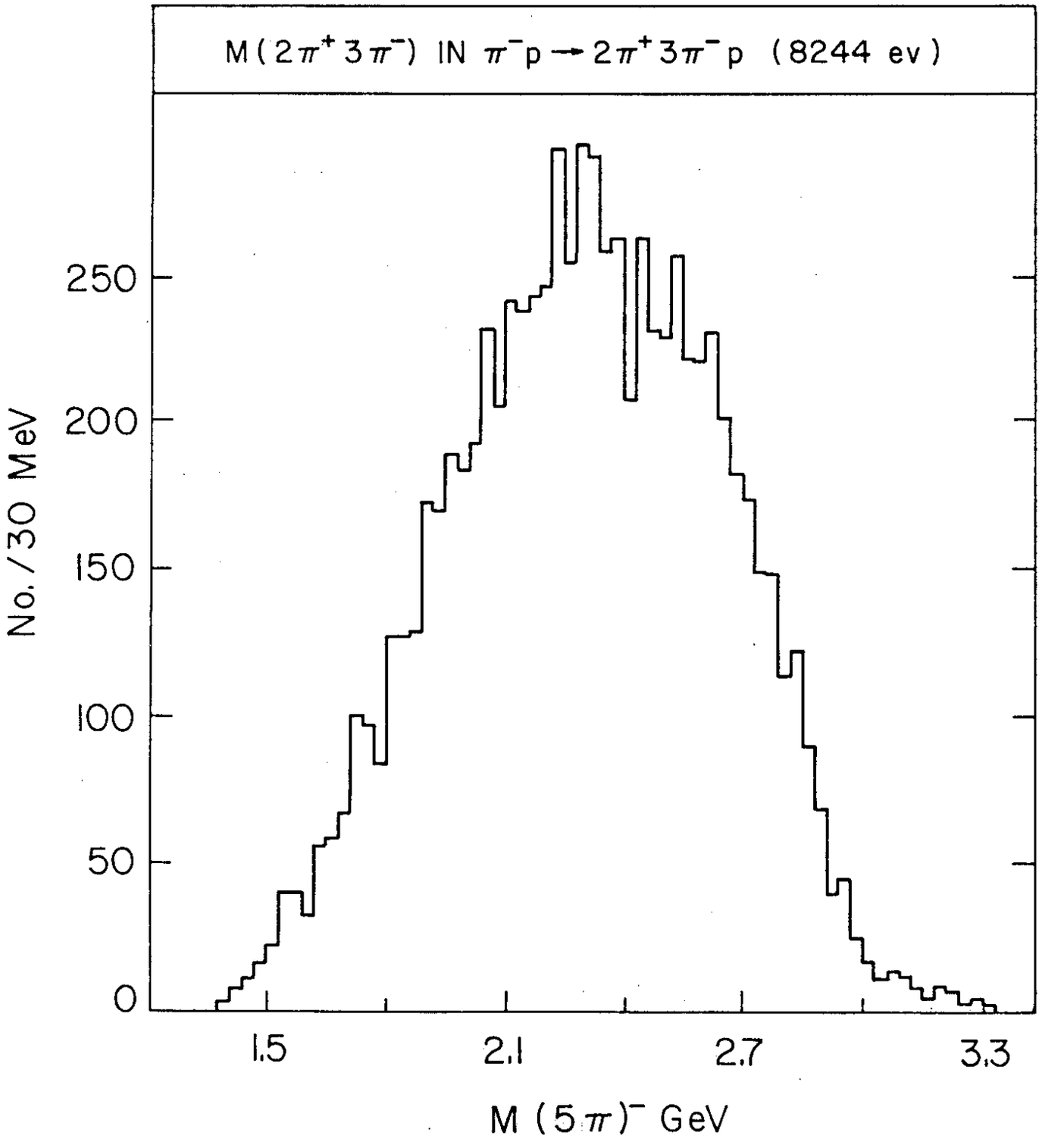
M(2π⁺3π⁻) IN π⁻p → 2π⁺3π⁻p (8244 ev)
No./30 MeV
250
200
150
100
50
0
1.5
2.1
2.7
3.3
M(5π)⁻ GeV

Fig. 43

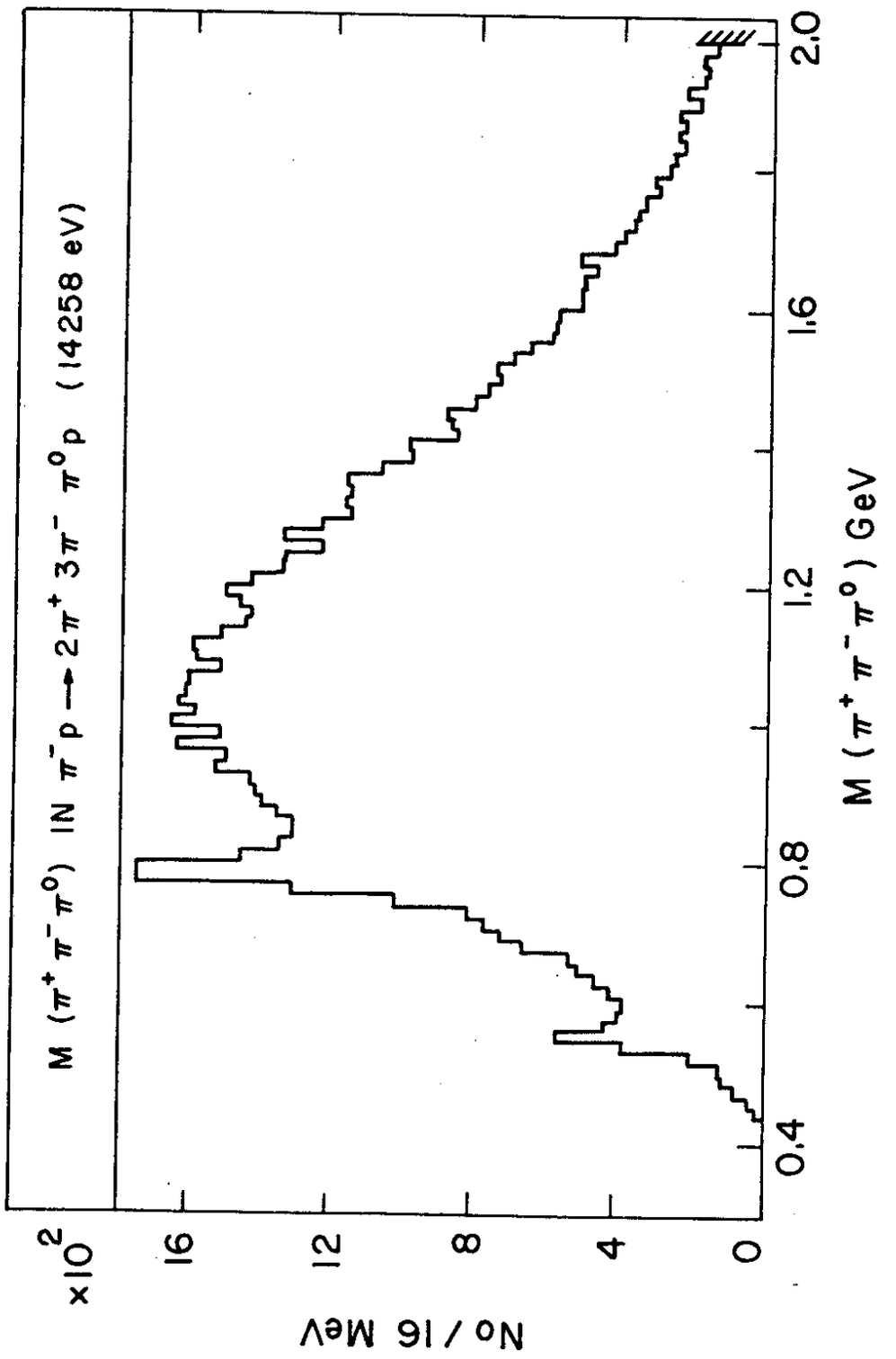
M ($\pi^+\pi^-\pi^0$) IN $\pi^- p \longrightarrow 2\pi^+ 3\pi^- \pi^0 p$ (14258 eV)
$\times 10^2$
16
12
8
4
0
No / 16 MeV
0.4
0.8
1.2
1.6
2.0
M ($\pi^+\pi^-\pi^0$) GeV

Fig. 44

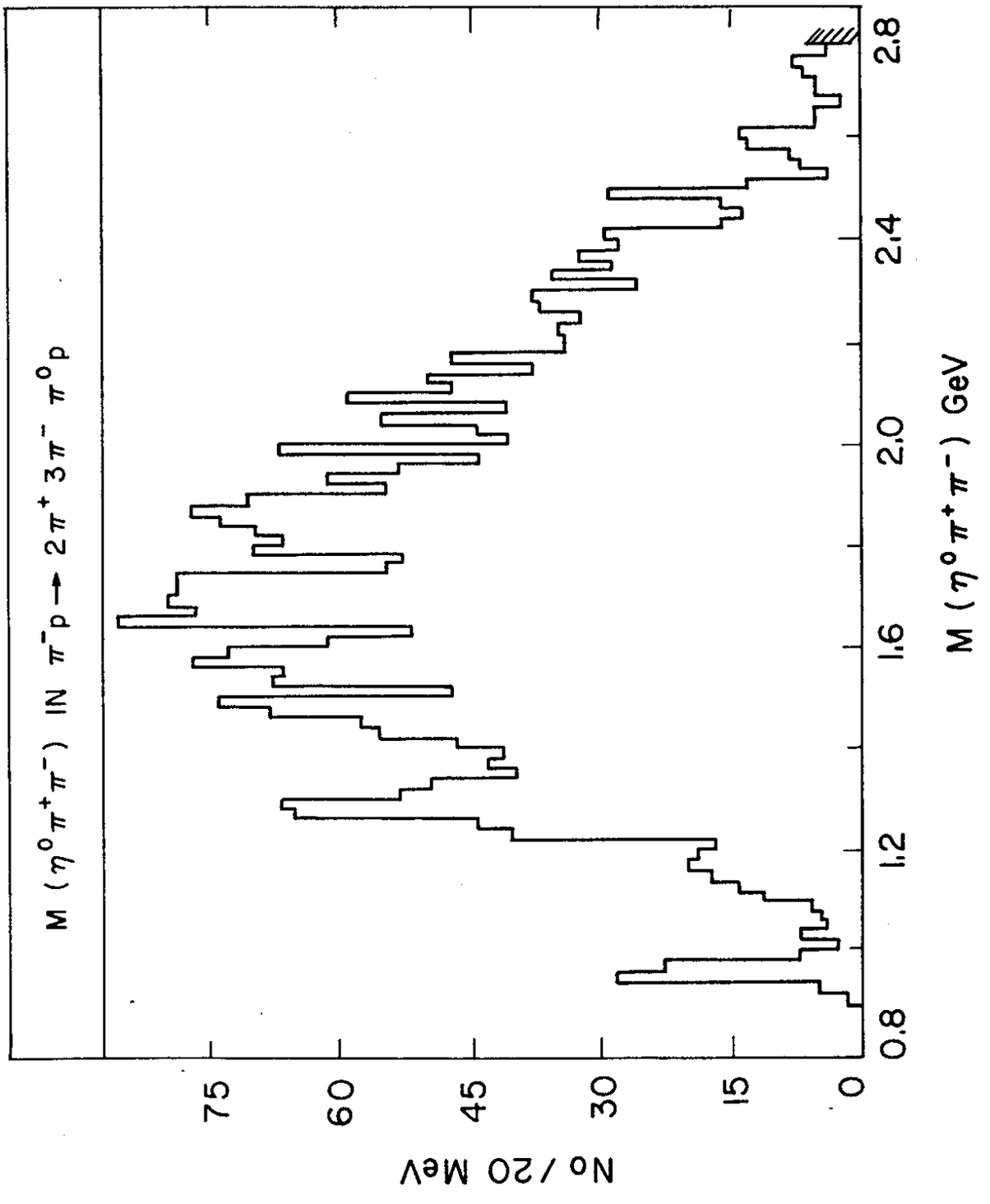
M ($\eta^0\pi^+\pi^-$) IN $\pi^-p \rightarrow 2\pi^+ 3\pi^- \pi^0 p$
No / 20 MeV
0
15
30
45
60
75
0.8
1.2
1.6
2.0
2.4
2.8
M ($\eta^0\pi^+\pi^-$) GeV

Fig. 45

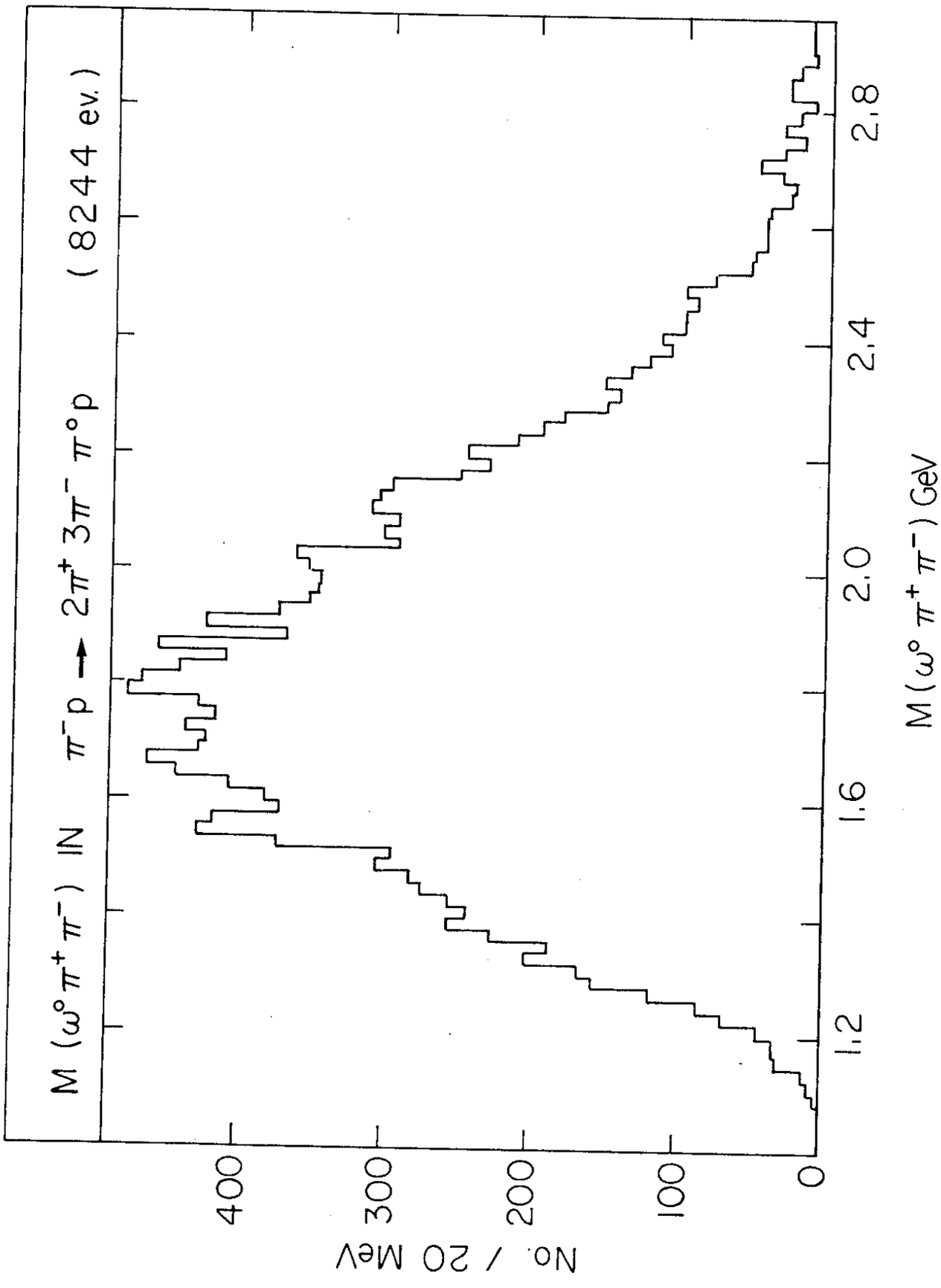
M (ω° π⁺ π⁻) IN π⁻p → 2π⁺ 3π⁻ π°p (8244 ev.)
No. / 20 MeV
0
100
200
300
400
1.2
1.6
2.0
2.4
2.8
M (ω° π⁺ π⁻) GeV

Fig. 46

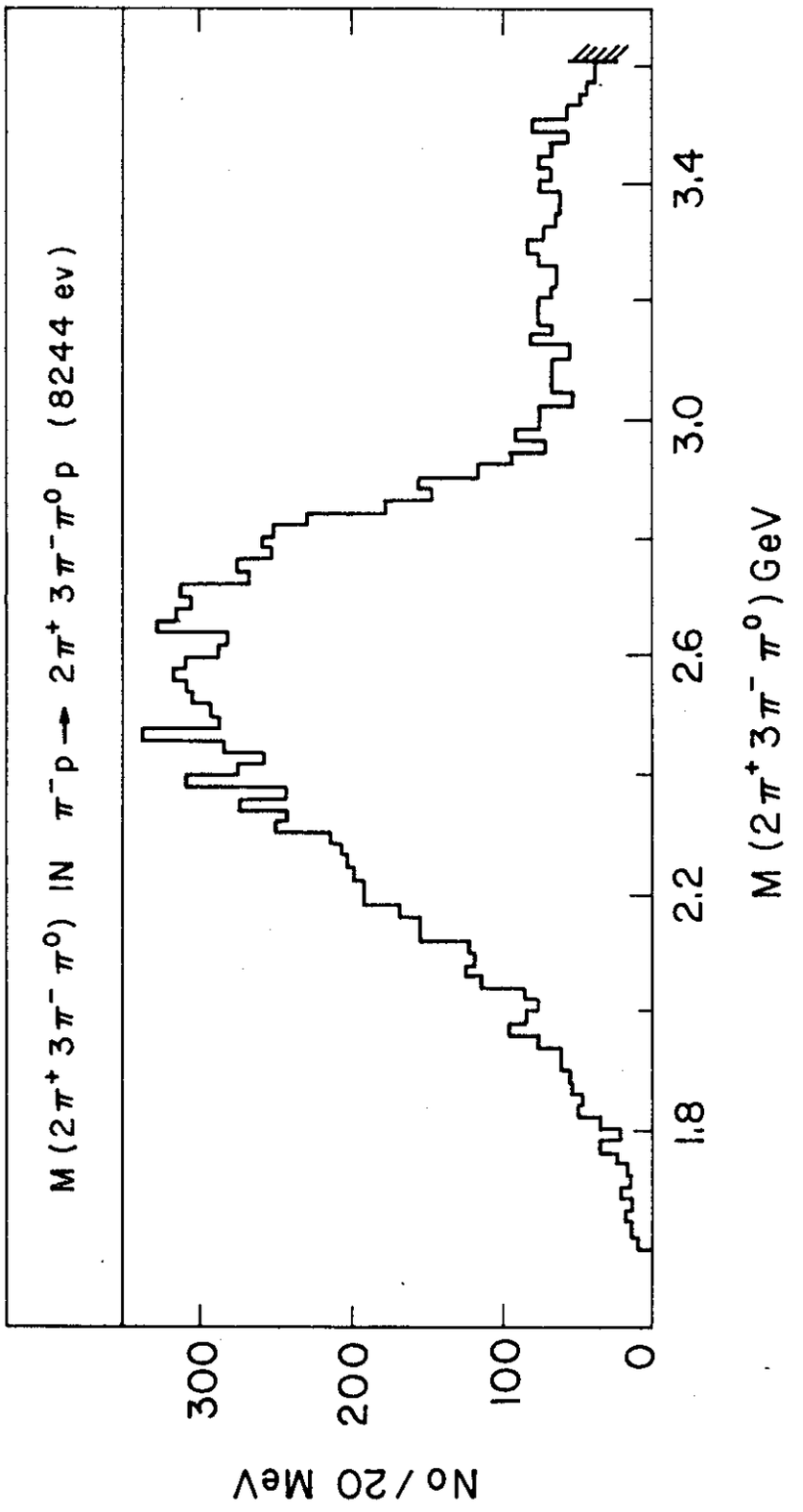
M (2π+ 3π- π0) IN π- p → 2π+ 3π- π0 p (8244 ev)
No / 20 MeV
0
100
200
300
1.8
2.2
2.6
3.0
3.4
M (2π+ 3π- π0) GeV

Fig. 47